



Università degli Studi di Pisa

---

FACOLTÀ DI SCIENZE MATEMATICHE FISICHE E NATURALI

Corso di Laurea Specialistica in Scienze Fisiche

TESI DI LAUREA SPECIALISTICA

**On the resolution in a measurement of dijet  
invariant mass when searching for associated  
WZ production with CDF**

Candidato:  
**Sabato Leo**

Relatori:  
**Prof. Giorgio Bellettini**  
  
**Dr. Gueorgui V. Velev**



# Contents

<b>Abstract</b>	<b>v</b>
<b>Introduction</b>	<b>vii</b>
<b>1 The Standard Model</b>	<b>1</b>
1.1 Particles and Fields in the Standard Model . . . . .	2
1.2 Electroweak Unification . . . . .	5
1.3 Associated WZ Production . . . . .	6
1.4 Observations of Associated WZ Production at the Tevatron . . . . .	7
1.5 Higgs Searches . . . . .	8
<b>2 The Fermilab Tevatron Collider and the CDF II Detector</b>	<b>13</b>
2.1 Tevatron Collider . . . . .	13
2.2 CDF II Detector . . . . .	15
2.3 Coordinates and Notation . . . . .	16
2.4 The Tracking System . . . . .	18
2.4.1 The Superconducting Solenoid . . . . .	19
2.4.2 Silicon System . . . . .	19
2.4.3 Central Outer Tracker . . . . .	21
2.5 Calorimeters . . . . .	22
2.5.1 Electromagnetic Calorimeter . . . . .	23
2.5.2 Hadronic Calorimeter . . . . .	25
2.6 Trigger and Data Acquisition System . . . . .	26
2.7 CDF Software Framework . . . . .	27

2.8	Monte Carlo Simulation of Detector and Trigger . . . . .	29
<b>3</b>	<b>Identification and Definition of Objects</b>	<b>31</b>
3.1	Track Reconstruction . . . . .	31
3.1.1	Tracking Algorithms . . . . .	32
3.2	Calorimeter Electron and Photon Identification . . . . .	34
3.3	Muon Identification . . . . .	37
3.4	Neutrino Identification . . . . .	37
3.5	Jet Identification . . . . .	38
3.5.1	CDF Cone Algorithm . . . . .	41
3.6	Jet Corrections . . . . .	42
3.6.1	Corrections to the Raw Measured Jet Energy . . . . .	43
3.6.2	Corrections to the Raw Measured Missing $E_T$ . . . . .	47
3.7	Secondary Vertex Tagging . . . . .	48
3.7.1	Tagging Performances and Scale Factors . . . . .	50
<b>4</b>	<b>Event Selection</b>	<b>55</b>
4.1	Data Trigger Streams . . . . .	55
4.1.1	Physical Objects . . . . .	56
<b>5</b>	<b>Optimization of dijet Invariant Mass Resolution: Tracker-based methods</b>	<b>59</b>
5.1	MC Sample . . . . .	60
5.2	Initial Considerations . . . . .	60
5.3	Invariant Mass Studies . . . . .	62
5.4	Correcting the Axis of Jets in Cracks . . . . .	64
5.5	K Scale Factors . . . . .	65
5.6	Correcting Energy of Jets in Cracks . . . . .	68
5.7	Correcting Axis Using Tracker Info . . . . .	71
5.7.1	Golden Sample . . . . .	71
5.8	Charge Fraction Studies . . . . .	72
<b>6</b>	<b>Optimization of dijet Invariant Mass Resolution: Calorimeter-based</b>	

<b>methods</b>	<b>77</b>
6.1 Introduction . . . . .	77
6.2 Three Tight Jets Subsample . . . . .	79
6.3 Two Tight Jets Subsample . . . . .	80
6.4 Results on the Inclusive Sample . . . . .	81
6.5 Including the Third Jet all-over . . . . .	81
<b>7 Concluding Summary and Future Prospects</b>	<b>91</b>
<b>Appendices</b>	<b>93</b>
<b>A Some Details on the SM and the Higgs Mechanism</b>	<b>95</b>
A.1 The Higgs Mechanism . . . . .	97
A.1.1 Spontaneous Symmetry Breaking in SM . . . . .	100
A.2 Quantum Chromodynamics . . . . .	101
<b>B Collision Energy and Luminosity</b>	<b>105</b>
<b>C Tevatron Collider Operation</b>	<b>107</b>
C.1 Proton Production . . . . .	107
C.2 Antiproton Production and Accumulation . . . . .	107
C.3 Injection and Collisions . . . . .	109
C.4 Tevatron Performance . . . . .	110
<b>D Other CDF II Sub-Detectors</b>	<b>113</b>
D.1 Time-of-Flight Detector . . . . .	113
D.2 Muon Detectors . . . . .	113
D.3 Cherenkov Luminosity Counters . . . . .	115
D.4 Forward Detectors and Beam Monitoring . . . . .	116
<b>E Trigger Levels</b>	<b>119</b>
E.1 Level-1 . . . . .	119
E.2 Level-2 . . . . .	119
E.3 Level-3 . . . . .	120

<b>F Track Parameters</b>	<b>121</b>
<b>G Signal and Background Cross Sections</b>	<b>123</b>
<b>H Nominal Interaction Vertex</b>	<b>125</b>
<b>Bibliography</b>	<b>127</b>
<b>Acknowledgements</b>	<b>135</b>

# Abstract

We report on a number of simulation studies on how to improve the invariant mass resolution of a particle decaying into two large energy hadron jets. This is a preliminary step of an effort to observe associated WZ production. This process is extremely rare and competes with a large background, and any even minor improvement in resolution deserves great attention.

These tools would be of interest in the study of many rare multi-jet processes. They are implemented here in a simulated measurement of  $Z \rightarrow q\bar{q}$  decay (aiming eventually at a  $H \rightarrow b\bar{b}$  decay), in associated WZ (WH) production in  $p\bar{p}$  collisions at  $\sqrt{s}= 1.96$  TeV recorded by the CDF II experiment at the Fermilab Tevatron Collider.

We generate WZ events with an identified charged lepton, a large imbalance in transverse momentum, and at least two large transverse energy jets. We determine the sample selection cuts by studying jet energy dependence of signal and background. The main backgrounds, noticeably W+jets production, are modeled based on experimental data whenever possible. We first try to optimize the sensitivity to a jet-jet invariant mass peak by complementing the information provided by the CDF calorimeter with that of the tracker. For mis-measured calorimeter jets, and for jets fragmenting with a large charged-to-neutral ratio, the jet axis could be better measured in the tracker. As a consequence the dijet invariant mass could be better measured. The study starts by checking the best ever achievable improvement by adopting the primary parton direction as jet axis. This study is performed on a  $WZ \rightarrow l\nu q\bar{q}$  PHYTIA Monte Carlo in the simpler case of light decay quarks. Improvements in dijet mass resolution of the order of a few % are obtained in a number of cases. Next we try to develop event-specific energy corrections for calorimeter jets. Again, improvements of the order of a few % are obtained in a number of cases. The combination of these two methods indicates possible improvements in dijet mass resolution up to  $\sim 5\%$ .

When the study is extended to using, rather than primary quark directions, tracker jet axes which are experimental observables, no real progress is predicted. However, the study is extended to event specific corrections to calorimeter jets based on additional information carried by the tracker and the calorimeter. This study gives very interesting and promising indications. Criteria by which we select and merge jets due to final state radiation (FSR) are discussed, and the impact on dijet mass resolution of merging three jets for reconstructing W or Z in  $q\bar{q}$  decay is studied.

# Introduction

This thesis summarizes the work done by the candidate with the CDF-Pisa group from winter 2008 to fall 2009. A significant effort was spent reviewing the physics of diboson production, which is the topics of this search, and the layout and the operation mode of the Fermilab Tevatron Collider and of the CDF detector. This was a necessary preliminary step because the candidate joined the group efforts when the collider and the detector were operating in a stable mode, as a given “bonus” to a newcomer. This work is reported in chapters 1 to 3 and in the appendices. The analysis work of the candidate is reported in chapters 4 to 6. His most significant original contributions are described in chapters 5 and 6, where very detailed studies to find out whether information on the charged component of hadron jets can be used to improve the resolution on the mass of the  $Z$  boson in the two jets final state. In chapter 6 his most recent studies on the possible exploitation of more than two final state jets to measure the  $Z$  mass are reported. The studies are very promising, but they are still in a preliminary phase. In chapter 7 there is a summary of the work and a guide line for future extentions.



# Chapter 1

## The Standard Model

*A most ambitious theory describing matter at its fundamental level, the standard model of particle physics, is summarized in this chapter. Fundamental particles and interactions are listed in sec. 1.1.  $W$ ,  $Z$  bosons and Higgs mechanism are introduced in sec. 1.2 and appendix A.1. Appendix A.2 gives an introduction to Quantum Chromodynamics. A summary of  $W$ ,  $Z$  production data is given in sec. 1.3 and sec. 1.4. Some experimental results on Higgs searches are summarized in sec. 1.5.*

### Premise

One can date the birth of a new era of deeper understanding of the basic constituents of matter with the discovery of the quark structure of the proton at the Stanford Linear Accelerator Center in 1968. The discovery was made by a deep inelastic scattering experiment of electrons on protons [1]. That experiment probed the inner structure of the target proton at scale of about  $1 \text{ fm} = 10^{-13} \text{ cm}$  and found hard point-like scattering centers within the target. According to the uncertainty principle,  $\Delta P \Delta x \geq \hbar c \sim 0.2 \text{ fm} \cdot \text{GeV}$ . In order to probe the proton at such small distance one needs to transfer momenta of  $\Delta P \gg 1 \text{ GeV}$ . The discovery became possible when electron beams of energy in the range 7 to 17 GeV became available [1]. Higher energies are also needed for discovering new heavy unstable particles. Although these particles are unstable they may play an important role in nature, such as the  $W/Z$  bosons and the top quark. A crucial role in the search for new particles of higher energies is played by experiments at collider accelerators,

presently at the Fermilab antiproton-proton 1.96 TeV collider and soon at the CERN proton-proton collider which will reach ultimately an energy of 14 TeV in the c.m.s. The effort reported in this thesis fits within this line of research. Our work is based on simulated WZ events of the CDFII experiment at the Tevatron collider center-of-mass energy  $\sqrt{s} = 1.96$  TeV. Since the topology of these events is very similar to that of associated production of Z and light Higgs boson, this work is a preliminary step towards a search for the Higgs itself, the next new fundamental particle hopefully to be discovered.

## 1.1 Particles and Fields in the Standard Model

At our current level of understanding the basic constituents of matter are the quarks and leptons, which are spin 1/2 particles (fermions). Six quarks and six leptons have been experimentally observed and their exchange forces have been studied in great detail. The interaction between the fundamental fermions is built up out of four terms, the gravitational, weak, electromagnetic (EM), and strong interaction. The weak, EM and strong interaction are mediated by spin 1 particles, which are called bosons. The gravitational interaction is supposed to be mediated by a spin 2 boson.

The SM is a consistent and calculable theory that successfully explains most of the known phenomena in elementary particle physics [2],[3]. The SM describes weak, electromagnetic and strong interactions. Although it is desirable to have a unified treatment of all known forces including gravity, a satisfactory theory extending the SM to include gravity does not exist yet. On the other hand, in particle physics experiments the role of gravity is negligible.

The SM is based on the gauge symmetry group  $SU(3) \otimes SU(2) \otimes U(1)$  which describes the microscopic world in terms of interacting particles and fields in the framework of relativistic quantum field theory [4].  $SU(3)$  describes the strong interactions, whose theory is named Quantum Chromodynamics (QCD).  $SU(2)$  describes the weak interactions and  $U(1)$  the electromagnetic interactions (Quantum Electrodynamics, QED). The evidence collected so far suggests that all phenomena in the microscopic world are governed by a combination of these forces.

The particles of the SM and their properties [5] are summarized in Table 1.1. In the SM the matter fields are fermions and are organized in 3 generations with identical quantum numbers but different masses. Each generation contains three pairs of quarks with strong interaction charge (color) and a colorless doublet with a

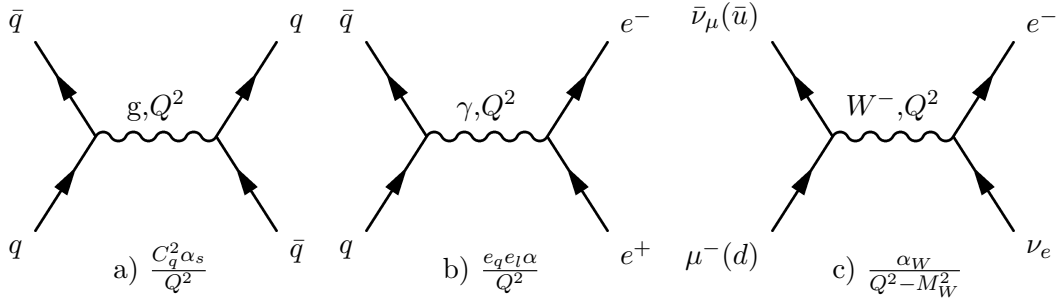


Figure 1.1: *Feynman diagrams for (a) strong, (b) electromagnetic and (c) weak interactions.  $Q^2$  is the square of 4-momentum transferred between the particles.*

neutrino and a charged lepton. The reason for the existence of just three generations is not known. The interactions between matter fermions are mediated by spin 1 particles called gauge bosons. The gauge bosons comprise eight colored gluons of the strong interactions, the photon of the electromagnetic interactions and the  $W^+$ ,  $W^-$  and  $Z^0$  of the weak interactions. A diagram picturing the three exchange interactions is shown in fig. 1.1 along with the corresponding effective coupling constants.

The gluon coupling is proportional to the color charge  $C_q$  and to the coupling constant  $\alpha_s$ . This is similar to the situation in electrodynamics, where the coupling is proportional to the electric charge  $e_q$  and to the fine structure constant  $\alpha$ . However, unlike in QED, the force carriers in QCD are colored, hence self-coupled. As a result of this self-interaction the strong force increases linearly with distance, making quarks tightly bound inside hadrons. The impossibility of separating color charges, such as individual quarks and gluons, is called color confinement. So far, no free quarks or gluons have been observed. They occur only in bound states which are color-neutral. The color charge is conserved. Only a color-neutral pair of color-anticolor quarks can be created in a collision. If the final state quark and antiquark have large energies color confinement degrades their momentum by radiating gluons or quark (parton) pairs. The new partons are approximately collinear with the original parton and combine into mesons or baryons in such a way that a spray of color-less particles is observed which move close to the same direction. This process is referred to as parton *fragmentation*, and the spray of collimated particles is called a jet. Energetic gluons trying to escape the interaction region undergo the same fragmentation process. In the work reported in this thesis an attempt was made to improve the information carried by the hadron jets by studying them in two separate components of the detector, the tracker (sec. 2.4) and the calorimeter

(sec. 2.5).

The coupling constant  $\alpha_s$  in QCD is a function of transferred momentum  $Q^2$ .  $\alpha_s$  decreases with increasing  $Q^2$  and vanishes asymptotically. This leads to the property of QCD called *asymptotic freedom* and allows calculating the strong interaction cross sections perturbatively at high momentum transfer. This is often the case of collisions at the Tevatron, where it is possible to calculate interaction cross sections as perturbative expansions. However, in the process of jets formation the particle energies in the fragmentation process become successively smaller and perturbative QCD is no longer applicable. Phenomenological models are usually applied in order to describe completely jet features.

The weak interaction is mediated by the  $W^\pm$  and  $Z^0$  bosons. Since the force carrier is a massive particle, it follows from the uncertainty principle that this interactions are restricted to a short range

$$\Delta P = M_W \cdot c \Rightarrow \Delta x \sim \frac{\hbar}{M_W \cdot c} < 1 fm$$

	Particle Name	Mass (GeV/ $c^2$ )	Charge	Interaction
Leptons	electron (e)	$511 \otimes 10^{-6}$	$\pm 1$	EM, Weak
	e neutrino ( $\nu_e$ )	$< 2.3 \otimes 10^{-6}$	0	Weak
	muon ( $\mu$ )	$106 \otimes 10^{-3}$	$\pm 1$	EM, Weak
	$\mu$ neutrino ( $\nu_\mu$ )	$< 0.17 \otimes 10^{-3}$	0	Weak
	tau ( $\tau$ )	1.78	$\pm 1$	EM, Weak
	$\tau$ neutrino ( $\nu_\tau$ )	$< 15.5 \otimes 10^{-3}$	0	Weak
Quarks	up (u)	$(1.5-3.3) \otimes 10^{-3}$	$\pm 2/3$	Strong, EM, Weak
	down (d)	$(3.5-6.0) \otimes 10^{-3}$	$\mp 1/3$	Strong, EM, Weak
	charm (c)	$1.27_{-0.11}^{+0.07}$	$\pm 2/3$	Strong, EM, Weak
	strange (s)	$(70-130) \otimes 10^{-3}$	$\mp 1/3$	Strong, EM, Weak
	top (t)	$171.3 \pm 2.1$	$\pm 2/3$	Strong, EM, Weak
	bottom (b)	$4.20_{-0.07}^{+0.17}$	$\mp 1/3$	Strong, EM, Weak
Gauge Bosons	gluon (g)	0	0	Strong
	photon ( $\gamma$ )	0	0	EM
	W boson ( $W^\pm$ )	$80.40 \pm 0.03$	$\pm 1$	Weak
	Z boson ( $Z^0$ )	$91.188 \pm 0.002$	0	Weak

Table 1.1: *Properties of elementary particles in the Standard Model*

The elementary particles of the SM have masses varying over a wide range,

from  $511 \times 10^{-6} \text{ GeV}/c^2$  for an electron to about  $173 \text{ GeV}/c^2$  for the top quark. The generation of the elementary particles mass is tentatively understood via the Higgs mechanism. If gauge symmetry is imposed, the W, Z bosons that mediate the weak interactions are required to be massless as well as the fermion's masses. On the other hand, an explicit mass term in the interaction Lagrangian cannot be accepted because it would violate gauge symmetry. Non-zero mass can be given to the W, Z bosons, while preserving a local gauge symmetry, by spontaneous symmetry breaking. This concept does not rely on mass terms in the Lagrangian, but rather on the assumption that in the physical vacuum a scalar field exists with a specific form such as to assign the correct mass to all particles. Particles acquire mass as a result of the interaction with the Higgs field, which extends over the space-time continuum [6]. The existence of a physical Higgs boson would be the explicit manifestation of this mechanism. At the time being (fall 2009) the Higgs boson has not yet been found.

## 1.2 Electroweak Unification

The first successful quantum field theory was Quantum Electrodynamics (QED), which describes the electromagnetic interactions. As mentioned above, the interaction Lagrangian must be gauge invariant in order for the theory to be renormalizable. QED is a gauge invariant theory described by the U(1) symmetry group. A late major progress was the unification of the electromagnetic and weak interactions described jointly by a  $SU(2) \otimes U(1)$  symmetry group. A brief description of QED, of the unified electromagnetic and electroweak lagrangian, of spontaneous symmetry breaking by the Higgs mechanism and of the progress in understanding strong interactions which lead ultimately to QCD theory is given in appendix A

As a consequence of the Higgs mechanism adopted in the SM to generate spontaneous symmetry breaking, a physical particle, the Higgs boson (“the Higgs”), must exist. Observing the Higgs boson is a must in order to confirm that symmetry breaking is the origin of mass. The SM Lagrangian includes interactions that couple the Higgs to each fermion and gauge boson. This make it possible to produce the Higgs through high energy collisions, and to observe it through its final state decay particles (see sec. 1.5).

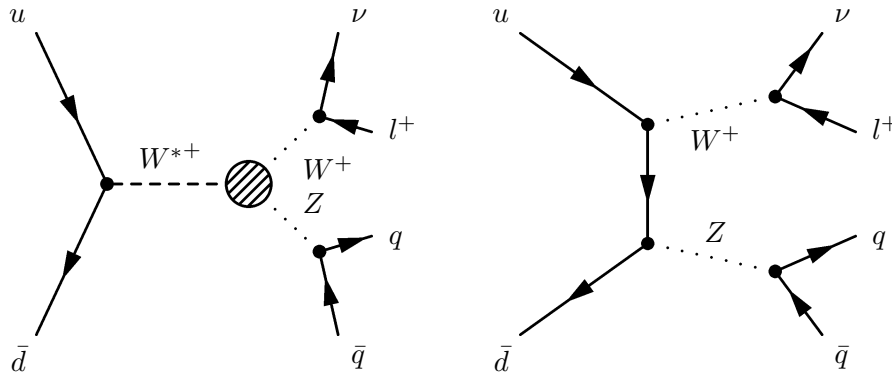


Figure 1.2: *Leading order Feynman diagrams for the process studied in this analysis.*

### 1.3 Associated WZ Production

The work reported in this thesis is an initial step in measuring the production of events containing a W boson that decays leptonically ( $W \rightarrow l\nu$ ,  $l = e$  or  $\mu$ ) in association with a Z boson that decays hadronically ( $Z \rightarrow q\bar{q}$ ). The leading order (LO) Feynman diagrams for these processes are shown in fig. 1.2. Next-to-leading order (NLO) calculations for the production of WZ at  $\sqrt{s} = 1.96$  TeV predict the cross sections  $\sigma(p\bar{p} \rightarrow WZ) = 3.7 \pm 0.3 pb$  [22].

A primary motivation for studying diboson physics is that their production and interactions provide a test of the electroweak sector of the SM. Diboson production can be studied by measuring their interactions and their production cross sections via trilinear gauge-boson couplings (TGC) [23, 24, 28]. The deviation of a TGC or production cross section from the values predicted by the SM would be an indication of new physics beyond the SM and could give a clue about the mechanism responsible for electroweak symmetry breaking. Furthermore, the SM Higgs search is often performed in the diboson channel. One of the most promising channels for discovering a low mass Higgs ( $M_H \lesssim 130 \text{ GeV}/c^2$ ) is in associated production with a W that decays leptonically ( $W^\pm H^0 \rightarrow l\nu b\bar{b}$ ). The Feynman diagrams for  $W^\pm H^0 \rightarrow l\nu b\bar{b}$  are similar to those for  $W^+W^-/W^\pm Z^0 \rightarrow l\nu q\bar{q}$  shown in fig. 1.2. In both cases, the final state particles are a lepton and neutrino from the decay of a W boson and a quark-antiquark pair from the decay of either the Higgs or a weak gauge boson (W or Z). One consequence of this similarity is that  $W^+W^-/W^\pm Z^0 \rightarrow l\nu q\bar{q}$  is an important background for these Higgs searches. Making this direct measurement of diboson production supplies an in situ measurement of the size of this background. An even more important consequence, however, is that detecting WZ in this channel represent a benchmark for Higgs searches with similar final states. The Higgs boson

searches and this analysis share the same challenge of separating a small signal from a large background. Of course, this analysis has the advantage that the signal is in several times larger and that the Z mass is known. Additionally, the ability to discover the Higgs boson (and to measure  $W^+W^-/W^\pm Z^0 \rightarrow l\nu q\bar{q}$ ) depends largely on how precisely a resonance in the dijet invariant mass is reconstructed. A measurement of  $W^+W^-/W^\pm Z^0 \rightarrow l\nu q\bar{q}$  would determine the actual resolution of the measurement of a dijet resonance. Weak diboson production is also a significant background for high mass SM Higgs boson ( $M_H \gtrsim 140 \text{ GeV}/c^2$ ), in which the search focuses on  $H \rightarrow W^+W^-$  decays. As in the low mass Higgs scenario, both the magnitude and the kinematics of diboson production impact the power of the search. In summary one can say that a measurement of  $W^+W^-/W^\pm Z^0 \rightarrow l\nu q\bar{q}$  production provides a “*standard candle*” with which to calibrate and optimize many of the techniques used in SM Higgs searches. The event selection for this search shares most of the trigger, Monte Carlo (MC) simulation, and normalization methods of the  $H \rightarrow b\bar{b}$  search. The multivariate event classification schemes that are becoming increasingly popular in Higgs boson searches can also be checked using a known signal. Finally, the statistical techniques used for the entire SM Higgs mass range can be tested on this known signal, providing opportunities for optimization. To date,  $W^\pm Z^0$  production has been measured using only leptonic decays of both bosons. The reconstruction of  $W^\pm Z^0$  events when the Z decays hadronically represents a challenge for the separation of signal from the dominant backgrounds, a challenge shared by Higgs searches.

## 1.4 Observations of Associated WZ Production at the Tevatron

Already in the Tevatron Run I (1992-1996), with approximately  $100 \text{ pb}^{-1}$  of integrated luminosity accumulated in each experiment, the diboson physics program was started and new limits on the TGC values were set. During Run II more than 50 times the Run I integrated luminosity has been accumulated so far (fall 2009), allowing much more precise measurements and providing better limits. The current status of the WW and WZ production studies at the Run II Tevatron experiments will be reviewed in this section.

The largest statistics was collected on WW production. The WW signature in the leptonic decay is two isolated high- $E_T$  leptons with opposite charge and

large missing transverse energy from the W neutrinos. After the selection cuts, the dominant backgrounds are Drell-Yan, other diboson decays and  $W + jets$  where a jet fakes an isolated lepton. The study of the leptonic WZ production allows one to search for anomalous  $WWZ$  coupling independently of the  $WW\gamma$  coupling, in contrast to WW production. The WZ production has been observed by CDF in October 2006 [25], using  $1.1 fb^{-1}$ . The WZ analysis uses a final state of 3 leptons (electrons or muons) and missing transverse energy. The dominant backgrounds are from  $Z + X$ , where X is a Z,  $\gamma$ , or jet faking a lepton. Figure 1.3 shows the missing transverse energy distribution for candidates both inside and outside the WZ signal region. The measured cross sections for the two processes are summarized in tab. 1.4. All results are compatible with the SM predictions.

Process	Measurement (pb)	NLO (pb)	$\int \mathcal{L} dt$
$\sigma(p\bar{p} \rightarrow WW)$	$13.6 \pm 2.3(stat) \pm 1.6(sys) \pm 1.2(lumi)$	$12.4 \pm 0.8$	$825 pb^{-1}$
$\sigma(p\bar{p} \rightarrow WZ)$	$4.3^{+1.3}_{-1.0}(stat) \pm 0.2(sys) \pm 0.3(lumi)$	$3.7 \pm 0.3$	$1.9 pb^{-1}$

Table 1.2: Double vector boson production in leptonic final states as measured by the CDF Collaboration [25].

Different measures of the semi-leptonic decay of WW and WZ have been performed by CDF [26, 27]. Reference [26] used  $390 pb^{-1}$  of integrated luminosity of data obtaining a cross section of  $\sigma(WW/WZ) = 14.4 \pm 3.1(stat) \pm 2.2(sys)$  pb. Reference [27] reports a cross section of  $\sigma(WW/WZ) = 18.0 \pm 2.8(stat) \pm 2.4(sys) \pm 1.1(lumi)$  pb using the same integrated luminosity.

## 1.5 Higgs Searches

Information on the Higgs mass comes from direct searches or from accurate electroweak measurements that indirectly constrain SM parameters. An experimental lower limit on the Higgs mass comes from LEP experiments [29]. The experiments performed a direct Higgs search using  $2461 pb^{-1}$  of data at a center of mass energy between 189 and 209 GeV. The used channels were  $e^+e^- \mapsto Z^0H$ , with  $Z^0$  decaying into all possible modes and  $H \mapsto b\bar{b}$ , and the channel with  $H \mapsto \tau^+\tau^-$  and  $Z^0 \mapsto q\bar{q}$ .

Figure 1.4 shows a reconstructed Higgs mass distribution. No significant mass peak was found<sup>1</sup>, so a 95% confidence level lower mass limit was established:

$$M_H > 114.4 GeV/c^2 \quad (1.1)$$

<sup>1</sup>The ALEPH experiment claimed some inconsistency of data with background only.

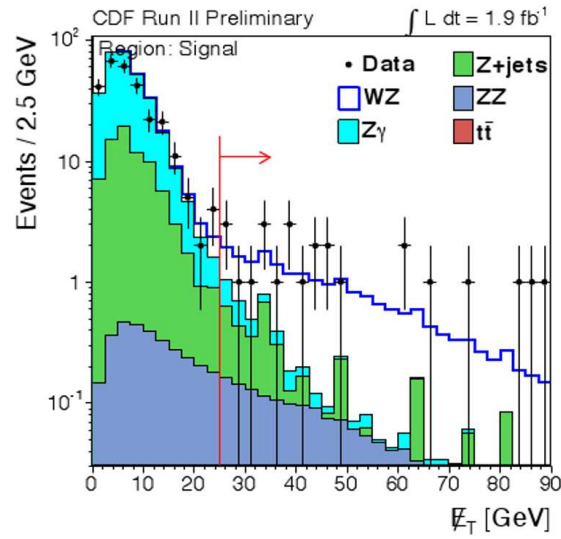


Figure 1.3: Missing  $E_T$  distribution for the  $WZ \rightarrow ll\nu$  process. The signal region (after the red line) contains events with missing  $E_T > 25 \text{ GeV}$ .

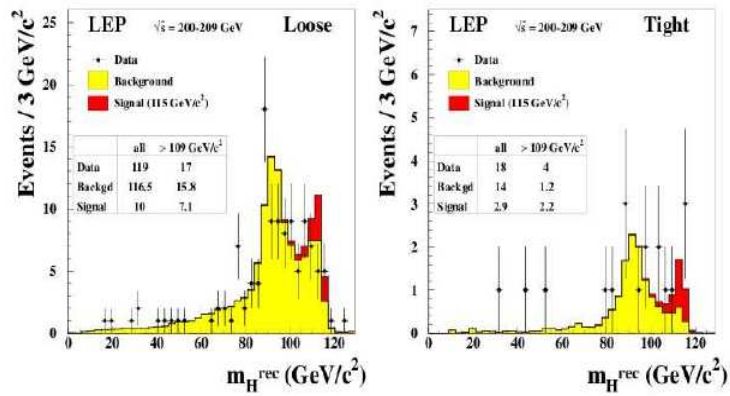


Figure 1.4: Reconstructed Higgs boson mass obtained by the ALEPH experiment at LEP. Monte Carlo predicted background (yellow) and expected Standard Model Higgs boson signal (red) for a mass of  $115 \text{ GeV}/c^2$  is shown together with data.

*Indirect Higgs mass estimates* are made assuming the correctness of SM with the Higgs mechanism included. Accurate mass measurements of the heavier SM particles, like  $W^\pm, Z^0$ , top quark and other electroweak parameters impose theoretical limits on the allowed Higgs mass in order to be consistent with each other. Noticeably the W and Z masses are increased by loop diagram corrections. Figure 1.5 shows the limits on  $M_H$ , derived by  $M_W$  and  $M_{top}$  measurements. Fitting all electroweak measurements performed at LEP, SLD, CDF and DØ with the Higgs mass as a free parameter the  $\Delta\chi^2$  curve in fig. 1.6 is obtained. The preferred value corresponds to the minimum of the curve and gives  $M_H = 87_{-27}^{+37}$  GeV/ $c^2$  at 68% CL. If also LEP-2 limit is included (yellow band in fig. 1.6), one finds:

$$114.4 < M_H < 190 \text{ GeV}/c^2, \quad (1.2)$$

95% CL.

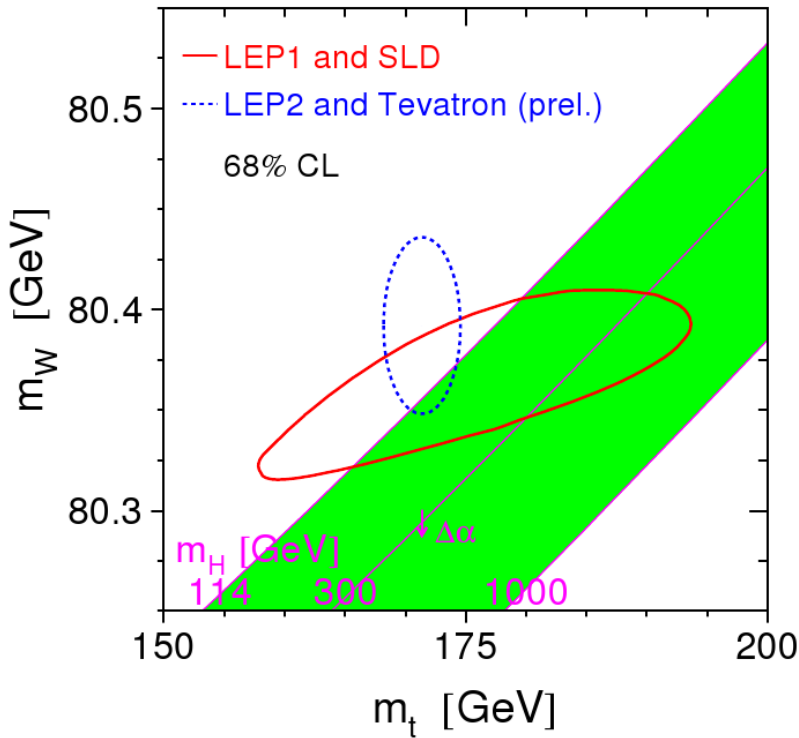


Figure 1.5: SM relationship between  $M_{top}$ ,  $M_W$  and  $M_H$ . Contour curves are obtained varying experimental mass values of  $\pm\sigma$  [29, 30]. The arrow labeled as  $\Delta\alpha$  shows the variation if  $\alpha(M_Z)$  is changed by one standard deviation.

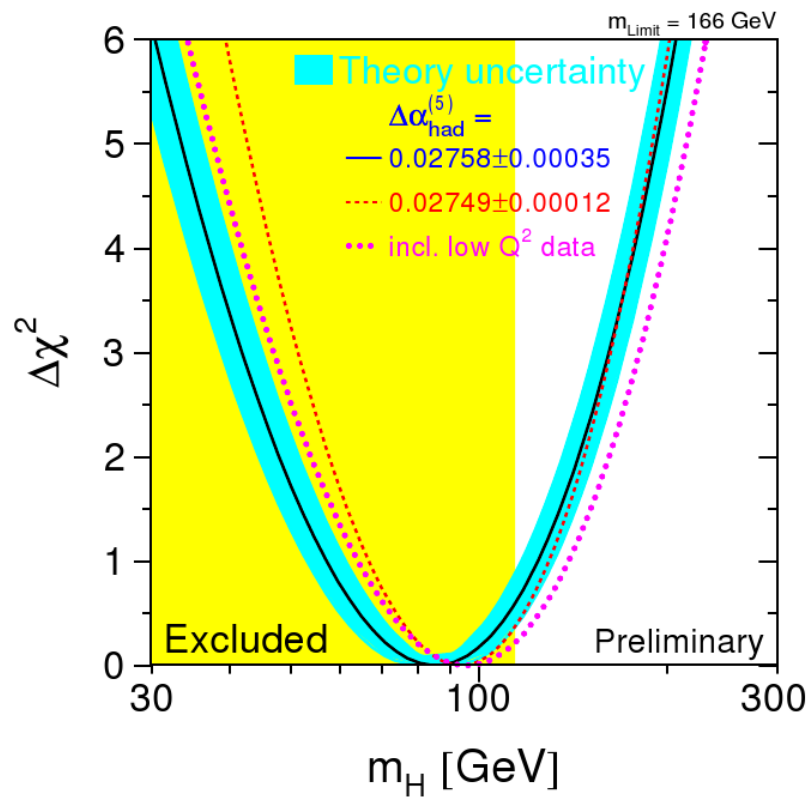


Figure 1.6:  $\Delta\chi^2$  of the global fit to the Standard Model as a function of the Higgs boson mass



## Chapter 2

# The Fermilab Tevatron Collider and the CDF II Detector

*This chapter provides a concise description of the Tevatron Collider and of the CDF II detector where the WZ and WH searches are in progress. Some details are given of the tracking system, of the calorimeters and of the trigger systems, for their crucial importance in the present analysis. A more complete description of the entire detector can be found in [33]*

### 2.1 Tevatron Collider

The Tevatron collider will be the world highest energy accelerator until the CERN Large Hadron Collider will start operating. It provides collisions of antiprotons with protons at a center-of-mass energy of 1.96 TeV. The Tevatron, an underground circular proton synchrotron, is the last stage of a system of accelerators, storage rings, and transfer lines located at the Fermi National Accelerator Laboratory (FNAL or Fermilab), about 50 km west from Chicago, Illinois, United States.

The Tevatron started operating in 1975 as the first superconducting synchrotron. Since the year 2002 it operates only in the collider mode. It employs about 1000 dipole bending magnets with niobium-titanium superconducting coils in a 1 km radius ring. Each dipole magnet is 6.4 m long and is cooled with liquid helium down to 4.3 K. The dipole field reaches 4.2 T. When the machine operates in collider mode, “bunches” of protons spaced by 396 ns collide against a similar beam of antiprotons.

In the two high-luminosity (defined below) interaction points, conventionally

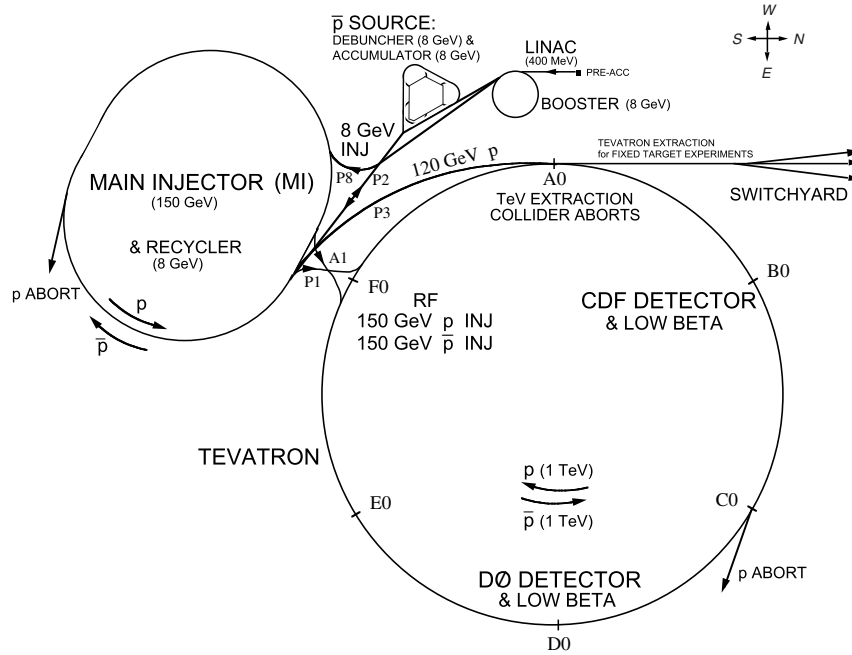


Figure 2.1: The Fermilab accelerator chain.

named  $B\bar{O}$  and  $D\bar{O}$ , the colliding beams are shrunk to a diameter of approximate Gaussian shape with about  $32 \mu m$  width. Each period of Tevatron collider operations is conventionally identified as a Run. The present analysis deals with the data collected in Run II which started in 2002.

The performance of the Tevatron collider is defined in terms of two key parameters: the center-of-mass energy,  $\sqrt{s}$ , and the instantaneous luminosity,  $\mathcal{L}$  (appendix B).

The most important factor determining the luminosity is the antiproton current that can be efficiently transferred through the accelerator chain for final collisions. The particles are accelerated in bunches enclosed in RF buckets. A bucket is one interval of the longitudinal restoring force provided by the RF cavities that results in a stable phase-space where a bunch may be captured and accelerated. During the acceleration process the bunch emittance is reduced (cooling) and trains of bunches are eventually stored and accelerated to top energy in the Tevatron. During a Tevatron run, which can last up to  $\sim 24$  hours, the Tevatron injector chain provides beams for a number of fixed-target experiments (primarily on neutrino beams). The procedure for obtaining a continuous period of collider operation using the same collection of protons and antiprotons (called a store) is described in appendix C.

## 2.2 CDF II Detector

The CDF II detector is a large multi-purpose solenoidal magnetic spectrometer surrounded by full coverage, projective calorimeters and fine-grained muon detectors. The CDF II detector was designed and constructed with an approximately cylindrically symmetric layout both in the azimuthal plane and in the “forward” ( $z > 0$ , east) “backward” ( $z < 0$ , west) directions [38], [39]. It is installed at the  $B\bar{O}$  interaction point of the Tevatron (see fig. 2.2). It comprises a number of coaxial sub-detectors that provide different information by which it is possible to determine energy, momentum and in a number of cases, nature of a broad range of particles produced in 1.96 TeV  $p\bar{p}$  collisions:

- a tracking system composed by three silicon microstrip trackers (LØØ, SVX II and ISL, from inner to outer radii) and an open-cell drift chamber (COT) housed inside a superconducting solenoid providing a 1.4 T magnetic field;
- a time of flight detector, radially outside the COT for particle identification up to momenta of few GeV;
- a set of calorimeters located outside the magnet and used to measure the energy of electrons, photons and hadron jets;
- dedicated detectors used to identify muons that pass through the calorimeters interacting as minimum-ionizing-particles;
- two small angle spectrometers in the very forward and backward regions with respect to the main detector for specialized studies of diffraction processes;
- luminosity monitors.

Several upgrades modified the design of the original detector commissioned in 1985. The most recent upgrade started in 1995 and led to the current detector whose operation is generally referred to as Run II.

A detailed description of the CDF II detector can be found in [33] and in specific references cited there for each sub-detector. In the following, we describe in some detail the tracking and the calorimeters systems, which are the detector components more specific to this analysis. Some information on the remaining components of the CDF II detector are given in appendix D

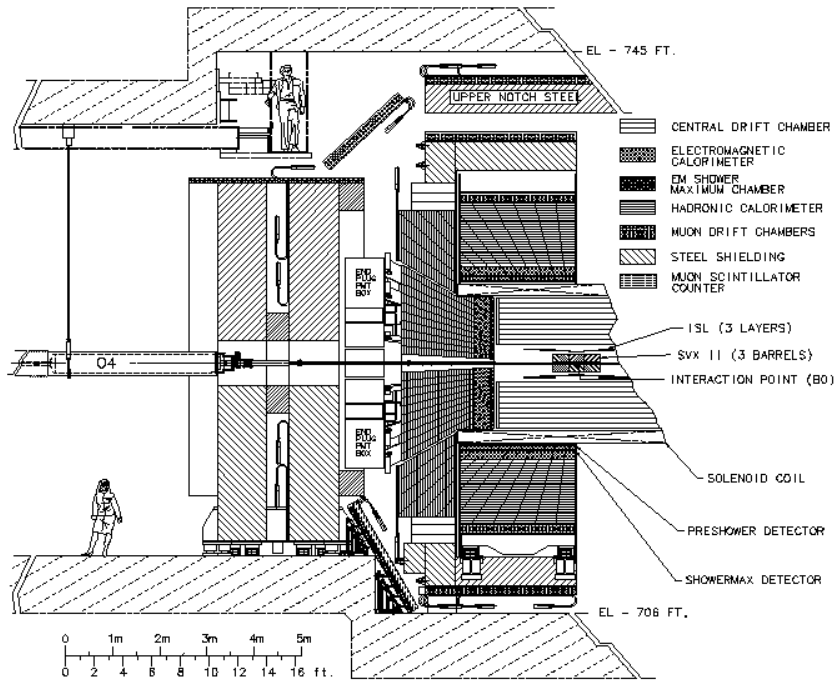


Figure 2.2: Elevation view of one half of the CDF RunII detector: The TOF and the small angle detectors are not pictured, The Central Muon Extension (CEX) and the forward muon detectors are clearly visible on the left side.

## 2.3 Coordinates and Notation

CDF II employs a right-handed Cartesian coordinate system with origin in the  $B\emptyset$  interaction point, assumed coincident with the center of the drift chamber (see sec. 2.4.3). The positive  $z$ -axis lies along the nominal beam-line pointing toward the proton direction (east). The  $(x, y)$  plane is therefore perpendicular to either beams, with the positive  $y$ -axis pointing vertically upward and the positive  $x$ -axis in the horizontal plane of the Tevatron, pointing radially outward with respect to the center of the ring.

Since the colliding beams of the Tevatron are unpolarized, the resulting physical observations are invariant under rotations around the beam line axis. Thus, a cylindrical  $(r, \varphi, z)$  coordinate system is particularly convenient to describe the detector geometry. Throughout this thesis, *longitudinal* means along the proton beam direction (i. e., to the  $z$ -axis), and *transverse* means perpendicular to the beams, i. e., in the  $(x, y) \equiv (r, \varphi)$  plane.

In hadron-collisions environments, it is customary to use a variable invariant under  $\hat{z}$  boosts to describe longitudinal position in the relativistic phase-space, instead

of the polar angle  $\vartheta$ . This variable is the *rapidity* defined as

$$Y = \frac{1}{2} \ln \left[ \frac{E + p \cos \vartheta}{E - p \cos \vartheta} \right], \quad (2.1)$$

where  $(E, \vec{p})$  is the energy-momentum four-vector of the particle.<sup>1</sup> However, a measurement of rapidity requires a detector with full particle identification capability because of the mass term entering  $E$ . Thus, pseudo-spherical coordinates are more commonly used at CDF by replacing  $Y$  with its approximate expression  $\eta$  in the ultra-relativistic limit, usually valid for products of high-energy collisions except at the most forward angles:

$$Y \xrightarrow{p \gg m} \eta + \mathcal{O}(m^2/p^2), \quad (2.2)$$

where the *pseudo-rapidity*  $\eta \equiv -\ln[\tan(\vartheta/2)]$  is only function of the polar angle. As the event-by-event longitudinal position of the interaction is distributed around the nominal interaction point with 30 cm r.m.s. width, it is useful to distinguish *detector pseudo-rapidity*,  $\eta_{\text{det}}$ , measured with respect to the (0, 0, 0) nominal interaction point, from *event pseudo-rapidity*,  $\eta$ , which is measured with respect to the  $z_0$  position of the event vertex where the particle originated.<sup>2</sup>

Mapping the solid angle in terms of (pseudo)-rapidity and azimuthal angle is also convenient because the density of final-state particles in energetic hadronic collisions is approximately flat in the  $(Y, \varphi)$  space. Other convenient variables used are the transverse component of the momentum with respect to the beam axis ( $p_{\text{T}}$ ), the “transverse energy” ( $E_{\text{T}}$ ), and the approximately Lorentz-invariant distance in the  $\eta - \varphi$  space  $\Delta R$ , respectively defined as

$$\vec{p}_{\text{T}} \equiv (p_x, p_y) \rightarrow p_{\text{T}} \equiv p \sin(\vartheta), \quad E_{\text{T}} \equiv E \sin(\vartheta), \quad \text{and} \quad \Delta R \equiv \sqrt{\Delta\eta^2 + \Delta\varphi^2}. \quad (2.3)$$

Throughout this thesis, the magnitude of the vector  $\vec{p}_{\text{T}}$  (and of any vector  $\vec{v}$ ) is indicated as  $p_{\text{T}}$  ( $v$ ).

---

<sup>1</sup>The rapidity can be derived from the Lorentz-invariant cross-section:  $E \frac{d^3\sigma}{(dp)^3} = E \frac{d^2\sigma}{\pi p_{\text{T}} dp_{\text{T}} dp_z}$ . Observing that only  $E$  and  $p_z$  change under  $z$  boosts, we can replace them by a variable  $Y$  such as  $E \frac{dY}{dp_z} = 1$ . Solving for  $Y$  we get eq. (2.1).

<sup>2</sup>An idea of the difference is given by considering that  $|\eta_{\text{det}} - \eta_{\text{part}}| \approx 0.2$  if the particle is produced at  $z = 60$  cm from the nominal interaction point.

## 2.4 The Tracking System

Three-dimensional charged particle tracking is achieved through an integrated system consisting of three silicon inner subdetectors and a large outer drift-chamber, all contained in a superconducting solenoid. The 1.4 T magnetic field and the 136 cm total lever arm provide excellent tracking performances (see fig. 2.3).

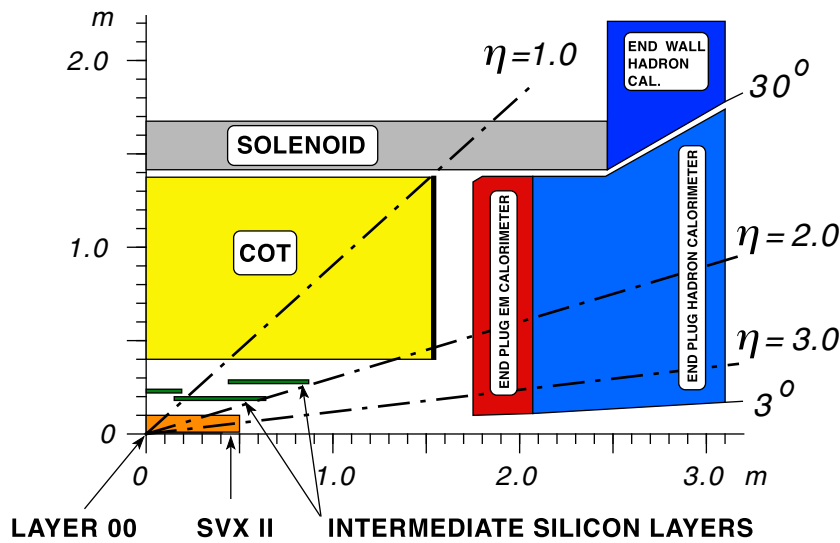


Figure 2.3: Elevation view of one quadrant of the inner portion of the CDF II detector showing the tracking volume surrounded by the solenoid and the forward calorimeters.

In the central region ( $|\eta_{\text{det}}| \lesssim 1$ ), seven silicon samplings (one in the  $(r, \varphi)$  view and six in the  $(r, \varphi, z)$  view), and 96 chamber samplings (48  $(r, \varphi)$  plus 48  $(r, z)$ ) are available between 1.6 and 132 cm. In the forward and backward regions ( $1 \lesssim |\eta_{\text{det}}| \lesssim 2$ ), 8 silicon samplings (one in the  $(r, \varphi)$  view and seven in the  $(r, \varphi, z)$  view) are available between 1.6 and 29 cm, along with partial information from the chamber.

The high number of samplings over the 88 cm lever arm of the chamber ensure precise determination of curvature, azimuth, and pseudo-rapidity of the tracks in the central region. The chamber provides also track seeds for pattern-recognition in silicon.

### 2.4.1 The Superconducting Solenoid

The CDF II detector employs a superconducting solenoid for momentum measurements. This solenoid generates a 1.4 T nearly uniform magnetic field. It is oriented along beam direction and operated with a 4650 A current (current density 1150 A/m) through 1164 turns of an aluminum-stabilized NbTi/Cu super-conducting coil. The solenoid is 4.8 m in length, 1.5 m in radius,  $0.85X_0$  in radial thickness<sup>3</sup> (for normally incident particles), and is cooled by forced flow of two-phases helium. Outside the coil, the return of the field flux is a box-shaped steel yoke, 9.4 m high by 7.6 m wide by 7.3 m long. It is shaped such as to avoid interference between the field and the proper operations of the photo-multiplier tubes (PMT) used in the calorimeters.

### 2.4.2 Silicon System

The LØØ, SVXII, and ISL detectors constitute the silicon tracking system. The total amount of material in the silicon system, averaged over  $\varphi$  and  $z$ , varies roughly as  $\frac{0.1X_0}{\sin(\vartheta)}$  in the  $|\eta_{\text{det}}| \lesssim 1$  region, and roughly doubles in  $1 \lesssim |\eta_{\text{det}}| \lesssim 2$  because of the presence of cables, cooling bulk-heads, and portions of the support frame. The average amount of energy loss for a charged particle crossing the detector at  $90^\circ$  is  $\sim 9$  MeV. To prevent thermal expansion, relative detector motion, increased leakage-current, and chip failure due to thermal heating, the silicon detectors and the associated front-end electronics are held at roughly constant temperature ranging from  $-6^\circ\text{C}$  to  $-10^\circ\text{C}$  for LØØ and SVXII, and around  $10^\circ\text{C}$  for ISL, by an under-pressurized water and ethylene-glycol coolant flowing in aluminum pipes integrated in the supporting structures.<sup>4</sup>

#### Layer ØØ

The “innermost” tracker, i. e., the Layer ØØ (LØØ), is a light-weight silicon layer placed on the beam-pipe at radii, alternating in  $\varphi$ , of 1.35 or 1.62 cm from the beam, [42]. It provides full azimuthal and  $|z| \lesssim 47$  cm longitudinal coverage and recovers the degradation in resolution of the reconstructed vertex position due to multiple scattering, which is particularly significant on the SVXII read-out electronics and cooling system, installed within the tracking volume. The complete silicon tracking

<sup>3</sup>The symbol  $X_0$  indicates the radiation length.

<sup>4</sup>The pressure of the cooling fluid is maintained below the atmospheric pressure to prevent leaks in case of damaged cooling pipes.

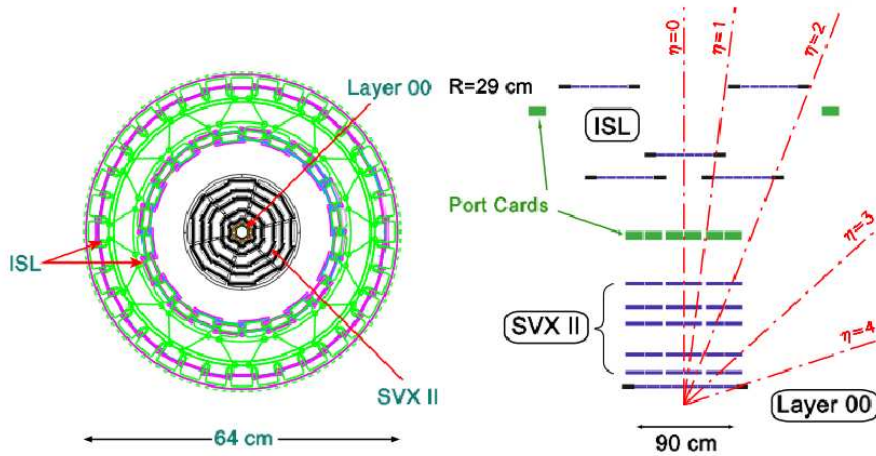


Figure 2.4: Longitudinal coverage of the silicon trackers (right) and cross section view of the integrated SVXII-ISL tracking system (left).

detector is sketched in fig. 2.4

### Silicon Vertex detector II

The core of the silicon tracker is the Silicon Vertex detector (SVXII). It is a fine resolution silicon micro-strip vertex detector which provides five three-dimensional measurements that extend the COT lever arm by 41.5 cm toward the beam thus (see fig. 2.3) allowing more precise determination of the trajectories and identification of decay-vertices displaced from the beam-line with full pseudo-rapidity coverage in the  $|\eta_{\text{det}}| \lesssim 2$  region (see fig. 2.5(a)) [40]. This corresponds to a length of  $|z| \lesssim 96$  cm along the beam-line, sufficient to cover the  $\sigma_z \approx 28$  cm longitudinal spread of the luminous region. The SVXII has an approximate cylindrical geometry coaxial with the beam. Its mechanical layout is segmented in three 32 cm axial sections (“barrels”)  $\times$  twelve  $30^\circ$  azimuthal sectors (“wedges”)  $\times$  five equally-spaced radial layers. A small overlap between the edges of adjacent azimuthal sectors helps wedge-to-wedge alignment (see fig. 2.5(b)).

Sensors in a single layer are arranged into independent longitudinal read-out units, called “ladders”.

### Intermediate Silicon Layers (ISL)

The Intermediate Silicon Layers (ISL), is a silicon tracker placed at intermediate radial distance between the SVXII and the drift chamber (see fig. 2.3), and covering

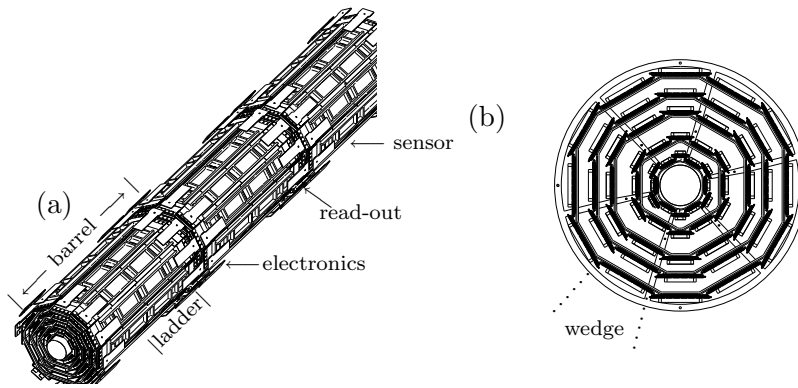


Figure 2.5: Schematic illustration of the three instrumented barrels of SVXII (a) and of the cross-section of a SVXII barrel in the  $(r, \varphi)$  plane (b).

the  $|\eta_{\text{det}}| \lesssim 2$  pseudo-rapidity range for a total length of 174 cm along  $z$  [41]. The ISL allows efficient linking between tracks reconstructed in the chamber and hits detected in the SVXII. It also extends the track finding to pseudo-rapidities  $1 \lesssim |\eta_{\text{det}}| \lesssim 2$ , where the chamber coverage is marginal: at  $|\eta_{\text{det}}| \lesssim 1$  a single layer of silicon sensors is mounted on a cylindrical barrel at radius of 22.6 (or 23.1 cm). At  $1 \lesssim |\eta_{\text{det}}| \lesssim 2$  two layers of silicon sensors are arranged into two pairs of concentric barrels (inner and outer).

### 2.4.3 Central Outer Tracker

The main tracker at CDF is the Central Outer Tracker (COT), a cylindrical multi-wire open-cell drift chamber that provides charged particle tracking in the central pseudo-rapidity region ( $|\eta_{\text{det}}| \lesssim 1$ , see fig. 2.3) [43]. Charged particles in the solenoidal magnetic field perform helical paths whose radius measures their momentum. The internal radius of the COT sensitive volume is 44 cm, the external one is 132 cm and the COT total length is 3.1 m. The COT is filled with an  $Ar - Ethane - CF_4$  mixture (in the proportion 50:35:15) that provides fast drift of ionization electrons ( $\approx 100 \mu\text{m}/\text{ns}$ ). The maximum drift time in the COT cells is 100 ns, less than the originally planned time interval between bunch crossings (132 ns, with 108 circulating bunches). The single hit resolution is about  $110 \mu\text{m}$ . The COT cells are grouped in 8 superlayers (fig. 2.6), 4 with axial wires and 4 with stereo wires, having alternatively a  $\pm 3^\circ$  tilt with respect to the  $z$  axis. The number of cells per superlayer increases from 168 in the innermost SL1 to 480 in SL8. Each cell contains 12 gold-plated tungsten potential wires and 12 sense wires (fig. 2.6).

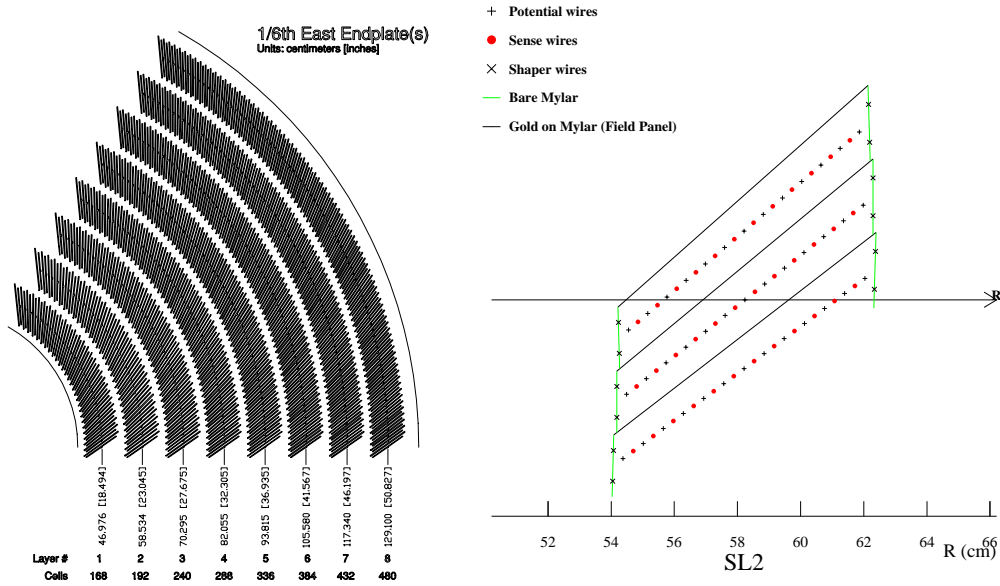


Figure 2.6: A 1/6 section of the COT end-plate (a). For each super-layer is given the total number of cells, the wire orientation (axial or stereo), and the average radius [cm]. The enlargement shows in details the slot were wire planes (sense) and field sheet (field) are installed (b). The arrow shows the radial direction.

The cells themselves are tilted in azimuth by  $35^\circ$  respect to the radial direction to allow the Lorentz force to drift ionization in the direction transverse to the radius for optimal momentum resolution. The total amount of material in the COT, including the gas mixture, corresponds to 0.017 radiation lengths for electrons. The COT is read by 30240 linear electronic channels and is capable of measuring  $\left(\frac{dE}{dx}\right)$  besides charged particles momenta.

## 2.5 Calorimeters

Located immediately outside the solenoid, the calorimeter system at CDF covers a solid angle of nearly  $4\pi$  around  $p\bar{p}$  interaction point up to  $|\eta_{\text{det}}| \lesssim 3.6^5$ . It measures the energy flow from hadrons, electrons, or photons, using “shower” sampling [45] based on layers of high- $Z$  passive absorber interspersed with layers of plastic scintillator. Neutrino transverse momenta are measured via transverse energy imbalance

<sup>5</sup>However, between detector sections there are regions (“cracks”) where the response is poor.

in the event.<sup>6</sup> The calorimeters are segmented in solid angle around the nominal collision point and segmented into two compartments radially outward from the collision point (in-depth segmentation). Angular segmentation is organized in projective *towers*. Each tower is an independent read-out unit which subtends a portion of the solid angle, namely a rectangular cell in the  $(\eta_{\text{det}} - \varphi)$  space, with respect to the nominal interaction point. In-depth segmentation of each tower consists of two independent compartments: the inner one samples the electromagnetic component of the shower, while the outer one samples the hadronic fraction of the deposited energy. Different fractions of energy release in the two compartments distinguish photons and electrons from hadrons.

### 2.5.1 Electromagnetic Calorimeter

Electrons and photons are identified and have their energy sampled in the EM calorimeter by a set of thin scintillator layers interspread with lead absorbers. The EM calorimeter is split into three parts: the central EM calorimeter (CEM) covering the region  $|\eta_{\text{det}}| \lesssim 1.1$  and the two plug EM calorimeters (PEM) covering the forward regions  $1.1 < |\eta_{\text{det}}| < 3.6$ .

#### CEM

In the  $|\eta_{\text{det}}| \lesssim 1.1$  region, the electromagnetic calorimeter appears as an hollow cylinder occupying the radial region between 173 and 208 cm [46]. It is split into 12 azimuthal  $15^\circ$ -wide sectors (see fig. 2.7(a)). Each sector is divided into ten  $\eta_{\text{det}}$  towers ( $\Delta\eta_{\text{det}} \times \Delta\varphi \approx 0.11 \times 15^\circ$  per tower). To maintain a constant thickness in  $X_0$ , compensating the  $\sin(\vartheta)$  variation from tower to tower, some lead layers are replaced with increasing amounts of acrylic as a function of  $\eta_{\text{det}}$ .<sup>7</sup> The blue light from each tower is collected, wave-length shifted into green light by sheets of acrylic plastic placed on the azimuthal tower boundaries, and guided to two phototubes per tower. The two outer towers in one wedge are missing to allow accessing the solenoid for check and repairs if needed. The total number of instrumented towers is 478. At a radial depth of  $5.9X_0$ , where the peak of shower development is typically located, an array of multi-wire proportional chambers measures the transverse shower shape with 2.0 mm resolution (for 50 GeV electrons). In Run I a layer of multi-wire

<sup>6</sup>See pag. 17 for a definition of transverse energy of a particle. The total transverse energy is the sum over the entire calorimeter  $\vec{E}_T \equiv \sum_i \vec{E}_T^i$ .

<sup>7</sup>The number of lead layers varies from 30 in the innermost ( $|\eta_{\text{det}}| \approx 0.06$ ) tower to 20 in the outermost ( $|\eta_{\text{det}}| \approx 1.0$ ).

proportional chambers was located in a 5cm gap between the outer surface of the solenoid and the first layer of the calorimeter to monitor photon conversions started in the tracker material or in the solenoid (“preshower detector”). During the fall 2004 shut-down, this system was replaced with a finely segmented layer of scintillator tiles [47].

The total thickness of the electromagnetic section corresponds to approximately  $19X_0$  ( $\sim 1\lambda_{\text{int}}$ , where  $\lambda_{\text{int}}$  is the pion nuclear absorption length in units of  $\text{g cm}^{-2}$ ), for an energy resolution of<sup>8</sup>:

$$\frac{\sigma_E}{E} = \frac{13.5\%}{\sqrt{E_T}} \oplus 2\% \quad (2.4)$$

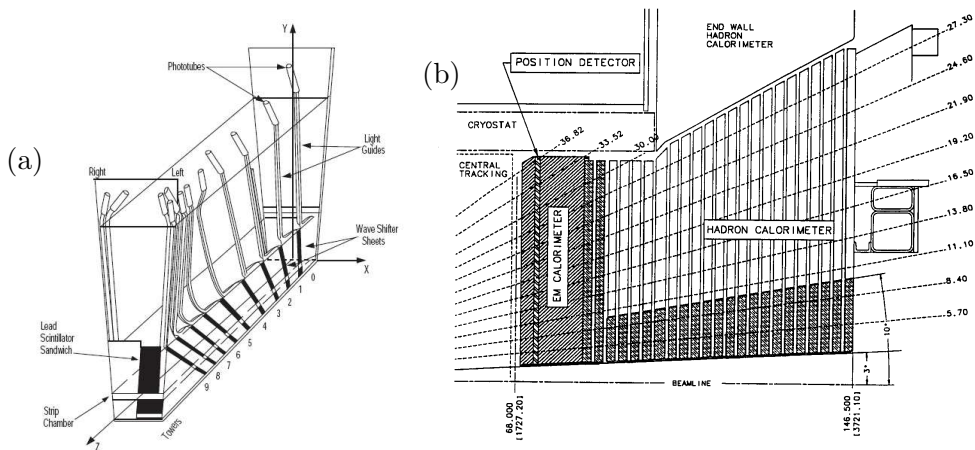


Figure 2.7: Schematic illustration of an azimuthal sector of the central electromagnetic calorimeter (a). Elevation view of one quarter of the plug calorimeter (b).

## PEM

The electromagnetic coverage is extended in the region  $1.10 \lesssim |\eta_{\text{det}}| \lesssim 3.64$  by a separate scintillating tile calorimeter (see fig. 2.7(b)) [49].

The PEM calorimeter has a similar structure as the CEM: 22 layers of 4.5 mm thick lead alternate with 22 layers of 4 mm thick scintillator. The PEM tower segmentation is  $7.5^\circ$  in  $\varphi$  for  $|\eta_{\text{det}}| \lesssim 2.11$  and  $15^\circ$  for  $2.11 < |\eta_{\text{det}}| < 3.6$ . The seg-

<sup>8</sup>The first term is called the “stochastic” term and derives from the intrinsic fluctuations of the shower sampling process and of the PMT photo-electron yield. The second term, added in quadrature, depends on the calorimeter non-uniformities and on the uncertainty of the calibrations. Energies are in GeV.

mentation in  $\eta_{\text{det}}$  can be understood by an inspection of fig. 2.7(b). Each scintillator tile is coupled to a different PMT, except for the first layer which is a 1 cm thick plane of scintillator bars read by a multi-anode PMT and acting as a preshower detector. The total thickness of the PEM section corresponds to approximately  $21X_0$  ( $1\lambda_{\text{int}}$ ), for an energy resolution of:

$$\frac{\sigma_E}{E} = \frac{16\%}{\sqrt{E_T}} \oplus 1\% \quad (2.5)$$

Also the PEM is equipped with a shower maximum detector (PES), made of three planes of scintillator strips rotated by  $60^\circ$  and providing a spatial resolution of about 1 mm on the shower location.

## 2.5.2 Hadronic Calorimeter

The identification of hadrons and the measurement of their energy are performed by a set of calorimeter towers located behind the EM ones: the central hadronic calorimeter (CHA), covering the region  $|\eta_{\text{det}}| < 0.9$ , two calorimeter rings that cover the gap between CHA and PHA in the region  $0.7 < |\eta_{\text{det}}| < 1.3$ , called the wall hadron calorimeters (WHA) and the two plug hadron calorimeters (PHA) covering the forward regions  $1.3 < |\eta_{\text{det}}| < 3.6$ .

### CHA and WHA

The large angle hadronic compartment comprises two subsystems: the central ( $|\eta_{\text{det}}| \lesssim 0.9$ ) and the end-wall ( $0.7 \lesssim |\eta_{\text{det}}| \lesssim 1.3$ ) section [48]. They consist of four ‘‘C’’-shaped arches for a total of 48 azimuthal sectors. Each central wedge is segmented into nine  $\eta_{\text{det}}$  towers matching in size and position the electromagnetic towers, for 384 towers in total. The end-wall section has six additional  $\eta_{\text{det}}$  towers, three of which matching the outer central hadronic towers (see fig. 2.2) for a total number of 288 towers. A central hadronic tower is constructed of 32 layers of steel absorber, 2.5 cm thick, alternating radially with 1.0 cm-thick acrylic scintillator. It is composed by two parts joining at  $z=0$ . The technology of the WHA is similar to CHA one, but contain only 15 layers of 5.1 cm-thick absorber.

The total thickness of the hadronic section is approximately constant in the  $|\eta_{\text{det}}| < 1.3$  region and corresponds to approximately  $4.5\lambda_{\text{int}}$ . The total number of projective towers of CHA+WHA is 12, out of which 6 are entirely contained in the CHA, 3 are entirely contained in the WHA and 3 are shared between the two. Each

tower element is read by 2 photomultipliers. The resolutions of CHA and WHA found in test beam measurements (response to single pions) are ([48]):

$$CHA : \frac{\sigma_E}{E} \approx \frac{50\%}{\sqrt{E}} \oplus 3\% , WHA : \frac{\sigma_E}{E} \approx \frac{75\%}{\sqrt{E}} \oplus 4\% . \quad (2.6)$$

### PHA

The Plug Hadron calorimeter (PHA) is located behind the PEM [49] and has the same tower segmentation (fig. 2.7(b)). The technology is the same as of CHA, with 23 layers alternating 2 cm thick steel absorber and 6 mm thick scintillator, for a total amount of material corresponding to  $7\lambda_{\text{int}}$ . Its resolution in single pion test beam was found to be ([49]):

$$PHA : \frac{\sigma_E}{E} \approx \frac{80\%}{\sqrt{E}} \oplus 5\% \quad (2.7)$$

Information on other component of the CDF II detector is given in appendix D

## 2.6 Trigger and Data Acquisition System

Since  $1 \mu\text{b} = 1 \text{ Hz}$  at  $\mathcal{L} = 10^{30} \text{ cm}^{-2}\text{s}^{-1}$ , we obtain that at a Tevatron instantaneous luminosity  $\mathcal{L} \approx 3 \times 10^{32} \text{ cm}^{-2}\text{s}^{-1}$ , and with an inelastic  $p\bar{p}$  cross-section of  $\sigma_{p\bar{p}\text{-in.}} \approx 60 \text{ mb}$ , one expect approximately  $1.8 \times 10^7$  inelastic collisions per second, corresponding to one inelastic  $p\bar{p}$  interaction per bunch crossing on average. Since the read-out of the entire detector needs about 2 ms, after the acquisition of one event, another approximately 5,000 interactions would occur and remain unrecorded. Clearly this is unacceptable. The detector front-end electronics must be designed as to solve this problem and reduce the event loss to a few percents. The percentage of events which are rejected solely because the trigger is busy processing previous events is referred to as trigger *deadtime*.

On the other hand, the average size of the information associated to each event from the  $\mathcal{O}(10^6)$  total CDF II channels is 140 kbytes. Even in case of deadtime-less read-out of the detector, in order to record all events an approximate throughput and storage rate of 350 Gbyte/s would be needed, largely beyond the possibilities of currently available technology.

However, since the cross-sections of most interesting processes are  $10^3$ – $10^{12}$  times smaller than the inelastic  $p\bar{p}$  cross-section, the above problems may be overcome

with an on-line preselection of the most interesting events<sup>9</sup>. This is the task of the trigger system, which evaluates on-line the information provided by the detector and discards the uninteresting events.

The CDF II trigger is a three-level system that selectively reduces the acquisition rate, with virtually no deadtime, i. e., keeping each event in the trigger memory for a time sufficient to allow for a trigger decision without inhibiting acquisition of the following events (see fig. 2.8). Each level receives the accepted event from the previous one and, making use of detector information of increasing complexity and with more time for processing, applies a logical “OR” of several programmable selection criteria to make its decision.

Prior to any trigger level, the bunched structure of the beams is exploited to reject cosmic-ray events by gating the front-end electronics of all subdetectors in correspondence of the bunch crossing. For each crossing, data enter the pipeline for read-out and eventual use at Level-2, and a Level-1 decision on a preceding crossing is made before the corresponding data reach the end of the pipeline. The Level-1 has  $132 \text{ ns} \times 42 \simeq 5.5 \mu\text{s}$  to make its decision before the contents of the buffer is deleted. On a Level-1 accept, the data from the Level-1 buffer are passed to the four-cell Level-2 buffer integrated in the front-end electronics of each subdetector, and the event is queued for a Level-2 decision. While data in a Level-2 buffer are being processed, they cannot be overwritten by incoming data corresponding to a subsequent Level-1 accept. If a Level-1 accept occurs while all four Level-2 buffers are occupied, trigger deadtime is incurred. The  $\simeq 20 \mu\text{s}$  latency of the Level-2 decision is less than approximately 80% of the average time between Level-1 accepts, to minimize deadtime. On a Level-2 accept, the entire detector is read-out, thereby emptying a cell in all detector buffers for the next event; the event is queued for read-out in Level-3 and for eventual storage to permanent memory.

Some more details on the operation of the three trigger levels are given in appendix E

## 2.7 CDF Software Framework

The CDF experiment uses a custom object-oriented software to manage data acquisition, offline event reconstruction and most of the analysis. The C++ language

---

<sup>9</sup>Examples are the  $b\bar{b}$  production cross section which is  $\sim 0.1 \text{ mb}$  and the  $t\bar{t}$  production cross section which is  $\sim 7 \text{ pb}$

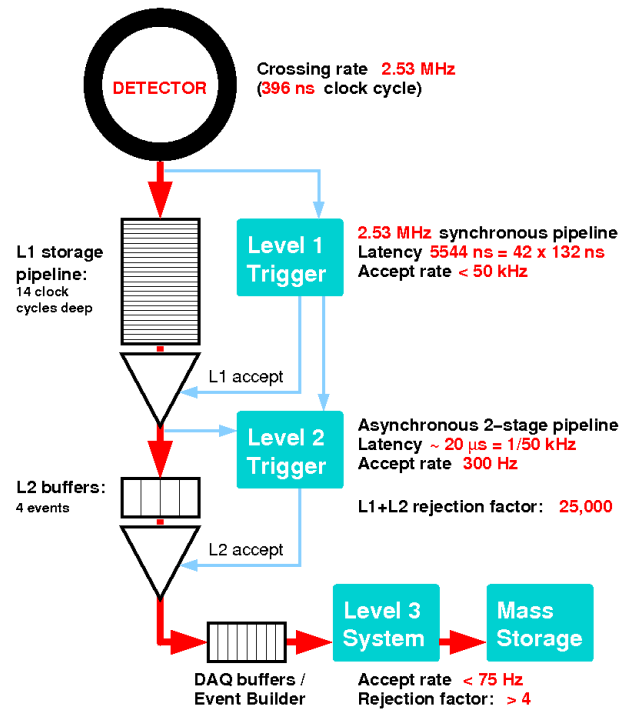


Figure 2.8: Functional block diagram of the CDF II trigger and data acquisition system.

is used to define objects, i.e self-consistent structures containing properties and definition common to all entries of the same kind. Usually an *object* is a physics interesting quantity. It can be simple, as a track reconstructed with a particular algorithm or the energy deposit in the calorimeters, or more complex, like a “jet object”, that will contain links to tracks, calorimeter energy deposits, vertex information and much more.

All the objects characterizing a reconstructed event are stored into large arrays (“n-tuples”) suitable for high level analysis which is performed with “ROOT” [57], an object oriented data analysis framework. The different objects are collected in AC++ *modules* that make easier to do parallel studies and upgrades. However all analysis streams start from a common stable framework. When a large set of new features is available, a new stable “generation” (or “Gen”) of the CDF software is released. At this point in time the CDF collaboration is using *Gen6* while *Gen7* is near to be fully tested. The release of a new generation improves several aspects of CDF analysis because, as time goes on, new algorithms are implemented and a better knowledge of the detector is obtained. Unfortunately, all the data acquired

before the date of the new release as well as all the Monte Carlo events need to be reprocessed with the new software and some older analysis may need adjustments because of backward compatibility problems. This is called “production” and is a time and CPU consuming task.

## 2.8 Monte Carlo Simulation of Detector and Trigger

An accurate simulation of physics events and of the expected detector response are of fundamental importance in many analyses. The Monte Carlo samples simulating the physics processes are produced with a three steps approach.

**Parton level:** the matrix element of the process is computed with numerical integration of leading-order (LO) or next-to-leading order (NLO) amplitude. The ALPGEN<sup>10</sup> amplitude generator [58] is used for many physics processes of interest for our work. In order to reproduce the final state, it is interfaced to the generator PYTHIA<sup>11</sup> [59] (see below) to include jet fragmentation. Full *PYTHIA* including generator is also used for some physics processes (for example for top quark pair production). For this study PYTHIA was used to produce the signal sample ( $WZ$ ,  $W \rightarrow l\nu$ ,  $Z \rightarrow q\bar{q}$ ). At CDF it is also possible to use HERWIG[60] to produce physics processes. This is done in a number of checks on Monte-Carlo-induced systematic uncertainties.

**Particles level:** higher order or non-perturbative processes are simulated on the basis of analytical approximations and QCD-inspired models. Parton shower programs like PYHTIA and HERWIG can be used to simulate quark hadronization, soft gluon emission or multi-parton interactions within a hard process, i.e. spectator quark interactions and accompanying soft interactions within the same bunch crossing.

**Detector level:** usually, the intricate detector geometry and the numerous effects that need to be accounted for in predicting detector response make the analytical derivation of the event observables impractical or impossible. Monte Carlo techniques are widely-used to address this problem. The detector geometry and material are modeled using the version 3 of the GEANT package [61] tuned to test-beam and collision data. GEANT receives in input the positions, the four-momenta, and the identity of all particles produced by the simulated collisions that exit the beam pipe. It simulates their passage in the detector, modeling their interactions

---

<sup>10</sup>The version used is 2.1

<sup>11</sup>The version used is 6.216. When used together ALPGEN the version of PYTHIA MC is 6.325

(bremsstrahlung, multiple scattering, nuclear interactions, photon conversions, etc.) and the consequent generation of signals in the detector channels.

Next, the actual trigger logic is simulated. The simulated output data have the identical structure as collision data, allowing their analysis with the same reconstruction programs used for collision data. Further details on CDF simulation can be found in [56].

## Chapter 3

# Identification and Definition of Objects

*The raw outputs of several CDF subdetectors must be combined in order to reconstruct the physical objects such as leptons or hadron jets, that are of interest in the analysis. Refinements of object reconstruction are possible and some of them are explained later in the work.*

### 3.1 Track Reconstruction

The ability to detect and reconstruct charged particle trajectories is essential for particle identification and momentum measurement. Precise, high efficiency tracking plays a central role for charged lepton identification. Photons give electron-like signals in the electromagnetic calorimeter but have no associated track, and can be identified by this signature. Track reconstruction in the silicon tracker allows precise measurement of track impact parameter, and thus the identification of long-lifetime heavy-flavor hadrons in jets.

In a uniform axial magnetic field, neglecting the energy loss by ionization in the detector material, the trajectory of a charged particle is described by an helix (see Fig. 3.1). The reconstruction of a charged-particle trajectory consists in determining the helix parameters through a fit of a set of spatial measurements (“hits”) in the tracking detectors (COT and silicon detectors, see section 2.4) reconstructed by clustering and pattern-recognition algorithms. The helical fit takes into account field non-uniformities and scattering in the detector material. The equations describing the helix are given in appendix F.

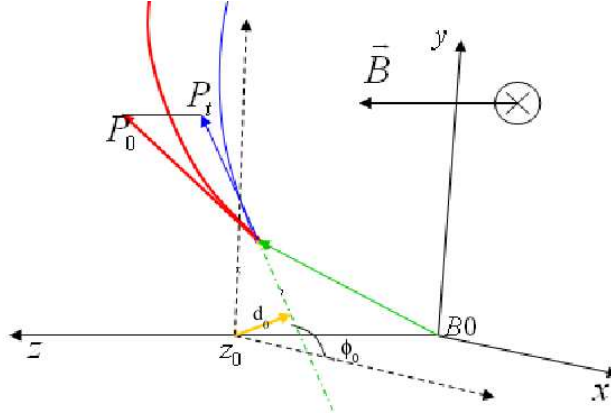


Figure 3.1: *Helix parameters in the solenoid field and coordinate system.*

### 3.1.1 Tracking Algorithms

The experiment exploits several tracking algorithms[63], each optimized for the information available in different detector region. In the following paragraphs we describe the main features of the relevant tracking algorithms used at CDF.

#### COT Tracking

Track pattern recognition in the COT is performed in four steps. The first step is the segment finding: each of the 8 COT superlayers is searched for groups of three aligned hits, which are fitted to a straight line with the method of the least squares. All hits closer than 1 mm to the fitted 3-hits seed line (1 mm road) are attached to the line and the fit is repeated. Tracks are reconstructed from the information of the axial superlayers only, with either one of two different algorithms. One algorithm (“segment linking”) links segments in different superlayers and fits them to a circle with the minimum  $\chi^2$  method. The other one (“histogram linking”, [64]) starts with a default circle defined by one COT segment and the beam axis, fills a 200  $\mu\text{m}$  binned histogram with the distance from the center of the circle of all hits in 1 cm wide road. If the most populated bin contains at least 10 hits, those hits are added to the track. The “histogram linking” algorithm ends with the attempt of adding more hits in a 750  $\mu\text{m}$  road around the track and refitting it. If a track is reconstructed by both algorithms, duplicates are removed. The third step in COT track reconstruction is the addition of stereo hits. For each axial track, a “segment linking” algorithm tries to attach stereo hits from the outer superlayer, refits the track and then tries to add hits from inner stereo superlayers. The second phase of

stereo reconstruction is “histogram linking”-based and is used to find the vertex of the track. The fourth and last step of COT tracking is a global refit of the track taking into account all known corrections for the non-uniformity of the magnetic field and for the modeling of the electron drift.

### Outside-In Algorithm

The Outside-In (OI) is the default CDF tracking algorithms. It is based on COT 96 sampling planes of wires arranged in 8 superlayers. Its short-come is the (limited) coverage, that extends with full sampling up to  $\eta = 1$ . The track found in the COT [65] is propagated inwards into the silicon system. A road around a track is defined using the uncertainties on track parameters and silicon hits are added if they lie inside this predefined road. When a hit is added, the track parameters are recalculated and the hit search is performed again. The accepted track has the largest number of hits. If more than one candidate has the same number of hits, the one with the lowest  $\chi^2$  is selected. The impact parameter resolution of COT + SVX tracks is found to be  $\sigma_{d_0} \simeq 20 \mu\text{m}$ .

### Silicon-Stand-Alone Algorithm

The hits in silicon subdetectors not used by OI tracking are available to the Silicon-Stand-Alone algorithm[66] that covers the region  $|\eta| < 2$  with some residual efficiency up to  $|\eta| \simeq 2.8$ . The SiSA algorithm starts from a collection of at least four hits in the SVXII detector in the  $r - \varphi$  plane and fits the  $C$ ,  $D_0$  and  $\lambda$  parameters (appendix F) to obtain a projection of the helix on the transverse plane. Then the algorithm creates a 3-D seed track adding small angle hits and the primary vertex information. At this point the  $90^\circ$  stereo hits are added and a global refit is performed. SiSA tracks reconstructed only with SVXII have a poor resolution for high  $p_T$  tracks so hits are searched in L $\emptyset\emptyset$  and ISL with the SVXII track as seed. The track is refit if other layers can be added. However, the performances on momentum and impact parameter resolution are limited. SiSA tracks are not used for secondary vertexing.

### Inside-Out Algorithm

The Inside-Out tracking algorithm[67], tries to recover efficiency and  $p_T$  resolution in the region  $1.2 < |\eta| < 1.8$  where the COT coverage is limited. SiSA tracks are

used as seeds which are extrapolated to the COT inner cylinder. Matching hits in the COT are added, track is refitted and all duplicates are removed.

### “Phoenix” Forward Electron Tracking

The Phoenix tracking algorithm [68] combines calorimetric information and standalone silicon tracks to track electrons in the forward region. The position of the EM shower in PES and the primary event vertex are used as seed points of the track helix and the helix curvature is varied to match the calorimeter  $E_T$ . If such a match is found, the track is called *Phoenix* electron (PHX).

### Vertex Finding Algorithm

The position of the interaction point, the so-called “primary vertex” of the event, is reconstructed by two algorithms: *PrimVtx* and *ZVertex*.

The seed used by *PrimVtx* is the average event  $z$  position measured during collisions. All tracks with  $|z_{trk} - z_{vtx}| < 1$  cm,  $|d_0| < 1$  cm and  $|d_0/\sigma_{d_0}| < 3$  are selected, ordered in decreasing  $P_T$  and fitted to a common vertex. The tracks with  $\chi^2 > 10$  after the fit are removed and the procedure is iterated until all accepted tracks have  $\chi^2 < 10$ .

*ZVertex* selects vertices from tracks passing minimal quality requirements and removes those without a minimum associated number of tracks with  $P_T > 300 MeV$ <sup>1</sup>. The  $z$  position of each vertex is the mean  $z_0$  of its associated tracks, weighted on the respective uncertainty  $\sigma_{z_0}$ .

## 3.2 Calorimeter Electron and Photon Identification

The calorimeter plays a fundamental role in particle detection. The first hint of an outgoing electron is a energy deposit (“cluster”) in the EM section of the calorimeters.

The CDF EM clustering algorithm[69] works in a simple but efficient way. The physical space corresponding to the calorimeter towers is mapped in the  $\eta - \varphi$  plane. The algorithm creates two lists of towers ordered by decreasing observed energy: the “usable list” (towers with energy  $> 100$  MeV) and the “seed list” (towers with

---

<sup>1</sup>A track is associated to a vertex if its distance from the vertex is less than 1 cm (silicon vertex) or 5 cm (COT vertex).

energy  $> 2$  GeV). It then takes the first seed tower and creates an  $\eta - \varphi$  cluster by adding the neighboring towers to form a 2x2 or 3x3  $\eta - \varphi$  area.

An EM cluster is found if  $E^{Had}/E^{EM} < 0.125$ , where  $E^{Had}$  is the energy deposited in the backing hadronic calorimeter towers and  $E^{EM}$  is the corresponding quantity for the EM section. As final step the  $\eta - \varphi$  centroid of the cluster is calculated and the used towers are removed from the lists. The algorithm selects the next seed tower and iterates the process until all seed towers have been used.

Usually the 3x3 clustering is used in the CEM region while 2x2 clusters are used in the PEM region, in order to properly reduce the probability to overlap the clusters of two different electrons. A cluster is not allowed to cross the boundary between different subdetectors. Several corrections are applied to reconstruct the initial energy of the EM object. Clusters are corrected for lateral leakage, off-center location inside the physical tower, on-line calibration and response curve drawn by the test beam data. The energies measured in the shower max (PES) and pre-shower (PPR) detectors are added to the reconstructed energy. PES is also used to compare the shower profile of electrons or photons to the profile measured in an electron test beam, and to measure the position of the EM shower centroid.

Beyond the raw EM energy measurement, the calorimeter information can be further exploited for a better particle identification. The  $E^{Had}/E^{EM}$  ratio is used to identify electrons. Studies performed with certified  $Z^0 \rightarrow e^+e^-$  events[70] show that electrons detected in the central or in the plug region have a little deposit in the hadronic part of the calorimeter (Fig. 3.2).

The *IsoRel* (or isolation) is another quantity derived from calorimeters. It is defined as:

$$- IsoRel \equiv E_T^{iso}/E_T^{cluster} < 0.1,$$

where  $E_T^{iso} = E_T^{0.4} - E_T^{cluster}$  and  $E_T^{0.4}$  is the energy collected by the calorimeters within a radius  $\Delta R = 0.4$  from the centroid of the EM cluster. Isolation is used in analysis involving a  $W^\pm$  or  $Z^0$  boson since leptons coming from the bosons decay are usually far from jets or other particles.

If a track is matched to the EM cluster, also the  $E^{cluster}/p^{trk}$  ratio can be used for a better electron identification. The  $E/p$  distribution is peaked at 1 but it has a large tail above 1 because electrons can radiate collinear photons in the passage through matter in the tracking volume. The EM energy measurement is weakly influenced by that (the photon usually deposits energy in the same EM cluster),

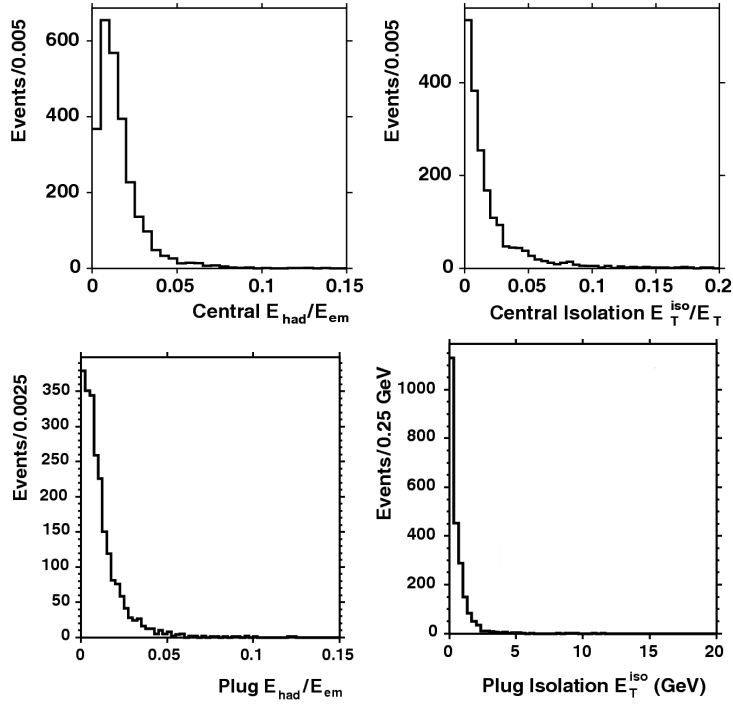


Figure 3.2:  $E^{Had}/E^{EM}$  (left) and isolation (right) distribution of central (top) and plug (bottom) calorimeter electron selection from unbiased, second leg of  $Z^0 \rightarrow e^+e^-$  candidate events in data[70].

but the momentum measurement decreases. Also photons are identified from their showers in the EM calorimeters. The discrimination between electrons and photons is obtained by requiring a reconstructed track pointing to the energy cluster in the EM calorimeter for the electrons and no tracks for photons. Within a cone with radius  $R = 0.4$  centered on the EM cluster, as wide as the typical hadron jets, the “no track” requirement for photons is as follows:

- the difference between the EM signal  $E_{EM}$  and the sum  $\sum_i E_i$  over all calorimeter towers within the cone must be less than  $0.15 \cdot E_{EM}$ ;
- the sum  $\sum_j P_{T_j}$  over all tracks within the cone must be less than 2 GeV.

Photons can be faked by electrons when the electron track fails to be reconstructed. Electrons can be faked by charged hadrons showering in the EM calorimeters or in the solenoid, or by conversion electron pairs ( $\gamma\gamma^* \rightarrow e^+e^-$ , being  $\gamma^*$  an atomic or molecular field) when also a track happens to point to the photon EM cluster. Electrons from photon conversion are identified and rejected if two opposite-

sign COT tracks are close in space showing  $|\Delta(\cot\theta_0)| < 0.04$  and  $|\Delta(xy)| < 2mm^2$ .

### 3.3 Muon Identification

Muons are as important as electrons in our search since the  $W \rightarrow \mu\nu$  decay is as frequent as  $W \rightarrow e\nu$ . Their identification is necessary and the corresponding background must be rejected.

High energy muons cross the calorimetric system as minimum ionizing particles (MIP). They are identified by a track inside COT, a deposit of a MIP inside EM and HAD calorimeters and an aligned track segment (“stub”) in the outer muon chambers. Muons can be faked by cosmic rays, by  $\pi$ ,  $k$  forward leptonic decays in the tracker and by hadrons not showering inside the calorimeters (“punch-through”). A number of software filters are used to reject the cosmics, and computed corrections are applied to the raw muon flux to account for hadronic decay and punch-through.

### 3.4 Neutrino Identification

Momentum conservation is the only way to reveal the presence of neutrinos since they do not interact in the detector components. While it is impossible to know the exact momentum of the colliding partons, the transverse component of the parton pair,  $p_T$ , should be approximately zero in the detector frame. All the detected transverse energy in the event is vectorially added, and if the sum is significantly different from zero, we assume a candidate neutrino is revealed. The missing transverse energy  $\vec{E}_T$  gives a measurement of the neutrino transverse momentum<sup>3</sup>. It is defined as:

$$\vec{E}_T \equiv - \sum_i \vec{E}_T^i \quad (3.1)$$

where  $\vec{E}_T^i$  is a vector with magnitude equal to the transverse energy collected by the  $i$ -th calorimeter tower and pointing from the interaction vertex to the center of the tower. The sum involves all towers with total energy above 0.1 GeV in the region  $|\eta| < 3.6$ . At offline level, the algorithm corrects for the position of the reconstructed event vertex and for any reconstructed muon in the tracker.

---

<sup>2</sup> $\Delta(xy)$  is the distance between the two tracks on the  $x \times y$  plane.

<sup>3</sup>For a massless neutrino  $p_T = E_T$ .

### 3.5 Jet Identification

According to QCD, partons composing the (anti)proton can be treated perturbatively as free particles if they are struck by an external probe<sup>4</sup> with sufficiently large momentum transfer (“hard scattering”). Scattered partons convert into color-less hadrons when entering the physical world. This process is called parton “hadronization” or parton “showering” and produces a collimated cluster of stable particles named “jet”. A jet approximately retains the total momentum and direction of the initial parton (for a pictorial representation see Fig. 3.3). Because of the intrigued

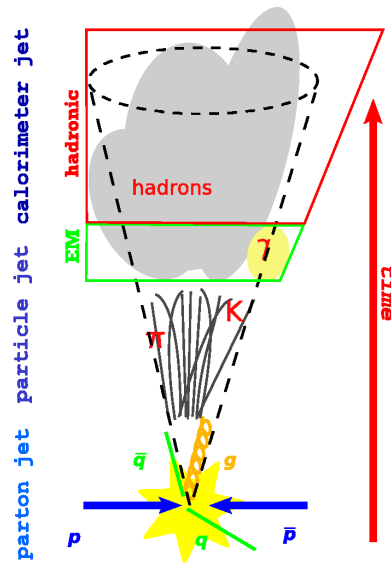


Figure 3.3: A parton originating from a hard scattering hadronizes and generates a collimated spray of particles, a jet.

multi-step relationship relating jets to primary partons one must be careful in their treatment and definition since any inappropriate handling would cause a systematic error or worsen the resolution in the parton momentum measurement. For example, a poor jet energy resolution would reduce the sensitivity in the search for a SM light Higgs Boson  $H \rightarrow b\bar{b}$ . A wrong jet energy scale can introduce a bias in delicate measurements, like in measuring the top quark mass.

From an experimenter’s point of view a jet is defined as a large energy deposit in a localized area of the detector<sup>5</sup> (see Fig. 3.4). The challenge of a physics analysis is to recover from detector information the initial energy, momentum and, possibly,

<sup>4</sup>I.e. a lepton or a parton belonging to another hadron.

<sup>5</sup>The ripartition of jet energy is typically  $\sim 60\%$  in EM and  $\sim 40\%$  in the hadronic calorimeter

the nature of the parton produced in the original interaction.

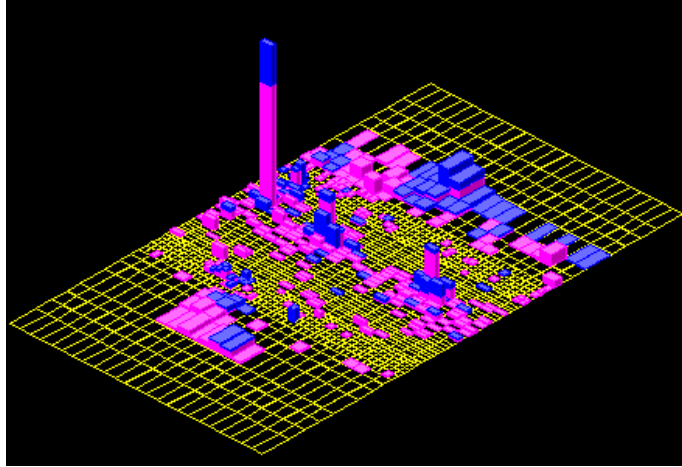


Figure 3.4: *Calorimetric deposit in the  $\eta - \varphi$  plane as represented in the CDF event display of a typical event. EM deposits are red while HAD deposits are blue. The height of the signals are proportional to the deposit energy.*

The information carried by the jet can be degraded for non-accounted physical reasons and for instrumental features of the detectors (fig. 3.3):

- the primary parton is the jet at the “parton level”: Whether the jet is generated by a quark or by a gluon is not known. However their radiation of secondary partons is somewhat different;
- the particles produced in the evolution of the jet correspond to the “particle (or hadron) level”: the details of particle production, the fragmentation process, are unknown;
- the calorimeter signal identifying the jet correspond to the “calorimeter level”: the calorimeter response to hadrons is only approximately known and the calorimeter signals are subject to measurement errors.

A universally valid way of defining a jet does not exist because there is no control on how the hadronization process takes place. The experimentalist’s task is to conceive an algorithm that allows a fairly accurate extrapolation of the parton properties from those of the calorimeter jet. In this section the first step of this backwards path from calorimeter level to the parton level, the jet reconstruction, is described as simulated at CDF [72, 73]. The parton reconstruction algorithm,

also called a “jet algorithm” or “transfer function”, is a tool to reconstruct such information and it must satisfy at best the following requirements[72]:

- *Infrared safety*: the presence of soft radiation between two jets may cause a merging of the two jets. This should be avoided at best by the algorithm in order to avoid an incorrect reconstruction of parton parameters.
- *Collinear safety*: the jet reconstruction should be insensitive to collinear radiation in the event, i.e. different energy distribution of particles inside calorimetric towers.
- *Invariance under boost*: the same jets should be found independently of boosts in longitudinal direction.
- *Boundary stability*: reconstructed kinematic variables should be insensitive to details of the final state.
- *Order independence*: the same kinematical variables should be traced all along the reconstruction path, at parton, particle and detector levels.
- *Straightforward implementation*: for practical reasons, the algorithm should be easy to implement in perturbative calculations.

Beyond these theoretical aspects, a jet algorithm should be experimentally valuable, with high reconstruction efficiency, good resolution and stable at different luminosity. For sake of completeness a list of this “experimental attributes” is given below:

- it should be able to reconstruct jets in detectors of different design;
- it should not degrade the instrumental resolution;
- its performances should be stable against multiple interactions in the same bunch crossing;
- it should be optimized in terms of computing time;
- it should identify all interesting jets;
- it should allow an easy calibration of the jet properties;
- it should be applicable in a wide range of jet multiplicity, space distribution and energy;
- it should be easily applicable.

### 3.5.1 CDF Cone Algorithm

CDF uses several jet reconstruction algorithms, none of them fully satisfying all the above requirements. The official jet algorithm at CDF is a cone clustering called JETCLU, an iterative fixed cone jet reconstruction algorithm based only on calorimetric information.

The algorithm begins by creating a list of the seed towers from all the calorimeter towers with transverse energy above the threshold of 1 GeV. Starting with the highest- $E_T$  seed tower, a precluster is formed by combining together all adjacent seed towers within a cone of given radius  $R^6$  in the  $\eta - \varphi$ . This procedure is repeated, starting with the next unused seed tower, until the list is exhausted. The  $E_T$ -weighted centroid is then formed from the towers in the precluster and a new cone of radius  $R$  is formed around this centroid. All towers with energy above the lower threshold of 100 MeV within this new cone are added to the cluster. Then, a new centroid is calculated from the set of towers within the cluster and a new cone drawn. This process is iterated until the new centroid does not drift appreciably away from the previous one (stable solution).

Since the clusters found initially can overlap, the next step is to decide whether to merge or rather separate overlapping clusters. Each tower should not be assigned to more than one jet. Two clusters are merged if the total energy of the overlapping towers is greater than 75% of the energy of the smallest cluster. If the shared energy is below this cut, the shared towers are assigned to the cluster that is closer in  $\eta - \varphi$  space. This process is iterated again until the list of clusters remains fixed.

Massless four-vector momenta are assigned to the towers in the clusters for EM and HAD components with a magnitude equal to the energy deposited in the tower and the direction defined by a unit vector pointing from the event vertex to the center of the calorimeter tower at shower maximum. A cluster four-vector is then

---

<sup>6</sup>CDF reconstructs jets using radii 0.4, 0.7 and 1.0.

defined summing over the towers in the cluster:

$$E = \sum_{i=1}^N (E_i^{EM} + E_i^{HAD}), \quad (3.2)$$

$$p_x = \sum_{i=1}^N (E_i^{EM} \sin \vartheta_i^{EM} + E_i^{HAD} \sin \vartheta_i^{HAD}) \cos \varphi_i, \quad (3.3)$$

$$p_y = \sum_{i=1}^N (E_i^{EM} \sin \vartheta_i^{EM} + E_i^{HAD} \sin \vartheta_i^{HAD}) \sin \varphi_i, \quad (3.4)$$

$$p_z = \sum_{i=1}^N (E_i^{EM} \cos \vartheta_i^{EM} + E_i^{HAD} \cos \vartheta_i^{HAD}). \quad (3.5)$$

where the index  $i$  runs over the towers in the cluster. Towers and jets are treated as massless particles. From their total four-momentum all relevant quantities for the analysis are computed:

$$P_T = \sqrt{p_x^2 + p_y^2}, \quad (3.6)$$

$$E_T = E \cdot \frac{P_T}{P}, \quad (3.7)$$

$$Y = \frac{1}{2} \cdot \ln \frac{E + P_z}{E - P_z}. \quad (3.8)$$

Other useful informations like the number of tracks reconstructed inside the jet cone, the vertex quality or the energy deposited in the HAD and EM calorimeter are added to the final jet-object used in the analysis.

### 3.6 Jet Corrections

The ultimate goal of the jet reconstruction algorithm is the determination of the energy of the outgoing partons coming from the hard interaction. As discussed above the information obtained by jet reconstruction can be incomplete or degraded by different phenomena and experimental features<sup>7</sup> :

- event dependent degradation
  - jet overlap;
  - pile-up from multiple interaction;

---

<sup>7</sup>Because of these effects the jet energy as obtained from direct calorimeter measurements is often referred as “raw” jet energy.

- background from spectator partons (“underlying event” – UE);
- detector depending degradation
  - incomplete hermeticity of the calorimeter;
  - non uniform or time-dependent detector response;
  - finite detector resolution;
  - biased clustering algorithm;
  - electronics dead time.

In order to overcome these limitations and allow extrapolating the jet parameters to the parton level, CDF developed a set of generic<sup>8</sup> jet energy corrections depending of  $\eta$ ,  $E_T^{raw}$  and  $R$  of the jet reconstructed by JETCLU algorithm.

### 3.6.1 Corrections to the Raw Measured Jet Energy

The corrections are divided into five levels<sup>9</sup> (“ $L$ -levels”) so that can be applied in a standard way to different analyses[74, 75]:  $\eta$ -dependent response ( $L1$ ), effect of multiple interactions ( $L4$ ), absolute energy scale ( $L5$ ), underlying event ( $L6$ ) and out-of-cone ( $L7$ ) corrections. In this analysis jets are corrected up to Level-7. The correction  $L1$  and  $L5$  are multiplicative factors ( $f_{L1}$  and  $f_{L5}$ ) on the raw  $E_T$  of the jet, the others are additive constants ( $A_{L4}$ ,  $A_{L6}$  and  $A_{L7}$ ). The general equation to apply all corrections is:

$$E_T^{corr}(\eta, E_T^{raw}, R) = (E_T^{raw} f_{L1} - A_{L4}) f_{L5} - A_{L6} + A_{L7}. \quad (3.9)$$

#### Level-1: $\eta$ dependent corrections

$L1$  correction is applied to raw jet energy measured in the calorimeters to make the detector response uniform in  $\eta$ . It takes into account aging of the subdetectors<sup>10</sup> and other “hardware” non-uniformities (for example the presence of cracks). This correction is obtained using a large di-jet sample: events with one jet (*trigger jet*) in the central region of the calorimeter ( $0.2 < |\eta| < 0.6$ ), where the detector response is well known and flat in  $\eta$ , and only one second jet (*probe jet*), allowed to range

<sup>8</sup>The word “generic” means that the jet corrections do not take into account the process or the parton from which the jet was generated.

<sup>9</sup>The actual naming skips a Run I step named  $L2$ , because it is absorbed in  $L1$ , and  $L3$ , as it was introduced as a temporary MC calibration in Run II.

<sup>10</sup>This was the  $L2$  correction during Run I

anywhere in the calorimeter ( $|\eta| < 3.6$ ). Since in a perfect detector the two jets should be balanced in  $p_T$ , a balancing fraction is formed:

$$f_b \equiv \frac{\Delta p_T}{p_T^{ave}} = \frac{p_T^{probe} - p_T^{trigger}}{(p_T^{probe} + p_T^{trigger})/2}, \quad (3.10)$$

the average of  $f_b$  in the analyzed  $\eta$  bin is used to define the  $\beta$  factor<sup>11</sup> (Fig. 3.5 shows the  $\beta$  distribution for different cone radii):

$$\beta \equiv \frac{2 + \langle f_b \rangle}{2 - \langle f_b \rangle}. \quad (3.11)$$

The final  $L1$  correction is defined as  $f_{L1}(\eta, E_T^{raw}, R) = 1/\beta$  and reproduces an approximately flat response in  $\eta$  with an error varying from 0.5% to 7.5%.

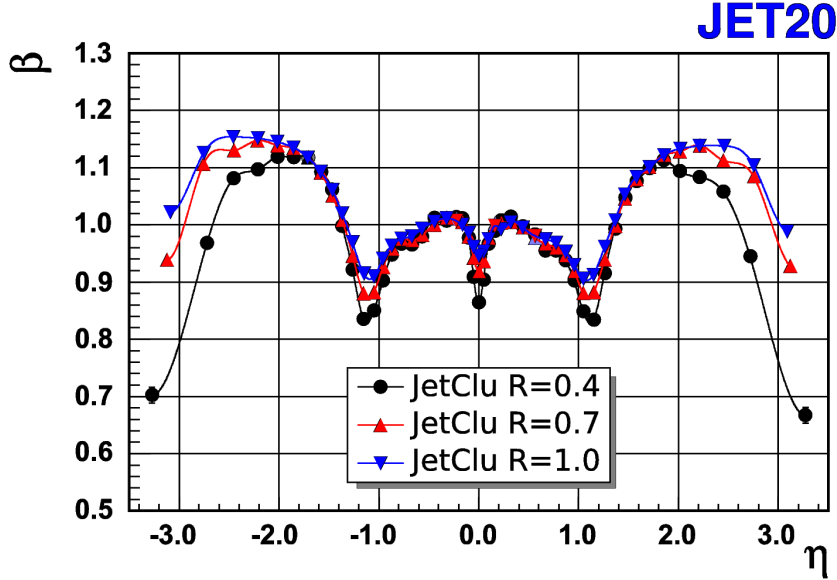


Figure 3.5:  $\eta$ -dependence of  $\beta$  factors for cone radii  $R = 0.4, 0.7$  and  $1.0$ , measured in the di-jet component of jet20 sample.

#### Level-4: multiple interactions corrections

Jet energy measurement is also degraded by the presence of minimum-bias events that come from multiple  $p\bar{p}$  interactions within the same bunch crossing. This correction becomes more relevant at high luminosity. The number of  $p\bar{p}$  interactions

<sup>11</sup>The definition of Eq. 3.11 has the correct average value equal to  $p_T^{probe}/p_T^{trig}$  but is less sensitive to presence of non-Gaussian tails in the usual  $p_T^{probe}/p_T^{trig}$  ratio.

is Poisson distributed with mean value depending almost linearly on instantaneous luminosity:

$$\langle N(\mathcal{L} \simeq 10^{32} \text{ cm}^{-2}\text{s}^{-1}) \rangle \simeq 3, \quad \langle N(\mathcal{L} \simeq 3 \cdot 10^{32} \text{ cm}^{-2}\text{s}^{-1}) \rangle \simeq 8. \quad (3.12)$$

The energy of particles coming from those processes is estimated from minimum-bias events drawing a cone in a random position in the region  $0.1 < \eta < 0.7$ . Figure 3.6 shows that the measured minimum-bias  $E_T$  grows linearly with the number of primary vertices<sup>12</sup>.  $A_{L4}$ , must be subtracted from the raw jet energy. This correction is R-dependent and its total uncertainty is  $\sim 15\%$ , depending on  $\mathcal{L}$ , event topology, vertex reconstruction efficiency and fake rates.

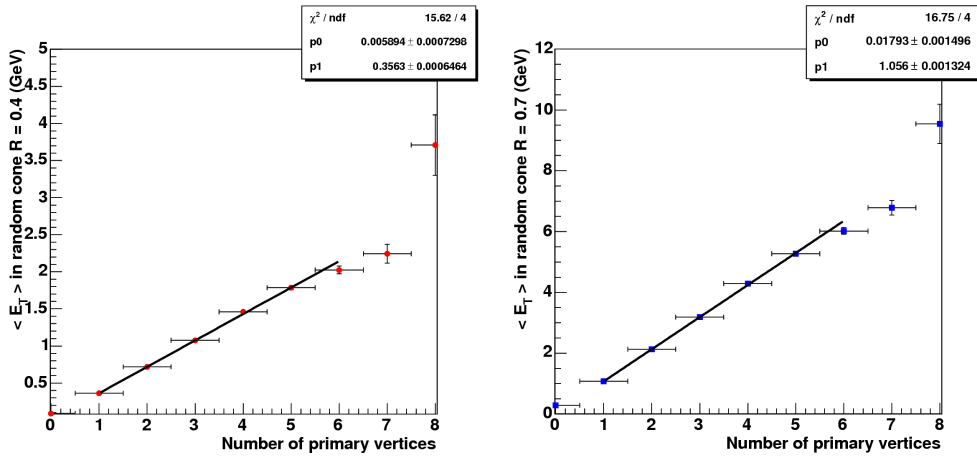


Figure 3.6: Multiple interaction  $E_T$  correction as a function of primary vertex number for cones with  $R = 0.4$  (left) and  $R = 0.7$  (right).

### Level-5: absolute energy scale corrections

While  $L1$  and  $L4$  make jet reconstruction uniform over the whole detector and over the changing rate of  $p\bar{p}$  interactions,  $L5$  corrections ( $f_{L5}$ ) step from calorimeter level back to particle level.

The study is MC driven. Jet events are generated with full CDF detector simulation, then jets are reconstructed both at calorimeter and hadron generation levels (HEPG) using the same clustering algorithm. A calorimeter jet (C) is associated to the corresponding hadron jet (H) if  $\Delta R < 0.1$ . For both HEPG and detector

<sup>12</sup>Good quality primary vertices are reconstructed through at least 2 COT tracks.

jets the transverse momentum,  $p_T^C$  and  $p_T^H$ , is calculated. The absolute jet energy is defined as  $\mathcal{P}(p_T^C|p_T^H)$ , the probability to measure  $p_T^C$  with a given  $p_T^H$ <sup>13</sup>.

Figure 3.7 shows the correction factor  $f_{L5}$  for different cone sizes as function of the different jet transverse energies. The total uncertainty is about 3% and it mainly arises from the determination of calorimetric response to single particles and MC fragmentation modeling.

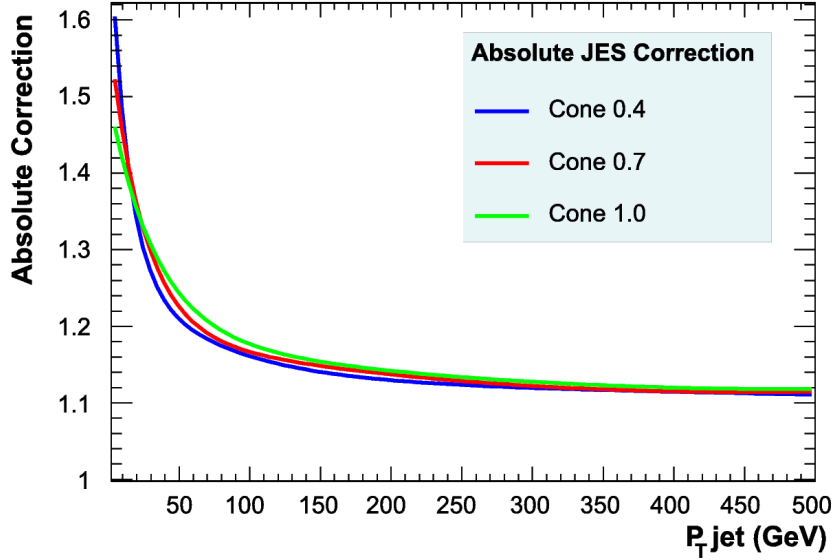


Figure 3.7: Absolute jet energy scale correction ( $f_{L5}$ ) for different cone sizes.

### Level-6 & Level-7: underlying event and out-of-cone corrections

The underlying event correction ( $L6$ ) takes into account the interaction processes which can occur between spectator partons or that originates from initial state radiation (usually soft gluon radiation) while the out-of-cone correction ( $L7$ ) considers the fraction of particles coming from the original parton that fall outside the jet cone.

The underlying event energy ( $A_{L6}$ ) must be subtracted from the total jet energy. It was measured studying minimum-bias events during Run I and is parametrized with a value that scales with the cone radius. Out of cone energy ( $A_{L7}$ ) must be added to the total jet energy. Studies to determine the cone-size dependent value of this correction are carried out with the same jet-to-parton matching method of

<sup>13</sup>If more than one  $p_T^H$  give the same  $p_T^C$  the largest of the two is chosen

L5.

### 3.6.2 Corrections to the Raw Measured Missing $E_T$

The raw missing  $E_T$  for any event is defined as a vector in the  $x \otimes y$  plane, according to (eq. (3.1)) and must be corrected for the presence of muons and for errors in the raw energy measured by the calorimeter. The correction for muons is performed in two steps:

- the muon track is extrapolated to the calorimeters and an energy corresponding to a MIP ( $\sim 350$  MeV in CEM and  $\sim 1.6$  GeV in CHA) is removed from the crossed towers and from the total  $P_T$  balance;
- the muon  $P_T$  is included in the total  $P_T$  balance.

Equation (3.1) is then changed into eq. (3.13) in the presence of a muon:

$$\cancel{E}_T = - \sum_i E_i \cdot \sin \vartheta_i \cdot \hat{n}_i + E_{T_{MIP}} \cdot \hat{n}_\mu - P_{T_\mu}. \quad (3.13)$$

The  $\cancel{E}_T$  must take into account the level of jet energy corrections too. The procedure is analogous to the correction for muons:

- the contribution given by the raw measured energy of the identified jets is removed from the total  $P_T$  balance;
- each jet is corrected at the level used in the analysis and the  $P_T$  of all jets, corrected at the desired level, is put back in the total  $P_T$  balance.

In order to avoid underestimating the total activity in the calorimeters because of the minimum bias energy subtraction in jet corrections, the jets are corrected in this case excluding L4 correction if the applied level is superior<sup>14</sup>. The final expression for the corrected  $\cancel{E}_T$ , for a level  $n$  of jet energy corrections, is then<sup>15</sup>:

$$\cancel{E}_T^{@Ln} = - \sum_i E_i \cdot \sin \vartheta_i \cdot \hat{n}_i + E_{T_{MIP}} \cdot \hat{n}_\mu - P_{T_\mu} + \sum_j P_{T_j}^{RAW} - \sum_j P_{T_j}^{(@Ln-L4)}. \quad (3.14)$$

<sup>14</sup>This is what is meant by the superscript  $(@Ln-L4)$  in eq. (3.14). It is assumed that the energy due to MB events be randomly distributed in  $\varphi$ .

<sup>15</sup>The index  $j$  runs on all the identified and reclustered jets.

### 3.7 Secondary Vertex Tagging

The identification of heavy flavor jets (i.e jets containing a bottom or charm hadron) is of fundamental importance in many analyses. Both quark top and the SM Higgs boson have large branching fraction into  $b$ -quark, and the exclusive identification of  $b$ -hadrons is a methodology to reduce background because many uninteresting physical processes contain only light flavor hadrons in the final state. An algorithm able to select a jet coming from a  $b$ -hadron is called “ $b$ -tagger” or “heavy flavor tagger”.

The Secondary Vertex Tagger algorithm (**SecVtx**) is one of the main  $b$ -taggers used at CDF<sup>16</sup>. It takes advantage of the long life time of  $b$ -hadrons: a natural  $c\tau$  value of about 450  $\mu\text{m}$  together with a relativistic boost due to a momentum of several GeV permit to a  $b$ -hadron to fly several millimeters<sup>17</sup> away from the primary interaction vertex. The relevant quantity is the relativistic boosted  $c\tau$  which determines the average impact parameter of the outgoing debris of  $b$ -hadron decays. The decay produces small sub-jets composed by tracks with large impact parameter ( $d_0$ ). The silicon detectors (see section 2.4.2) are able to reconstruct  $d_0$  with errors of the order  $\approx 50\mu\text{m}$ <sup>18</sup>, fully adequate to separate displaced tracks from prompt tracks coming from the primary interaction. Figure 3.8 shows as a  $W$ +jets candidate event with two displaced secondary vertices is identified by **SecVtx** and reconstructed by the CDF event display.

The variety of  $b$ -hadrons decay channels makes it very difficult for a single algorithm to achieve optimal efficiency. For example **SecVtx** has low efficiency in detecting semileptonic decays, or decays with low charged tracks multiplicity. Moreover the presence of  $D$  (charm) hadrons that may produce tertiary vertices may make the kinematic of a  $b$ -hadron decay even more complex.

To improve  $b$ -tagging efficiency, and to add tools to its searches, CDF developed other tagger algorithms:

- the “soft-lepton-tagger” algorithm which looks for semileptonic heavy flavor decays (its main difficulty is the identification of low energy leptons inside high density jets);

<sup>16</sup>Historically it was the most important component in top discovery in 1995.

<sup>17</sup>The average transverse momentum of a  $b$ -hadron coming from a  $WH$  events is about 40 GeV/ $c$  for a Higgs boson mass of 115 GeV/ $c^2$ ; in that condition a neutral  $B^0$  meson of mass 5.28 GeV/ $c^2$  undergoes a boost  $\beta\gamma = 7.6$  and the average decay length is 3.5 mm.

<sup>18</sup>Including the transverse size of the beam-beam interaction region

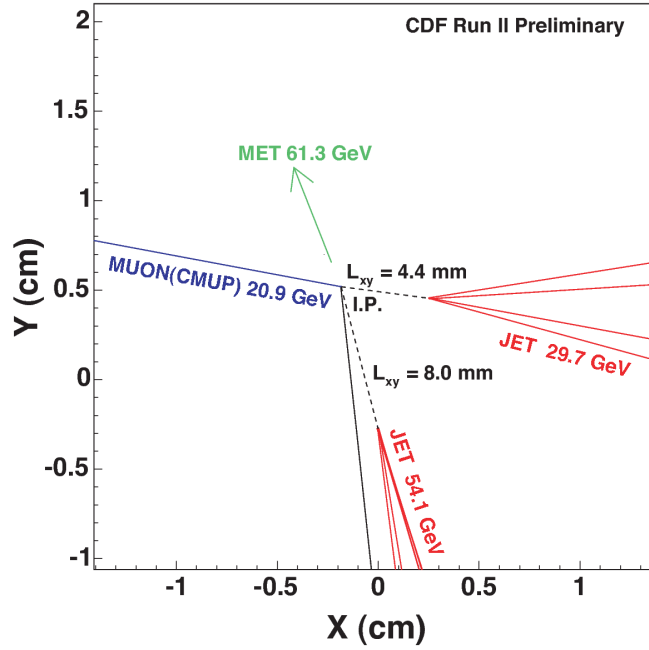


Figure 3.8:  $W$ +jets candidate event with two secondary vertices tagged by SecVtx (run 166063, event 279746). The  $\cancel{E}_T$  direction, a muon track, a prompt track and tracks from the secondary vertices are shown.

- the “jet-probability” algorithm assigns to each track the probability to come from the primary interaction vertex. A scalar probability parameter for the entire event can be built by adding the information from all tracks. Heavy flavour jets can be separated from background jets by setting a suitable threshold on the parameter.

SecVtx tries to merge large impact parameter ( $d_0$ ) tracks into a common vertex. The study is performed for all jets with  $|\eta| < 2.4$  in a event. For each jet only the tracks within the jet cone (i.e.  $\Delta R_{jet, trk} < R_{jet}$ ) are examined. The standard SecVtx mode of operating (“Tight SecVtx”) is described below. Two additional modes (called “Loose” and “Ultratight”) differ mostly in the applied thresholds. In the default SecVtx the “usable” tracks must satisfy the following requirements:

- $p_t > 0.5 \text{ GeV}/c$ ,
- $|d_0| < 0.15 \text{ cm}$  and  $|d_0/\sigma_0| > 2.0$ ,
- $|z_0 - z_{prmVtx}| < 2.0 \text{ cm}$ ,

- have a minimum number of hits in the silicon detector, the number depending on track reconstruction quality and position,
- be seeded or confirmed in the COT.

A “taggable” jet is defined as a jet containing at least two such tracks.

The algorithm works in two steps:

- In *Pass 1* at least three tracks are required to pass loose selection criteria, i.e the general ones for usable **SecVtx** tracks, but at least one of the tracks is required to have  $p_T > 1.0$  GeV/ $c$ . The selected tracks are combined two by two until a seed secondary vertex is built. The additional usable tracks are added one by one and a quality  $\chi^2$  is computed. Finally tracks are added or removed depending of their contribute to the  $\chi^2$ .
- *Pass 2* begins if *Pass 1* gives a negative result. Now only two tracks are required to form a secondary vertex but they must pass tighter requirements:  $p_t > 1.0$  GeV/ $c$ ,  $|d_0/\sigma_0| > 3.5$  and one of the tracks must have  $p_T > 1.5$  GeV/ $c$ .

If a secondary vertex is identified in a jet, the jet is “tagged”. The two dimensional decay length  $L_{xy}$  is calculated as the projection into the jet axis, in the  $r - \varphi$  plane, of the vector pointing from the primary vertex to the secondary one. The sign of  $L_{xy}$  is defined by the angle  $\alpha$  between the jet axis and the **SecVtx** vector. Figure 3.9 explains the geometry.

A secondary vertex coming from a heavy flavor hadron is expected to have large  $L_{xy}$ . To reduce background due to mismeasured tracks  $|L_{xy}/\sigma_{L_{xy}}| > 7.5$  is required. Other cuts are made on the invariant mass of the pair of tracks, to avoid  $K$  and  $\Lambda$  decays, and on vertex multiplicity and impact parameter to reject secondary vertices due to interaction with material inside the tracking volume.

### 3.7.1 Tagging Performances and Scale Factors

The performances of a  $b$ -tagger are evaluated by its efficiency, i.e the relative rate of correctly identified  $b$ -hadrons and by its purity, i.e the rate of falsely identified  $b$ -hadrons in a sample with no true  $b$ -hadrons. CDF uses  $t\bar{t}$  MC to evaluate **SecVtx** efficiency relying on detector and physical processes simulation. Figure 3.10 shows the  $b$ -tagging efficiency as a function of jet  $\eta$  and  $E_T$  for the three **SecVtx** modes.

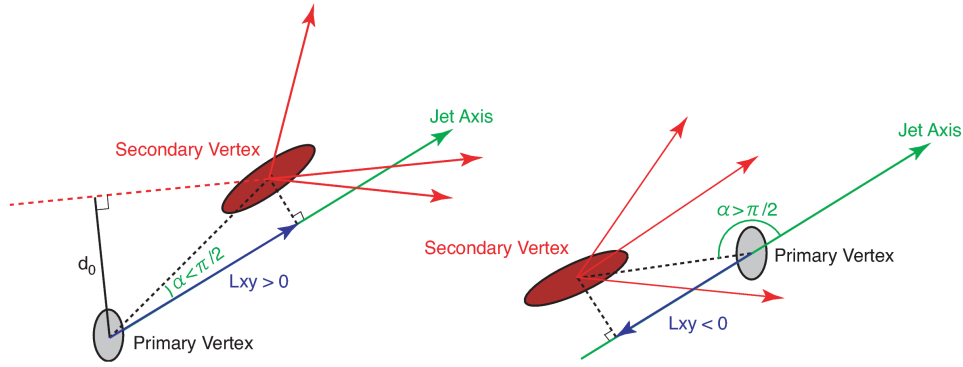


Figure 3.9: SecVtx variables. Left: true reconstructed secondary vertex. Right: negative SecVtx tag (falsely reconstructed secondary vertex). Negative  $L_{xy}$  has no physical meaning but it is important for estimating the mistag probability due to resolution effects.

The tagging efficiency at large  $\eta$  and at large  $E_T$  drops essentially because of lower track detection efficiency and resolution.

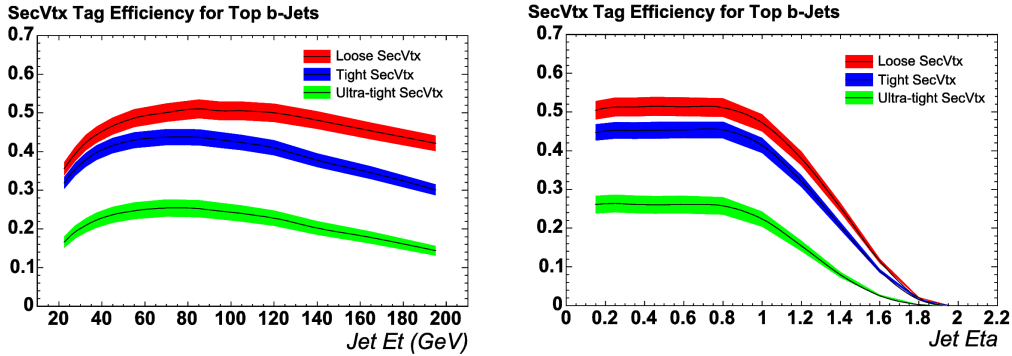


Figure 3.10: Efficiency to tag jets in top quark Monte Carlo samples which have been matched to  $b$  quarks, using the “tight”, “loose” and “ultra-tight” tunes of the SecVtx tagger in function of jet  $E_T$  (left) and  $|\eta|$  (right). The efficiency is obtained by multiplying the tag rate in the Monte Carlo by the measured data/MC scale factors of tab. 3.1. The bands represent the systematic error on the data/MC scale factors. The decrease in efficiency at high jet  $E_T$  is due to declining yield of good silicon tracks passing the quality cuts. The decrease at large  $\eta$  (right plot) is due to the reduced tracker coverage.

As MC does not reproduce the exact  $b$ -tagging efficiency of SecVtx as found

mode	$\Phi$	$\sigma_\Phi$ (stat)	$\sigma_\Phi$ (syst)
Loose	0.95	0.01	0.05
Tight	0.95	0.01	0.04
Ultra-tight	0.88	0.01	0.05

Table 3.1: **SecVtx** Scale factors ( $\Phi$ ) for the three different **SecVtx** operating modes.

in certified b-jets in data, a “scale factor” (SF or  $\Phi$ ) is introduced to account for data/MC difference in the form:

$$\Phi \equiv \frac{\varepsilon_{data}}{\varepsilon_{MC}}. \quad (3.15)$$

CDF uses two methods to calculate SF: the first looks in the inclusive jet sample for jet pairs with certified heavy flavor pair production: for example an event can contain two back-to-back jets, one of which is matched to a high  $p_T$  muon and the other one is  $b$ -tagged by **SecVtx**. We can infer that the jet matched to the muon originates from a  $b$ -hadron semileptonic decay and can apply **SecVtx** to it. A correction to allow for the small difference in **SecVtx** tagging efficiency for inclusive  $b$ -hadron decays is computed with MC, and it is possible to compare  $b$ -tagging efficiency on real data and derive the SF. The second method exploits electrons instead of muons. Figure 3.11 shows the SF determination with the two methods, Table 3.1 reports the SF for the three **SecVtx** operation modes.

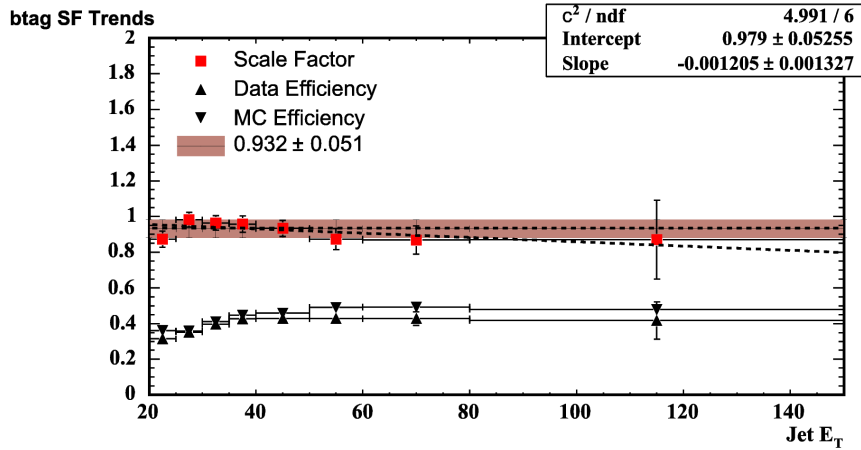


Figure 3.11: Scale Factor calculated with muon and electron  $b$ -tagging

The number of falsely **SecVtx** tagged jets is dubbed *mistags*. Mistags can be due

to finite track resolution, long living light-flavor hadrons or secondary interactions with detector material. They are measured in an inclusive jet sample (corrected to represent a sample with no heavy flavor components) and the reconstruction parametrizes mistags assigning a *mistag probability* depending on  $E_T$ ,  $\eta$ ,  $\varphi$  and track multiplicity of the considered jet. Figure 3.12 shows the mistag rate as function of  $E_T$  and  $\eta$  for a jet sample and two different **SecVtx** operating modes.

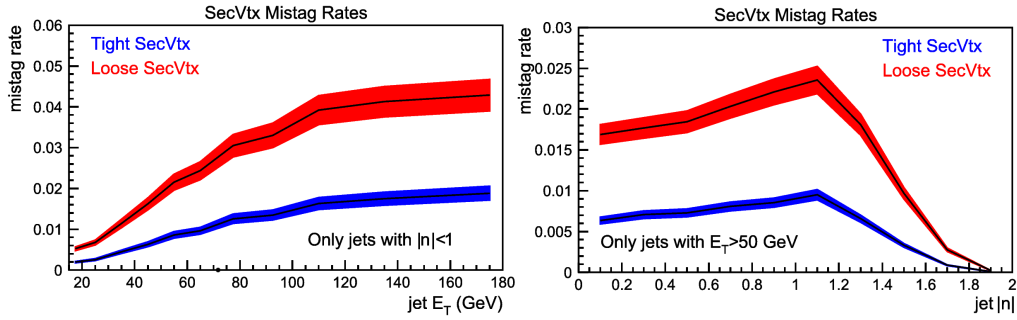


Figure 3.12: *Rate of wrongly SecVtx tagged jets (mistags) as a function of  $E_T$  and  $\eta$  for tight and loose SecVtx operation mode. The rate is derived from an inclusive jet sample corrected to remove the small contribution by real  $b$ -jets.*



# Chapter 4

## Event Selection

*We describe here the analysis cuts selecting the Monte Carlo sample on which the studies for an improved dijet mass resolution have been performed, as well as the data sample to be eventually analysed.*

Although our final goal will be to observe the associated WZ production in the “golden” channel for the light SM Higgs boson search ( $WH \rightarrow Wb\bar{b}$ ), as a first step we didn’t consider b-tagging. This was done in order to increase the available statistics for the dijet resolution studies. Given the small W, Z mass difference relative to the dijet mass resolution, we also considered the combined WW, WZ final states in which one W or the Z in the final state decay into two jets. The selected events must be consistent with a W leptonic decay. Therefore the basic signatures are:

- a lepton  $l$  (electron or muon) in the final state;
- $\cancel{E}_T$  consistent with leptonically decaying W boson;
- two jets to be consistent with the second boson decaying in a quark pair;

A detailed description of signal and background cross sections are in appendix G

### 4.1 Data Trigger Streams

We considered a suitable sample of real data to be compared with the simulation in order to define optimal candidate selection cuts. The data trigger paths requires

simply a high  $P_T$  lepton. The run ranges corresponding to the different data acquisition periods are listed in tab. 4.1. This list includes only runs corresponding to an optimal detector status.

Period	runs	dates
0d	138425-186598	04 Feb 02 - 22 Aug 04
0h	190697-203799	07 Dec 04 - 04 Sep 05
0i/0j	203819-233111	05 Sep 05 - 30 Jan 07
0j	233133-246231	30 Jan 07 - 04 Aug 07
0k	252836-261005	28 Oct 07 - 16 Apr 08
0m	261119-277511	18 Apr 08 - 13 Jun 09

Table 4.1: *Stored data runs used in this analysis*

#### 4.1.1 Physical Objects

The selected data events must be characterized by the following reconstructed objects<sup>1</sup>:

- one tight and isolated lepton (a tight lepton must have  $E_T \geq 20$  GeV and the  $z_0$  of its track must be  $< 60$  cm);
- the trigger lepton can be an electron (either CEM plus COT track or PEM plus PHX track) or a muon (either CMUP, i.e. CMU plus CMP stubs, CMX or BMU muons associated to COT tracks);
- two *JetClu* jets with  $R = 0.4$ , with energies  $E_T > 25$  GeV and  $E_T > 15$  respectively for the first and second leading jet<sup>2</sup> and  $|\eta_{det}| < 2$  ;
- $\cancel{E}_T > 20$  GeV.
- $m_T > 30\text{GeV}/c^{23}$  .

In addition, the selected events must pass certain vetoes to reject specific class of events not interesting for this work and to account for energy fluctuations in reconstructed objects:

<sup>1</sup>Jet energies and  $\cancel{E}_T$  are corrected at L7 of generic jet corrections before applying any cut

<sup>2</sup>Jets are ordered in decreasing  $E_T$

<sup>3</sup> $m_T$  is defined in the specific case of W(Z) boson decaying leptonically:

$$m_T = \sqrt{(E_T^l + E_T^\nu)^2 - (\vec{P}_T^l + \vec{P}_T^\nu)^2}$$

- $\cancel{E}_T$  significance<sup>4</sup>  $> 3.5$ ;
- The azimuthal distance between  $\cancel{E}_T$  and any clustered jet has to be  $> 0.3$  radians.
- Track  $\chi^2$  probability<sup>5</sup>:  $\chi^2 > 10^{-8}$ ;
- *Lepton conversion*: photon conversion resulting in lepton candidates are rejected by identifying an oppositely charged track satisfying a conversion configuration.
- $jet1llr \cdot jet2llr$ <sup>6</sup>  $> 1.05$

All these cuts are chosen looking at the agreement between data and Montecarlo distributions. In fig. 4.1 are shown the plots used to validate the cuts. The choice of a hard energy cut is motivated by the need to reject the QCD background. This is particularly important because the Monte Carlo simulation is not really reliable for the low energy background<sup>7</sup>.

---

<sup>4</sup>Two events can have very different amounts of hadronic activity but can have same  $\cancel{E}_T$ .  $\cancel{E}_T$  does not take into account event topology, so we need to work in terms of a probability that the  $\cancel{E}_T$  in a given final state is inconsistent with a fluctuation of the energy response of objects in the final state. Therefore the  $\cancel{E}_T$  is quoted relative to its uncertainty: it is named *met significance*

<sup>5</sup>As defined in sec. 3.1.1 the  $\chi^2$  define the goodness of track fit. Here the  $\chi^2$  probability cut is intended to reject kaon decays-in-flight that can be mistaken as muons [76].

<sup>6</sup> $jetillr$  ( $i = 1, 2$ ) is a variable indicating if the jet is coming from a gluon rather than a quark. With this cut we drastically reduce the statistics: we will relax it when an estimation of QCD background will be available.

<sup>7</sup>Since the QCD background is mostly present in the lower tail of the energy spectrum we can reduce its effect using harder energy cuts

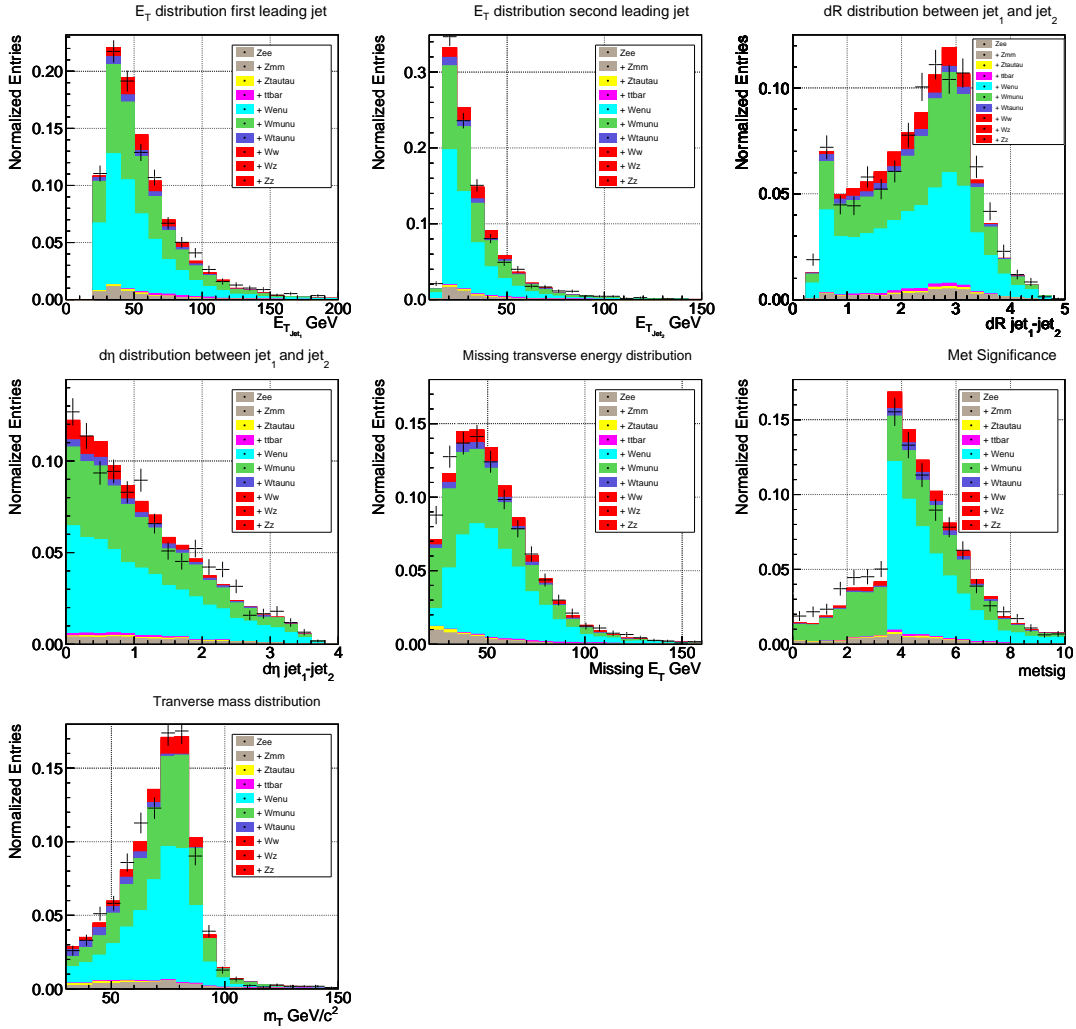


Figure 4.1: Distributions used to check the agreement between Data and MC and validate the cuts. The shape study shows that the adopted cuts are not fully optimized. However, they are adequate for studying the impact on the invariant mass resolution of the new tools being developed.

## Chapter 5

# Optimization of dijet Invariant Mass Resolution: Tracker-based methods

With reference to  $Z$  ( $H$ ) decay into two jets, we discuss in this chapter how to improve the resolution in the invariant mass of a dijet system. We first consider using tracking information in order to correct the jet direction as measured in the calorimeter. We note that in the dijet invariant mass a term depends on the opening angle between the two jets, which would profit from an improved measurement of the jet directions. By comparing jet directions measured in the calorimeter and in the tracker, we study how a correction to the jet energy can be applied. This study is on Monte Carlo simulated events only. We selected  $WZ \mapsto l\nu q\bar{q}$  events from HepgBank and studied  $Z$ -decay into any not- $b$  quark pair. In a first study  $b$ -jets were excluded in order to avoid applying  $b$ -specific jet corrections. All studies are based on the HepgBank generator (PYTHIA MC ).  $Z$ -decay quarks are studied in the WZ lab system. As first step we replaced the calorimeter jet axes with the direction of the primary quarks. This is done in order to gauge the maximum possible improvement one could shoot for in an experiment, where the tracker info would be used rather than the primary quark directions. As a second step, we compare the calorimeter jet energy to the quark energy and look for a correlation between its mismatch (not measurable) and the shift in the jet axis between calorimeter and tracker (measurable). We conclude this chapter describing a promising method to correct jet energy exploiting the charge component of jets as measured in the tracker.

## 5.1 MC Sample

We develop our method by studying how well we can reconstruct the mass of the Z decaying into pairs of u, d, s, c quarks. The adopted  $WZ \mapsto l\nu q\bar{q}$  PYTHIA MC samples<sup>1</sup> contain jets reconstructed within a  $dR = 0.4$  cone and corrected up to L7. Unless differently specified, these parameters will be used throughout the paper. As a start, the study considers all jets within  $|\eta| < 2$ . Some other constraints are:

- only 2 exclusive jets:

$$Et_{jet1_{upL7}} > 25 \text{ GeV and } Et_{jet2_{upL7}} > 15 \text{ GeV}$$

$$Et_{jet_i_{upL7}} < 5 \text{ GeV for } i \geq 3$$

- $dR(qclos, jet_1) < 0.7$  and  $dR(qclos, jet_2) < 0.7$

The last constraint defines the range over which the search for the primary quark of a jet is performed. A quark is associated to a jet when its direction falls within  $R < 0.7$  from the calorimeter jet axis.

## 5.2 Initial Considerations

The idea of choosing as jet directions those measured in the tracker originated from Montecarlo studies which showed that **tracker jets** are closer to primary partons than calorimeter jets. If we consider jets (both calorimeter and tracker) in the acceptance region of the tracker we obtain fig. 5.1.

We observe that 1.28 % more tracker jets match one primary parton within  $dR < 0.7$ . If we split this plot considering separately jets into crack and into nocrack regions (see below for a precise definition of these regions) we find that in the crack region the improvement is slightly better(fig. 5.2), with 1.32% more jets close to a primary parton within  $dR < 0.7$ .

From these preliminary studies we could expect some improvement by using tracker jets direction as axis of calorimeter jets. As a first step, before applying tracker jets direction we perform the correction of **caljets** axis using the direction of the primary quark. These studies indicate how much the angular term affects the dijet invariant mass and provide an upper limit to the progress possibly achievable in practice.

---

<sup>1</sup>The decay into a tau lepton was rejected at generator level. We checked that including this channel doesn't affect any distribution of interest.

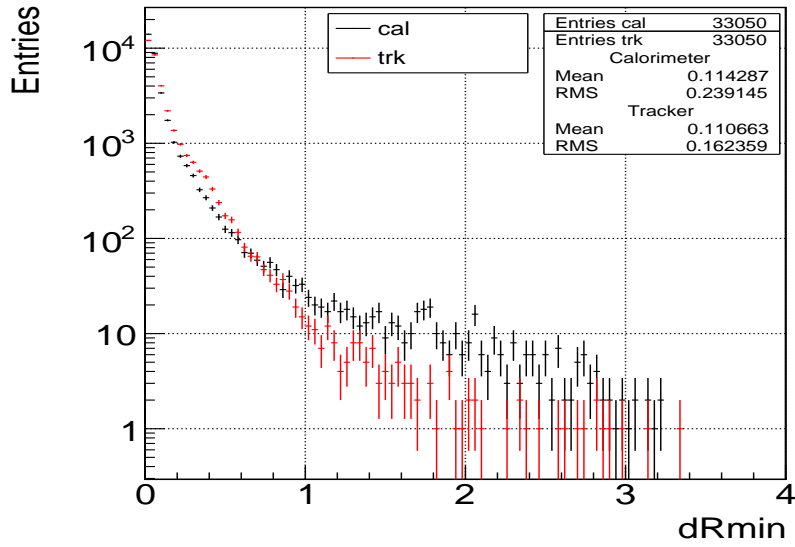


Figure 5.1:  $dR$  minimum between partons and caljets (black points) or trackjets (red points). Tracker acceptance region is  $|\eta_{det}| < 1$ .

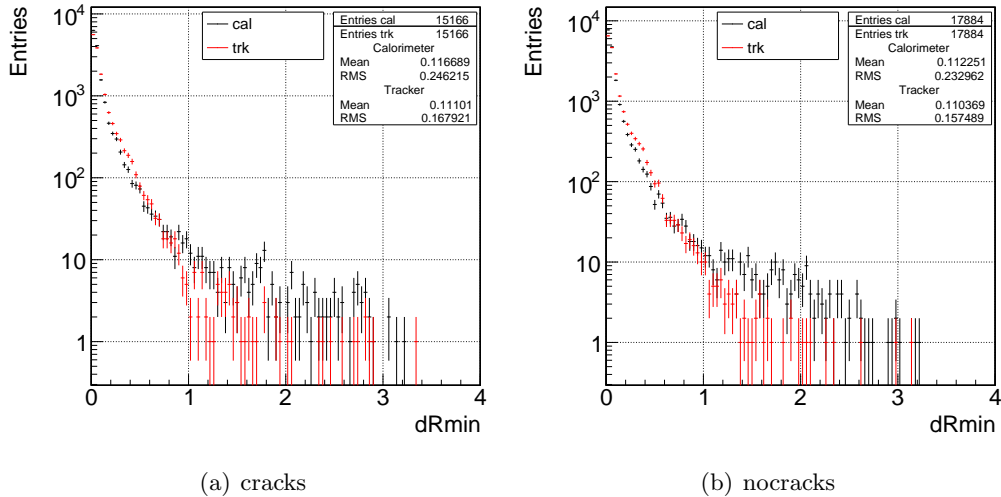


Figure 5.2:  $dR$  minimum between partons and caljets (black points) or trackjets (red points) considering jets in cracks regions (a) or in nocracks region (b) only

We have to note that, when used to select detector regions, partons (`caljets`, `trackjets`) are moved from the event vertex to the detector center. This is because of the projective nature of the calorimeter towers. The goodness of our function that moves the vertex of interaction from real to detector vertex is checked in appendix H.

### 5.3 Invariant Mass Studies

Figure 5.3(a) shows the Z mass at generation, and fig. 5.3(b) shows the Z mass as measured by the calorimeter. These distributions will serve as a reference for all the following studies.

In the calorimeters one can get a deformed view of the jet shape because of the cracks. This effect may shift the observed jet axis away from the true one. To gauge the possible improvement obtained by correcting the jet axis, we assume as jet axis the direction of the associated primary quark. If this would provide an improvement in dijet mass resolution, one might hope that also an estimate of the direction of the primary quark, as provided bias-free by the tracker, would give some benefit. The results of these studies are reported in fig. 5.4 and in tab. 5.4. The figure shows the reference distribution (a) on the left (mean mass  $91.7 \text{ GeV}/c^2$ , width  $10.4 \text{ GeV}/c^2$ ) and the modified distribution (b) on the right (mean mass  $92.8 \text{ GeV}/c^2$ , width  $10.3 \text{ GeV}/c^2$ ) when the quark direction is used as jet axis. We perform a Gaussian fit of the peaks between  $[mean - 1\sigma, mean + 2\sigma]$ , where mean and  $\sigma$  are provided by a Gaussian fit over the full Z peak of the reference plot, 5.4(a) [78],[79]. The improvement in the ratio width/peak ( $\frac{\sigma_2/\mu_2 - \sigma_1/\mu_1}{\sigma_1/\mu_1}$ ) is  $\sim 2.10\%$ . Since the effect is small but visible, we proceed to more detailed studies. In the crack regions of the calorimeters the lost energy is rescued in average by the energy corrections. However, in the cracks the jet axis could also be displaced from the primary parton direction. This displacement cannot be corrected by energy corrections. We therefore study the effect of adopting the quark directions as jet axis when jets are directed towards a calorimeter crack.

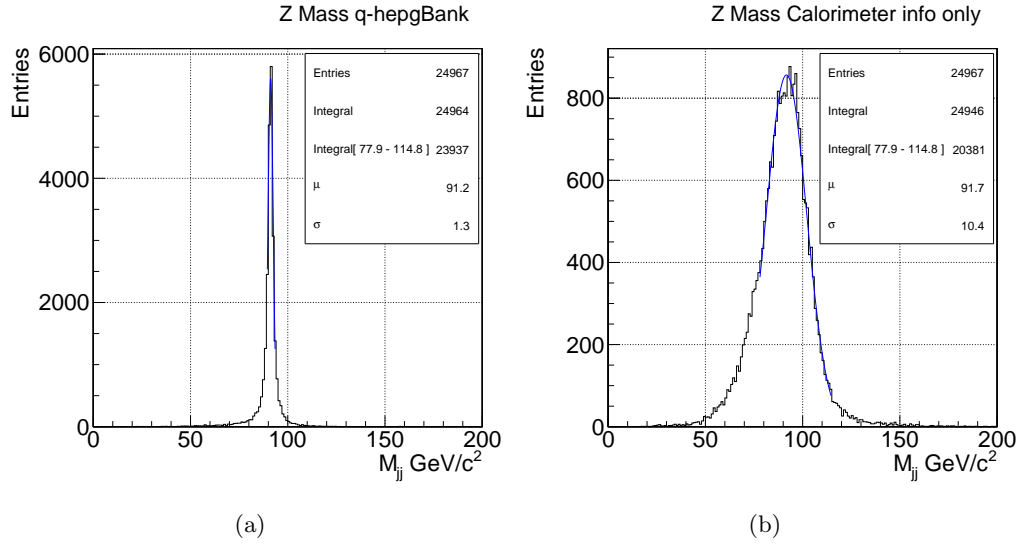


Figure 5.3: diquark  $Z$  mass at the generation level (fig. 5.3(a)) and as reconstructed with the calorimeter leading jets corrected up to level 7 (fig. 5.3(b))

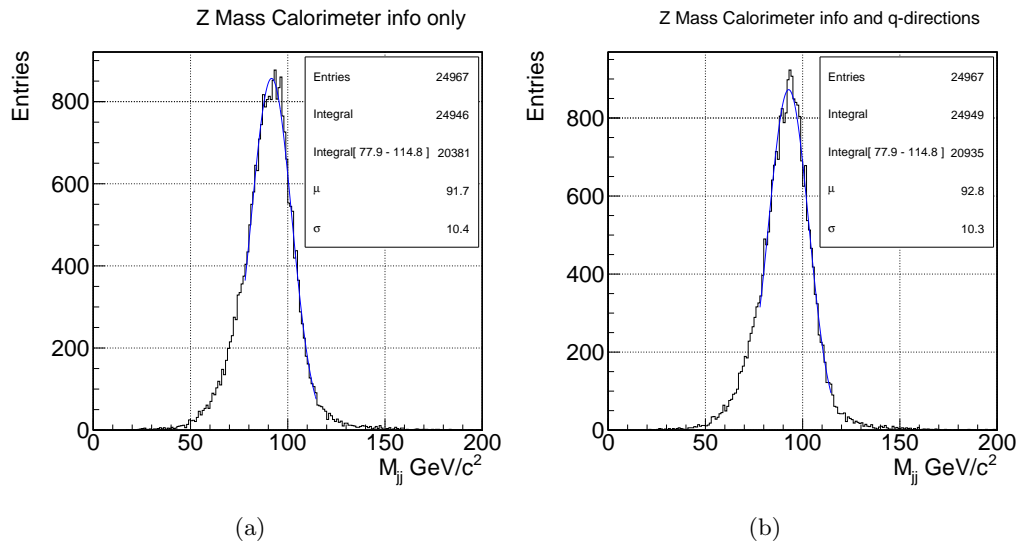


Figure 5.4: Calorimeter  $Z$  mass (the same as in fig. 5.3(b)) on the left, and modified distributions when the parton directions are taken as jet axes on the right. The performed Gaussian fits to the region around the peak are superimposed

## 5.4 Correcting the Axis of Jets in Cracks

We divide the detector in different regions:

- cracks:

$$|\eta| < 0.2;$$

$$|\eta| > 0.7 \text{ and } |\eta| < 1.4;$$

- nocracks:

$$|\eta| > 0.2 \text{ and } |\eta| < 0.7;$$

$$|\eta| > 1.4 \text{ and } |\eta| < 2.0;$$

As described above crack regions are selected using  $\eta_{det}$  as needed to correctly indicate the jet point of impact on the calorimeter. In tab. 5.4 we report a number of parameters of the distributions

- $\mu_{std}$  = Calorimeter Z mass;
- $\sigma_{std}$  = Calorimeter Z width ;
- $\mu_{mix}$  = Mean mass of distribution when using parton direction;
- $\sigma_{mix}$  = Width of distribution when using parton direction;
- $G = \frac{\sigma_{std}/\mu_{std} - \sigma_{mix}/\mu_{mix}}{\sigma_{std}/\mu_{std}}$  ;
- Evt/Wind. = difference between number of events in the selected mass windows [ $mean - 1\sigma$  ,  $mean + 2\sigma$ ];

We observe that when both jets are away from cracks (4<sup>th</sup> column) the mass scale is shifted but the width is significantly better than for jets over the full  $|\eta| < 2$  range (fig. 5.3(b)). In the samples where jets hit some crack (3<sup>rd</sup> column), correcting the direction of the jet axis gives a modest improvement of the width/peak ratio. The relevant result of tab. 5.4 is in the last column: when both jets are in the cracks region (last column) we have a 4.41% of improvement. Since this is an upper limit and this subsample represent the 20% of the entire sample we conclude that a substantial improvement cannot be expected by using tracker jet directions.

	ref. values:fig. 5.4(a)	1 jet in cracks	2 jets in nocracks	2 jets in cracks
$\mu_{std}$	91.7	91.4	92.2	90.7
$\sigma_{std}$	10.4	10.5	9.9	10.9
$\frac{\sigma_{std}}{\mu_{std}}$	11.35%	11.46%	10.68%	12.03%
$\mu_{mix}$	92.8	92.7	93.4	91.9
$\sigma_{mix}$	10.3	10.3	10.0	10.6
$\frac{\sigma_{mix}}{\mu_{mix}}$	11.14%	11.11%	10.68%	11.50%
<b>G</b>	<b>1.87%</b>	<b>3.08%</b>	<b>0.02%</b>	<b>4.41%</b>
<b>Evt/Wind.</b>	<b>2.21%</b>	<b>2.08%</b>	<b>2.38%</b>	<b>2.01%</b>

Table 5.1: *Effect of assuming parton direction as jet axis. The top row indicates the selected cracks. Crack regions are defined by parton directions in the lab frame. The 3 top lines give the mass and width of the mass fits using calorimeter jets, the 3 lower lines give the results of the fit to the same sample with parton directions as jet axes. The next to the last line gives the relative decrease of the  $\sigma/\mu$  ratio, and the last line gives the percentage difference in the number of event in the selected mass window.*

## 5.5 K Scale Factors

We now consider whether rather than correcting jet directions only, combined corrections to jet energy as well as to jet direction can provide better results.

For each Z decay jet we compute the ratio k between the energy of the primary parton and the calorimeter jet energy, and correlate it to the separation between jet axis and primary parton direction. We shall correct jet energy and angle in a number of ways. We define

- **std** invariant mass = Z mass using calorimeter info only;
- **mix** invariant mass = Z mass using calorimeter energy and parton directions;
- **k** invariant mass = Z mass using calorimeter energy corrected by the k factor (see below);
- **mixk** invariant mass = Z mass using calorimeter energy corrected by the k factor (see below), and parton directions;

The scatter plot of the ratio between the momentum of the closest parton to

the jet ( $dR < 0.7$ ) and the jet momentum ( $k = P_{q_{clos}}/P_{jet}$ ) versus the distance in R between their axes ( $dR(q_{clos}, jet)$ ) is shown in fig. 5.5 for Z-jets in the region  $|\eta| < 2$ . The distribution of the average  $k$  as a function of  $dR$  is shown in fig. 5.6

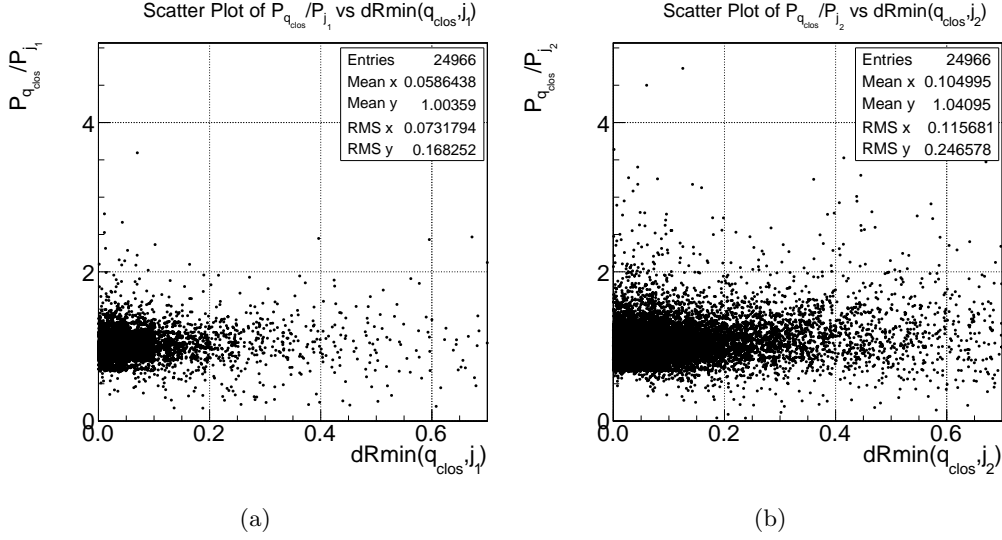


Figure 5.5: Scatter plot of  $k = \frac{P_{q_{clos}}}{P_{jet}}$  Vs  $dR(q_{clos}, jet)$  for Z-jets at  $|\eta| < 2$ . Left, leading jet; Right, next-to-leading jet.

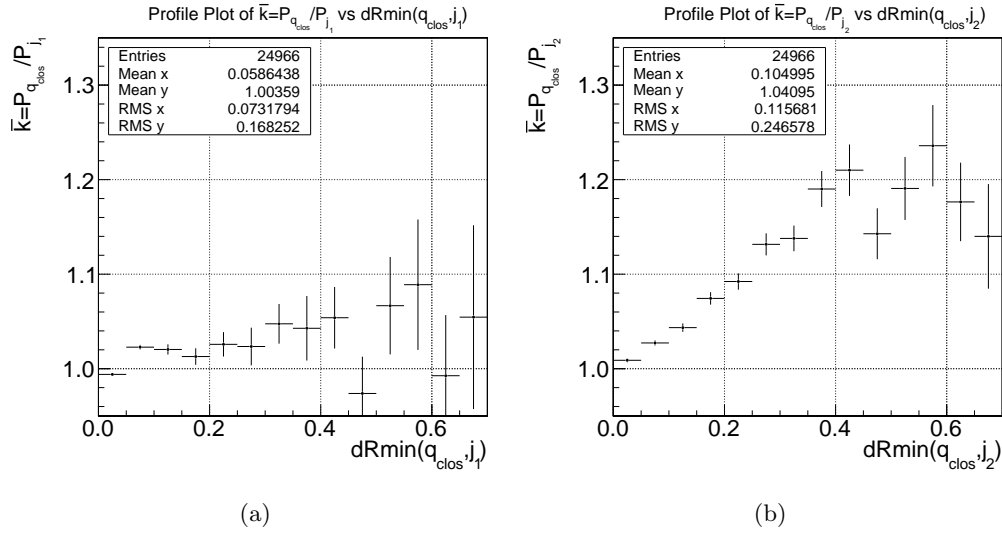


Figure 5.6: Distribution of  $\bar{k} = \langle \frac{P_{q_{clos}}}{P_{jet}} \rangle$  Vs  $dR(q_{clos}, jet)$  for jets in fig5.5. Left, leading jet; Right, next-to-leading jet.

One observes in fig. 5.5 a considerable spread in  $k$  values for any  $dR$ , the spread being larger for the sub-leading jet. Besides a larger number of jets whose energy

is under-estimated ( $k > 1$ ), there are also many jets whose energy is over-estimated ( $k < 1$ ). This spread indicates that even if the primary quark directions (i.e.  $dR$ ) could be measured with the tracker, only a modest improvement in resolution can be expected from an energy correction based only on  $dR$ . This expectation is confirmed by the following numerical studies. Figure 5.6 shows that at any  $dR$  the energy of the subleading jet is in average an underestimate of the parton energy ( $\bar{k} > 1$ ). This hints at an incorrect jet energy scale.

An appealing goal would be to approximate better the parton energy by applying specific corrections to either decrease or increase the jet energy. Under the tentative assumption that  $dR$  can be approximately measured in the experiment, we check the effect of  $\bar{k}$ -dependent corrections, with  $\bar{k}$  depending on  $dR$  as in fig. 5.6.

To apply jet energy corrections based on  $\bar{k}$  we adopt two methods:

- a) the  $\bar{k}$  values are picked bin by bin from the distributions in fig. 5.6;
- b) a linear fit over  $dR < 0.7$  to the distributions is used (see tab. 5.4 for fit parameter values). We also checked that fitting over a shorter  $dR$  range would not affect the result.

The Z mass and width are compared to the reference values in tab. 5.2. In the next to the last lines, **G** gives the relative change in width/mass from the reference value and **Evt/Wind.** gives the difference between the percentage of entries falling in the mass-windows, defined above, for  $k$  or mixk mass and reference values. The  $\bar{k}$  energy corrections can be combined with the jet axis corrections. The results are shown in tab. 5.3.

	std reference values	Method a)	Method b)
Z-mass	91.7	92.9	92.8
Width	10.4	10.2	10.2
$\frac{Width}{Z-mass}$	11.35%	10.98%	11.02%
<b>G</b>		<b>3.25%</b>	<b>2.91%</b>
<b>Evt/Wind.</b>		<b>2.36%</b>	<b>2.60%</b>

Table 5.2: *Effect of energy corrections by  $\bar{k}$*

From tab. 5.2 and tab. 5.3 one observes that the corrections increase the mass by several  $\text{GeV}/c^2$ , with little impact on the width. Therefore a modest improvement on the width/signal ratio is obtained. The corrections affect primarily events at

	std reference values	Method a)	Method b)
Z-mass	91.7	94.1	94.0
Width	10.4	10.3	10.3
$\frac{Width}{Z-mass}$	11.35%	10.91%	10.94%
<b>G</b>		<b>3.85%</b>	<b>3.59%</b>
<b>Evt/(mass.Wind.)</b>		<b>3.78%</b>	<b>3.93%</b>

Table 5.3: Energy corrections and jet axes corrections combined

large  $dR$ . With method a) the improvement in sigma/mean is 3.25% in the k mass, and 3.85% in the mixk mass. With method b) the improvement is 2.91% in the k mass and 3.59% in the mixk mass. Considering also the last row of tab. 5.2 and tab. 5.3 we conclude that the two methods are equivalent to each other. We decide to adopt method b) and we shall not consider method a) any further. We note that the modest improvement, mostly due to the shift in energy scale, persists even when tails in the mass distribution are excluded from the fit.

## 5.6 Correcting Energy of Jets in Cracks

In figures fig. 5.7 and fig. 5.8 we show the dependence of  $\bar{k}$  on  $dR$  for jets in cracks and in the no-cracks region. The left plots are for the leading jet ( $j_1$ ), the right plots are for the subleading jet ( $j_2$ ). We note that there is essentially no difference between crack and no-crack region

Table 5.4 shows intercepts and slopes of linear fits to  $\bar{k}$  distributions in the full  $dR < 0.7$  range. The corrections are in general positive and are much stronger for  $j_2$ .

	$a_{j_1}$	$b_{j_1}$	$a_{j_2}$	$b_{j_2}$
inclusive	$0.992 \pm 0.001$	$0.202 \pm 0.022$	$0.998 \pm 0.002$	$0.408 \pm 0.018$
cracks	$0.995 \pm 0.002$	$0.181 \pm 0.032$	$1.008 \pm 0.003$	$0.424 \pm 0.028$
nocracks	$0.990 \pm 0.002$	$0.242 \pm 0.027$	$0.991 \pm 0.003$	$0.402 \pm 0.024$

Table 5.4: Intercepts and slopes of linear fits.  $a$  and  $b$  are the parameter of the fitting function  $a + b \cdot x$

We have studied the effect of direction and  $\bar{k}$  corrections on the reconstructed Z mass splitting the events into three classes:

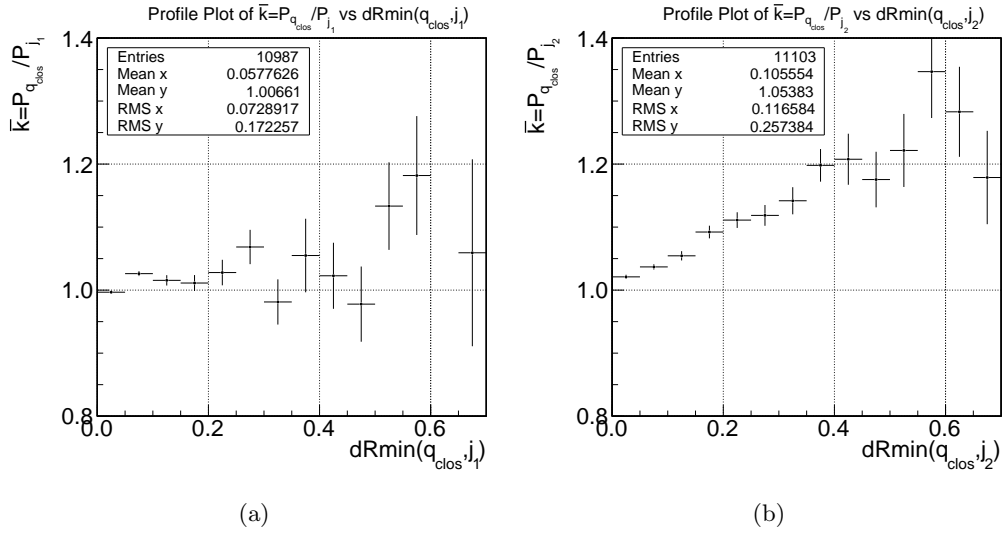


Figure 5.7:  $k$  factor for jets in cracks

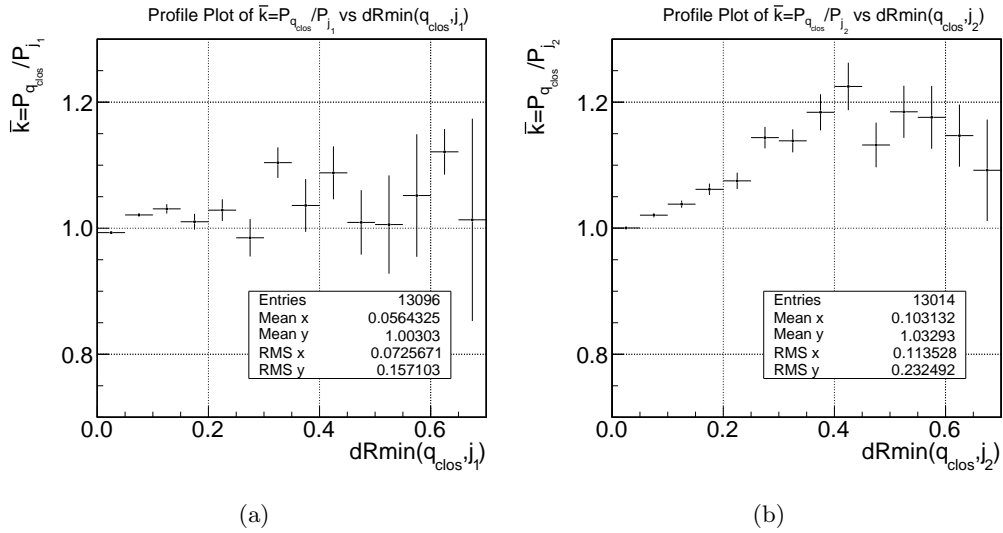


Figure 5.8:  $k$  factor for jets away from cracks

1. one jet is on cracks, the other is away from cracks
  
2. both jets are on some cracks.
  
3. both jets are away from cracks.

The results of fits over the mass range  $-1\sigma$  and  $+2\sigma$  as previously defined are reported in tab. 5.5 and tab. 5.6. A look at tab. 5.5 makes it clear as the  $\bar{k}$  corrections are almost *independent* of the position in the calorimeter. In general, in the inclusive study, combination of both  $\bar{k}$  and parton direction correction is more effective rather than one correction only (see tab. 5.2 and tab. 5.3). However, all together the effects are not large.

	ref. values fig. 5.4(a)	1 jet in cracks	2 jets in nocracks	2 jets in cracks
$\mu_{std}$	91.7	91.4	92.2	90.7
$\sigma_{std}$	10.4	10.5	9.9	10.9
$\frac{\sigma_{std}}{\mu_{std}}$	11.35%	11.46%	10.68%	12.03%
$\mu_k$		92.5	93.4	91.7
$\sigma_k$		10.3	9.7	10.9
$\frac{\sigma_k}{\mu_k}$		11.12%	10.34%	11.89%
<b>G</b>		<b>2.92%</b>	<b>3.21%</b>	<b>1.11%</b>
<b>Evt/Wind.</b>		<b>2.79%</b>	<b>2.37%</b>	<b>2.55%</b>

Table 5.5: Effect of  $\bar{k}$  correction in cracks. The top row indicates the selected crack: Crack regions are defined by parton directions in the lab frame. The 3 top lines give the mass and width of the fits for calorimeter jets, the next 3 lower lines give the results of the fit to the same sample with  $\bar{k}$  corrected parameters. The next to the last line gives the relative decrease of the  $\sigma/\mu$  ratio, and the last line gives the percentage difference in number of events in the selected mass window.

We now turn to study whether using tracker rather than quark information can preserve some progress. Given the previous results, we cannot expect much. However, we shall also explore whether the charged particle flux outside the jet cone can provide enough information on  $\bar{k}$  to allow building up specific jet corrections.

	ref. values fig. 5.4(a)	1 jet in cracks	2 jets in nocracks	2 jets in cracks
$\mu_{std}$	91.7	91.4	92.2	90.7
$\sigma_{std}$	10.4	10.5	9.9	10.9
$\frac{\sigma_{std}}{\mu_{std}}$	11.35%	11.46%	10.68%	12.03%
$\mu_{mixk}$		93.8	94.4	93.0
$\sigma_{mixk}$		10.3	9.9	10.8
$\frac{\sigma_{mixk}}{\mu_{mixk}}$		10.95%	10.43%	11.64%
<b>G</b>		<b>4.37%</b>	<b>2.33%</b>	<b>3.24%</b>
<b>Evt/Wind.</b>		<b>3.99%</b>	<b>3.81%</b>	<b>3.97%</b>

Table 5.6: Combined effect of assuming parton direction as jet axis and  $\bar{k}$  correction in cracks. The top row indicates the selected crack: Crack regions are defined by parton directions in the lab frame. The 3 top lines give the mass and width of the fits to the mass using calorimeter jets, the 3 next lines give the results of the fit to the same sample with parton directions as jet axes and  $\bar{k}$  corrected parameters. The next to the last line gives the relative decrease of the  $\sigma/\mu$  ratio, and the last line gives the percentage difference in number of events in the selected mass window.

## 5.7 Correcting Axis Using Tracker Info

Now we use tracker info to correct jet axis. As before, when partons were used, we select the closest tracker jet to calorimeter jet and use tracker jet axis to build invariant mass. This method would be applicable in the analysis of real data. We report in tab. 5.7 the results of these studies. We observe that using trackjets directions to correct calorimeter jet direction, rather than improving, would significantly degrade the resolution in all samples<sup>2</sup>.

### 5.7.1 Golden Sample

This negative result is surprising since the previous dR studies (see fig. 5.1) showed that **trackjets** are closer to parton than **caljets**. An explanation of this finding can possibly be found in the tracker insensitivity to neutral particle. If a large fraction of a jet energy is carried by neutrals, the information carried by the tracker on the jet axis would be poor. We explore this possible effect by studying a sample of events in which the electromagnetic fraction (**emfr**<sup>3</sup>) of the two leading jets

<sup>2</sup>The eta region considered is constrained to be less than 1 in  $\eta_{det}$

<sup>3</sup>Ratio between the EM and total calorimeter energy

	ref. values fig. 5.4(a)	1 jet in cracks	2 jets in nocracks	2 jets in cracks
$\mu_{std}$	91.7	91.25	92.2	91.0
$\sigma_{std}$	10.4	10.46	9.9	10.9
$\frac{\sigma_{std}}{\mu_{std}}$	11.35%	11.46%	10.71%	11.98%
$\mu$		91.8	91.36	90.3
$\sigma$		11.5	10.9	12.6
$\frac{\sigma}{\mu}$		12.69%	11.95%	14.00%
<b>G</b>		<b>-10.61%</b>	<b>-11.61%</b>	<b>-16.81%</b>
<b>Evt/Wind.</b>		<b>-5.87%</b>	<b>-12.57%</b>	<b>-14.61%</b>

Table 5.7: Effect of assuming trackjet direction as jet axis. The top row indicates the selected crack: Crack regions are defined by trackjet directions in the lab frame. The 3 top lines give the mass and width of the fits to the mass using calorimeter jets, the 3 next lines give the results of the fit to the same sample with trackjet direction taken in account. The next to the last line gives the relative decrease of the  $\sigma/\mu$  ratio, and the last line gives the percentage difference in the number of events in the mass window. the last two lines give the relative increase (negative gain **G**) in the  $\sigma/\mu$  ratio and the difference in the percentage of event in the selected mass window.

measured in the calorimeter is less than a reference value: We choose  $emfr < 0.5$  obtaining a subsample  $\sim 13\%$  the total sample. However, even in this sample the correlation between trackjets and partons is very much the same as in average jets, fig. 5.9.

## 5.8 Charge Fraction Studies

To complete our studies on the tracker, we turn our attention to other track-related observable, searching for event-specific corrections to `caljet` energy. We define the charge fraction (**chf**) as the ratio between  $P_{T_{trkclos}}/E_{T_{caljetRaw}}$ <sup>4</sup>. We study the effect of the  $k$  factor ( $k = P_q/P_{caljet}$ ) as function of **chf**, on the dijet mass ( $k_{chf}$  **mass**). The **chf** distributions are shown in fig. 5.10.

These distributions are different from each other, as already noted in previous CDF studies using a similar definition of the charge fraction, [80]. In figure fig. 5.11

<sup>4</sup>*caljetRaw* indicates calorimeter jets without correction, *trkclos* is the tracker jet closer to calorimeter one

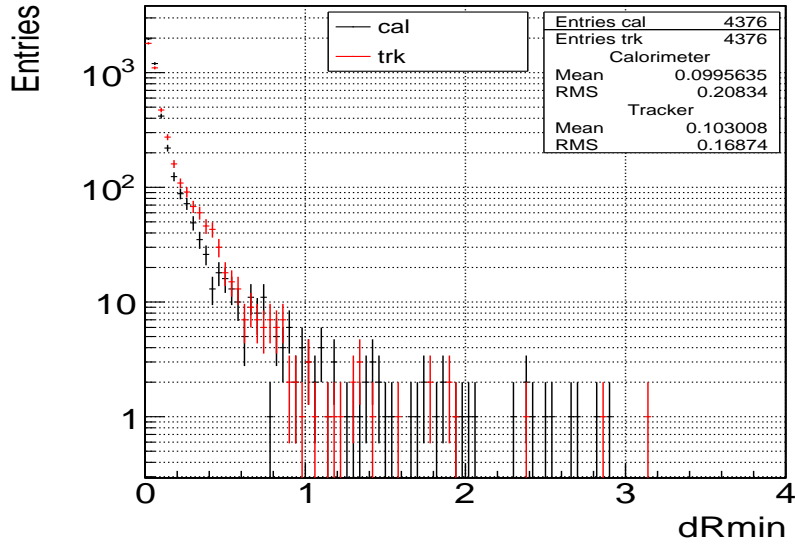


Figure 5.9:  $dR$  minimum between partons and caljets (black points) or trackjets (red points) in the sample with small neutral fraction jets

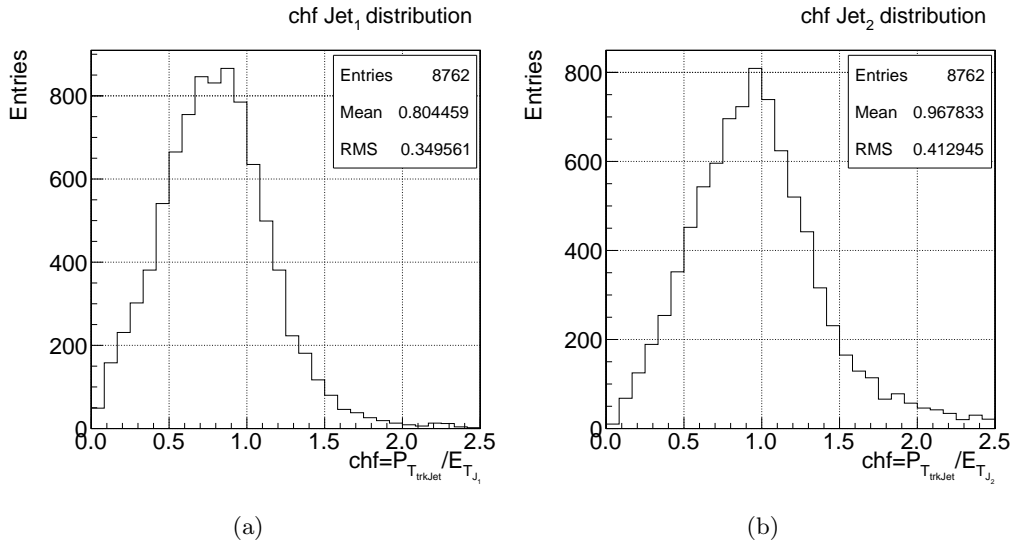


Figure 5.10: Charge fraction distribution for the first (a) and second (b) leading calorimeter jet

we show the  $\text{chf}$ -dependent correction factor for the two leading jets. Since these

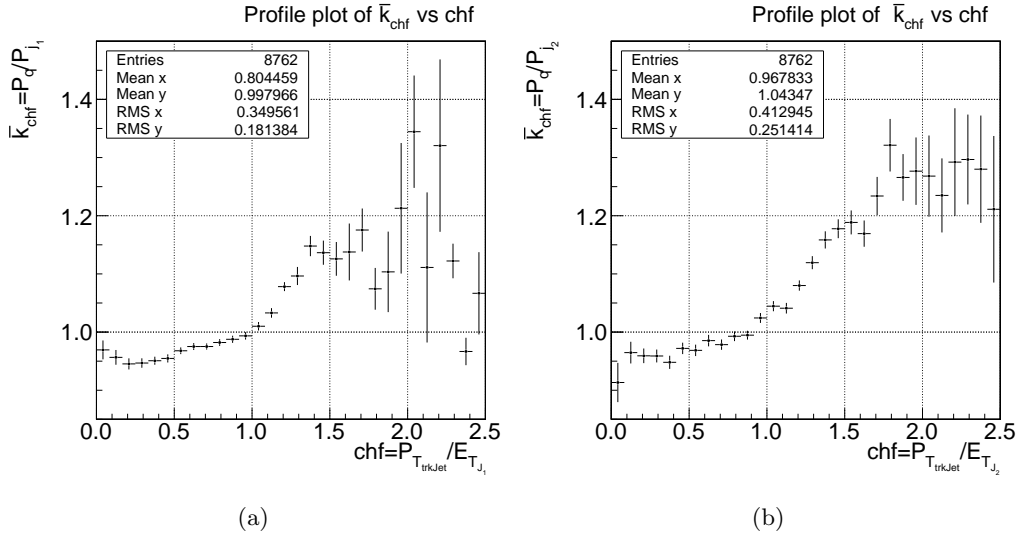


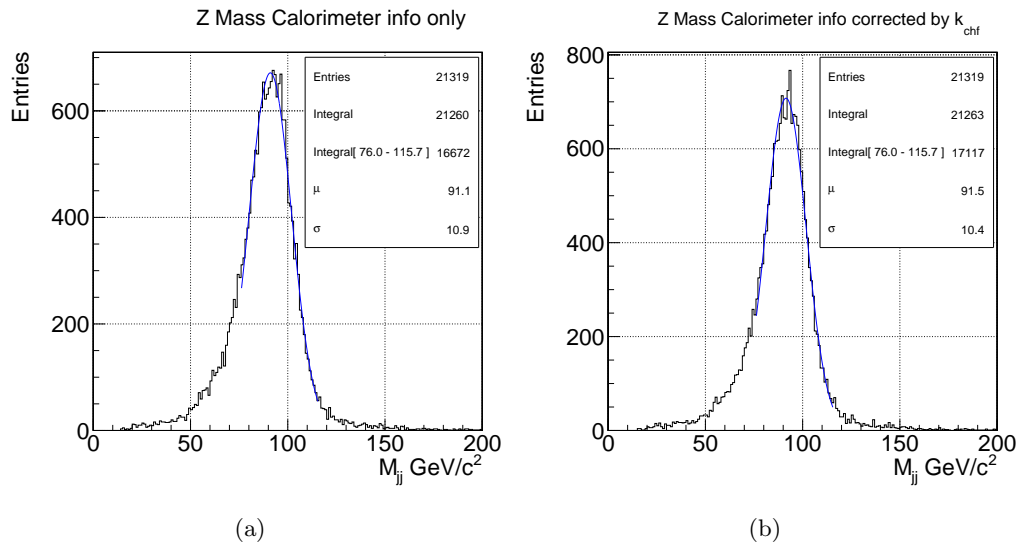
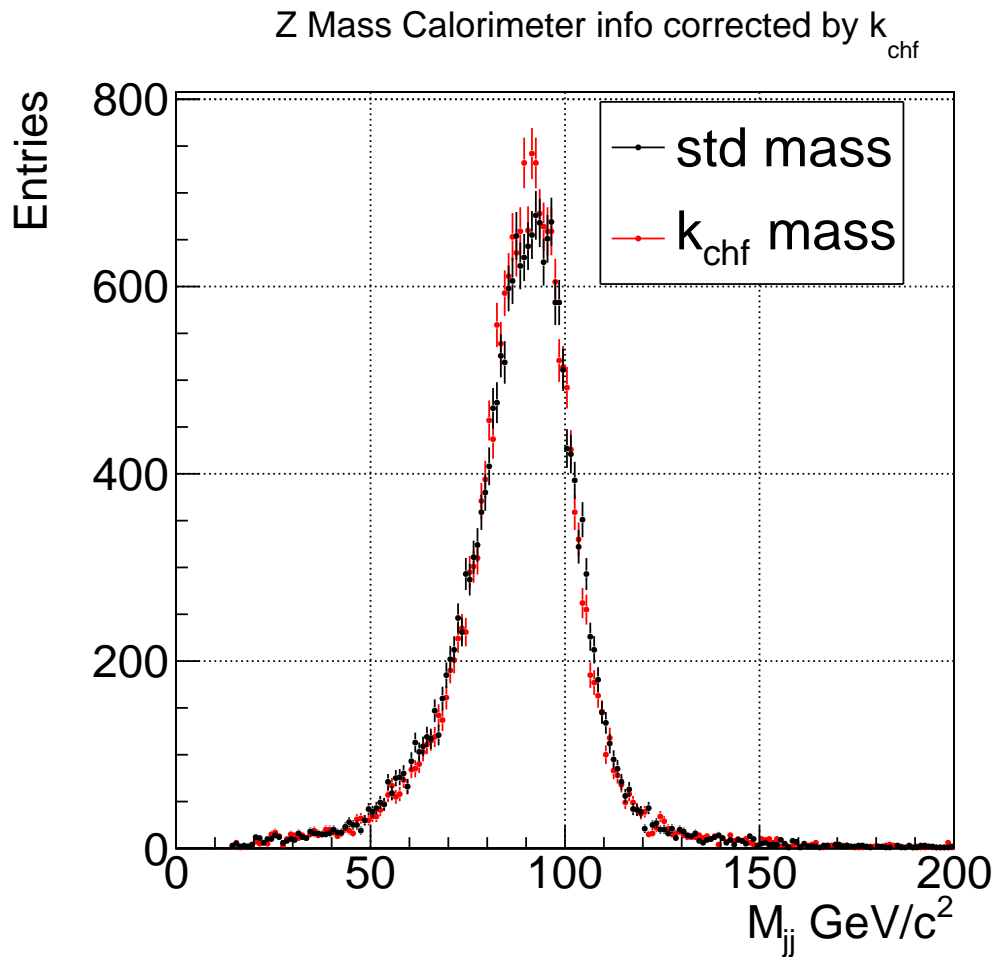
Figure 5.11: Profile plots of the scatter plot  $k$  vs  $\text{chf}$

distributions are fully compatible with each other (as should be expected), they have been combined and fitted to an analytical function to obtain a continuous correction to the jet energy as a function of the charge fraction<sup>5</sup>. After applying the correction the  $Z$  mass peak shown in figure fig. 5.12 is obtained. There is an improvement in the sigma/mean ratio of 4.07% over the original distribution (fig. 5.12(b)) and also of 1.41% in the number of events under the mass window. The two distribution of figure fig. 5.12 are superimposed in fig. 5.13.

This improvement is interesting in as much as it is better than the 2.91% previously obtained using the unphysical parameter  $dR_{(q\text{clos},\text{caljet})}$  (see tab. 5.2).

This last result is of real interest since the method can be implemented in the analysis of experimental data. Work is presently in progress on this iusse.

<sup>5</sup>We perform a parabolic fit til 1.4 and a linear fit in the range [1.4-2.0]

Figure 5.12: *Invariant mass standard (5.12(a)) and  $k_{\text{chf}}$  mass (5.12(b))*Figure 5.13: *Overlap between invariant mass standard (black) and  $k_{\text{chf}}$  mass (red)*



## Chapter 6

# Optimization of dijet Invariant Mass Resolution: Calorimeter-based methods

*In the following we discuss some calorimeter-based methods to improve the invariant mass resolution. In particular we shall search for some criteria to merge the third leading jet which is being disregarded in current analyses.*

### 6.1 Introduction

To perform studies on the third leading jet we select  $WZ \rightarrow \nu q \bar{q}$  events with the following cuts<sup>1</sup>:

- a *third tight jet*<sup>2</sup> can be present;
- $E_{t_{jet1_{upL7}}} > 25$  GeV;
- $E_{t_{jet2_{upL7}}} > 15$  GeV;
- $|\eta_{jet1_{upL7}}| < 2$ ;
- $|\eta_{jet2_{upL7}}| < 2$ .

---

<sup>1</sup>In order to increase the Monte Carlo statistics we included also the  $Z \rightarrow b\bar{b}$  decay channel. This channel is not distinguishable from the light quark channel in the present analysis

<sup>2</sup>In our convention a *tight jet* is a jet with  $E_{T_{j3}} > 15$  GeV

From now on the inclusive sample will be divided in two subsample:

1. *three tight jets sample*:

$$Et_{jet3_{upL7}} > 15 \text{ GeV and } |\eta_{jet3_{upL7}}| < 2;$$

2. *two tight jets sample*: the inclusive sample after removing the *three tight jets sample*;

Because of this extra-jet, in the sample 1 the resolution of the dijet invariant mass built with the first two leading jets, fig. 6.1, worsens. In fig. 6.1(a) increased tails relative to fig. 6.1(b) are clearly visible at low as well as at large mass. This effect may in part be due final state radiation. It might be corrected by considering the third jet.

With reference to this data sample, we note that including events with a third jet has increased the sample by  $\sim 39\%$ . Therefore any improvement in this subsample would have a significant impact on the whole sample.

We describe in the following some methods to make use of the third jet in building the Z mass. These will be based on studies of the probability of jet-to-parton association in the new sample.

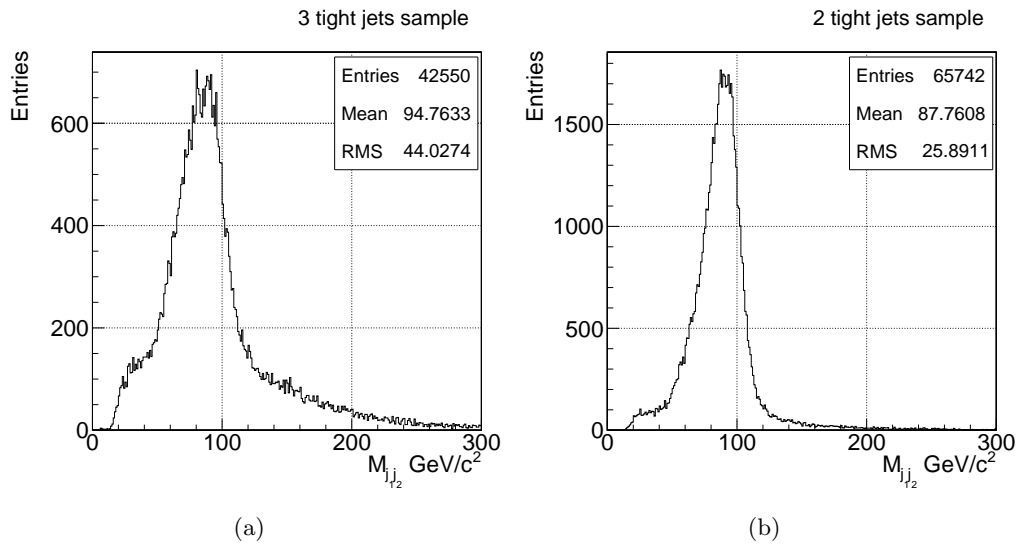


Figure 6.1: *Dijet invariant mass built with first and second leading jet in the sample with more than two tight jets (“three tight jets sample”, (a)) and in the sample with only two tight jets (“two tight jets sample” (b)). We call tight a jet with transverse energy greater than 15 GeV after Level7 correction are applied.*

## 6.2 Three Tight Jets Subsample

In fig. 6.2 the scatter plot between  $M_{j_1j_2}$  and  $dR_{j_1j_2}$  is shown. Four different mass regions are defined<sup>3</sup>. In tab. 6.1 there is a numerical definition of the outlined regions. We address first region A, where an increased event density with anomalously low mass is observed at small  $dR_{j_1j_2}$ .

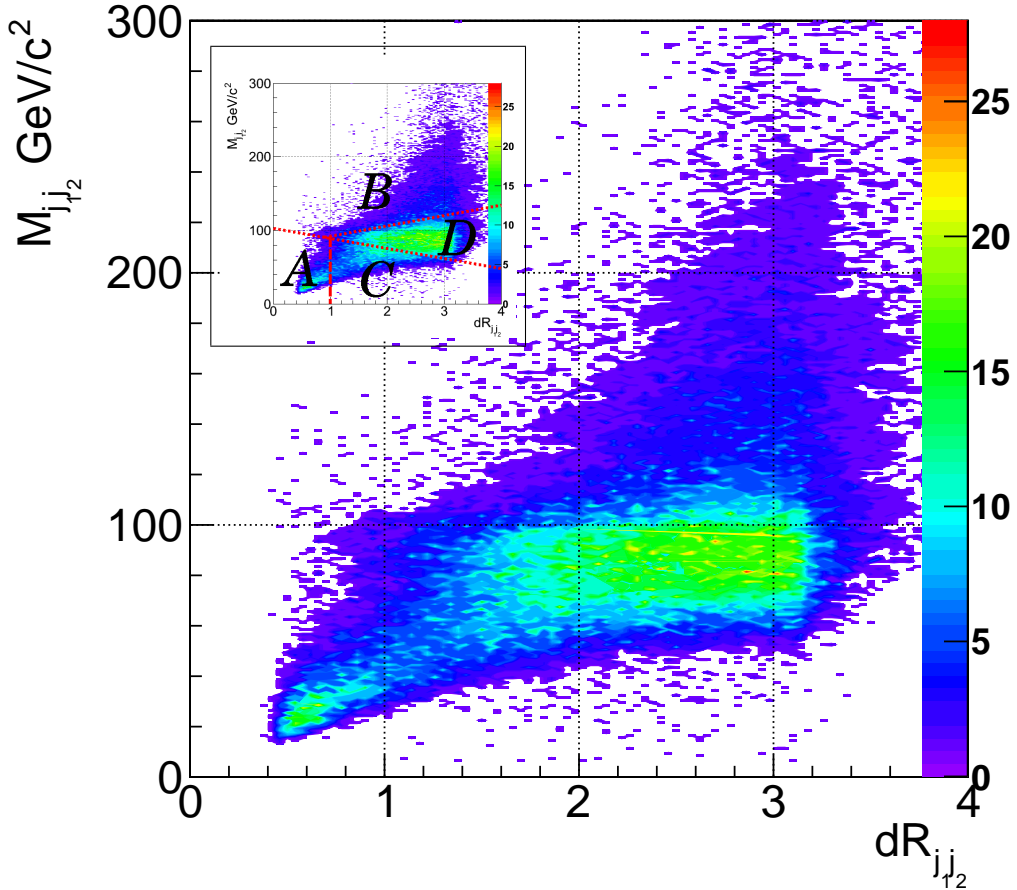


Figure 6.2: Scatter plot of the invariant std mass versus  $dR_{j_1j_2}$ .

This behaviour is likely to be linked to a Final State Radiation (*FSR*) effect. The grouping of  $M_{j_1j_2j_3}$  around the Z-mass in this zone (fig. 6.3(1)) suggests to merge the third jet in computing  $M_Z$ . Figure 6.4 shows the impressive improvement that

<sup>3</sup>These regions were defined based on qualitatively considerations. When Z-decay quarks have large  $dR$  they have relatively low energy. Since the calorimeter relative energy resolution (see sec. 2.5) is worse at lower energies, the fluctuations on the reconstructed mass will be larger. This explains the widening of the  $M_{jj}$  in D-region with increasing  $dR$ . Work is in progress to optimize the choice of regions.

Region	limits
A	$Line_1 < 0$ and $dR_{j_1j_2} < 1$
B	$Line_1 > 0$ and $dR_{j_1j_2} < 1$ $Line_2 > 0$ and $dR_{j_1j_2} > 1$
C	$Line_1 < 0$ and $dR_{j_1j_2} > 1$
D	$Line_1 > 0$ and $Line_2 < 0$ and $dR_{j_1j_2} > 1$

Table 6.1: Numerical definition of the region shown in fig. 6.2.  $Line_1$  and  $Line_2$  are described by the the equation  $(2.3 \cdot M_{j_1j_2} + 31 \cdot dR_{j_1j_2} - 237.2 = 0)$  and  $(2.3 \cdot M_{j_1j_2} - 29 \cdot dR_{j_1j_2} - 183.2 = 0)$  respectively.

is obtained using this criterion for zone A events. We show in figure fig. 6.5 the rate of correct jet-to-parton matching for jet pairs in zone B. The best chance is for pair 1-3 ( $\sim 31\%$  of times, entry at  $IdSum = 2$  in figure, rather than  $\sim 20\%$  for pair 1-2, entry at  $IdSum = 1$  in figure). As a first attempt we pick the  $j_1j_3$  pair to work out the Z-mass in this region. The resulting remarkable improvement in the Z-signal is shown in fig. 6.6. Work is in progress on a weighted average of the mass returned by all combinations.

Work is in progress to find an improved jet combination for zone C. For the time being we still use the standard  $j_1j_2$  pair to compute the Z-mass. This is done in zone D as well where  $j_1$  and  $j_2$  appear to preserve the bulk of the information on the Z-mass.

Figure 6.7 shows the Z-mass distribution when the modified jet selections in zone A ( $M_Z = M_{j_1j_2j_3}$ ) and B ( $M_Z = M_{j_1j_3}$ ) are chosen. A significant improvement in resolution is observed. In tab. 6.2 we report the improvements in the ratio  $\sigma/\mu$  and the percentage of event recovered under the peak.

### 6.3 Two Tight Jets Subsample

Although the third jet must have  $E_t < 15$  GeV, some impact of *FSR* can be expected also in the *two tight jets sample*. We apply the merging procedure in Zone A<sup>4</sup> in this sub-sample as well. Figure 6.8 shows the expeted result. The change is small but visible with an improvement of 0.84% in the number of events within the mass window.

<sup>4</sup>No evidence of wrong jet-to-parton association had been found in this sub-sample: This is why we use only the Zone A criterion ( $M_Z = M_{j_1j_2j_3}$ ).

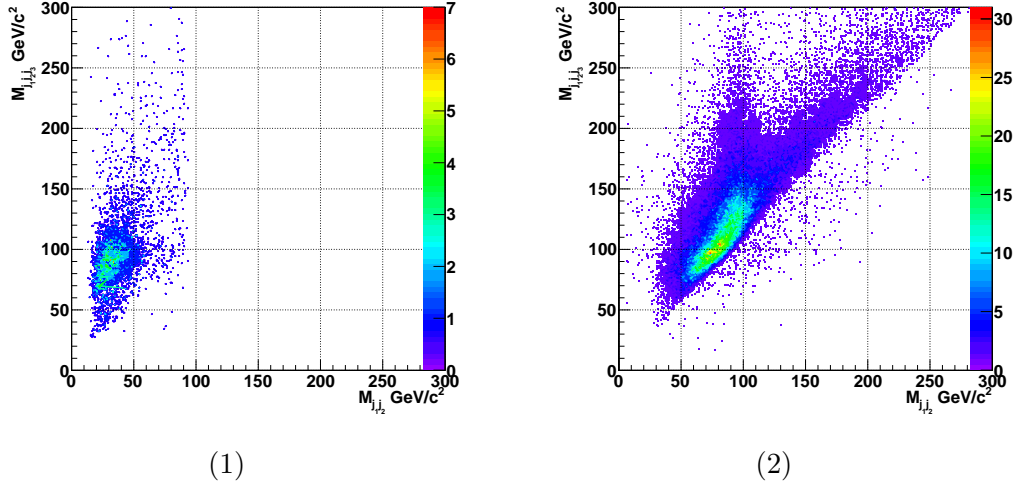


Figure 6.3: Scatter plot of the invariant mass  $M_{j_1 j_2 j_3}$  the standard  $M_{j_1 j_2}$  in zone A (1) and in zones B-C-D (2). The grouping of  $M_{j_1 j_2 j_3}$  around the Z-Mass in (1) suggests that one jet may be due to FSR. The upward spray of events at large  $M_{j_1 j_2 j_3}$  for  $M_{j_1 j_2}$  around the Z-Mass in (2) is suggestive of ISR

## 6.4 Results on the Inclusive Sample

As we have seen so far a very significant improvement can be obtained in the three *tight jets subsample*, but a very small gain is present when applying just the ( $M_Z = M_{j_1 j_2 j_3}$ ) criterion to zone A in the sample with only *two tight jets*. We report in tab. 6.3 and fig. 6.9 the results on the whole sample when the above criteria for correcting the  $j_1 j_2$  mass in Zone A ( $M_Z = M_{j_1 j_2 j_3}$ ) and B ( $M_Z = M_{j_1 j_3}$ ) are applied. The gain in resolution is  $\sim 2\%$  and the increasing of rate in mass window  $\sim 5.3\%$ . Studies are continuing to improve this result.

## 6.5 Including the Third Jet all-over

We considered including the third jet whenever two out of jets  $j_1$ ,  $j_2$  and  $j_3$  are close to each other. Figure 6.10 shows that an improvement is obtained in the low mass tail of the distribution but that the tail at large mass is increased. We suspect that this effect be principally due to *ISR* jets. Work is in progress to find some criteria to “tag” the *ISR* and be able to combine jets in the event to get the best measurement of the Z mass.

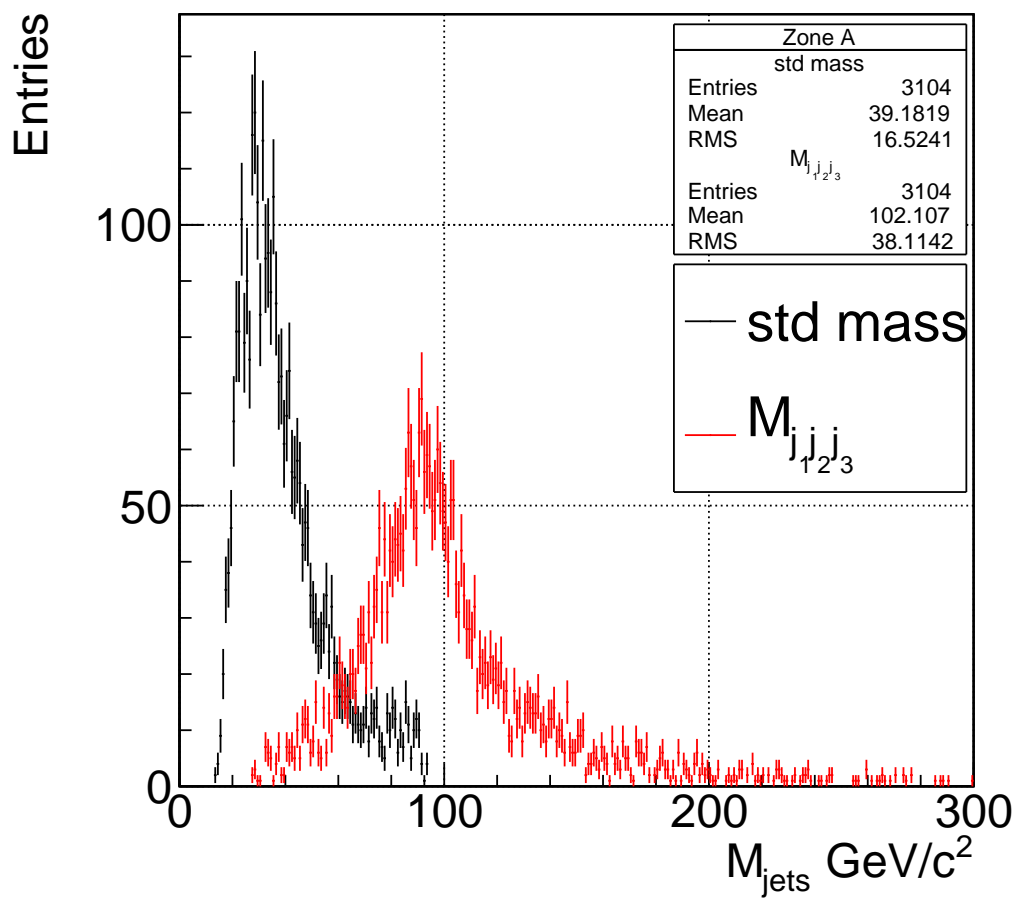


Figure 6.4: Effect of merging the third leading jet for Zone A events in the three tight jets sample.

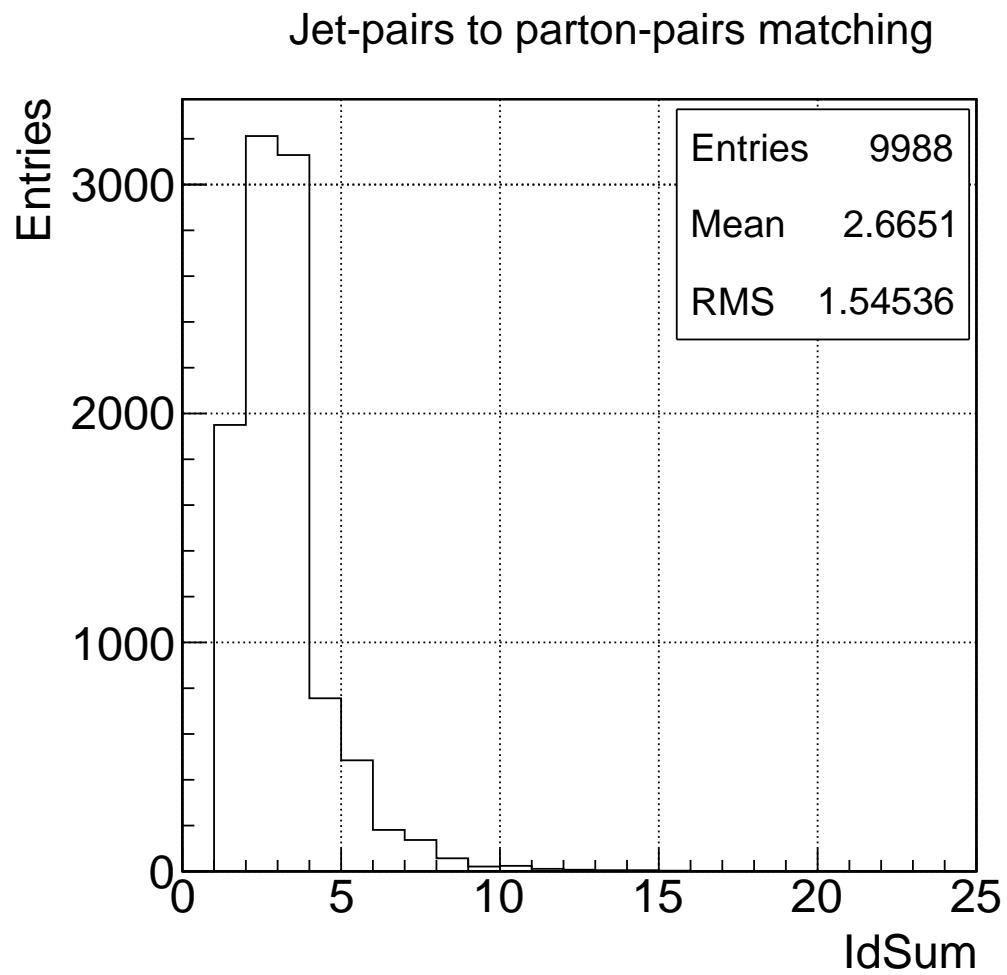


Figure 6.5: Rate of correct jet matching to partons for both jets of the selected pair. Entries are:  $IdSum = 1$ ,  $j_1j_2$ ;  $IdSum = 2$ ,  $j_1j_3$ ;  $IdSum = 3$ ,  $j_2j_3$ .

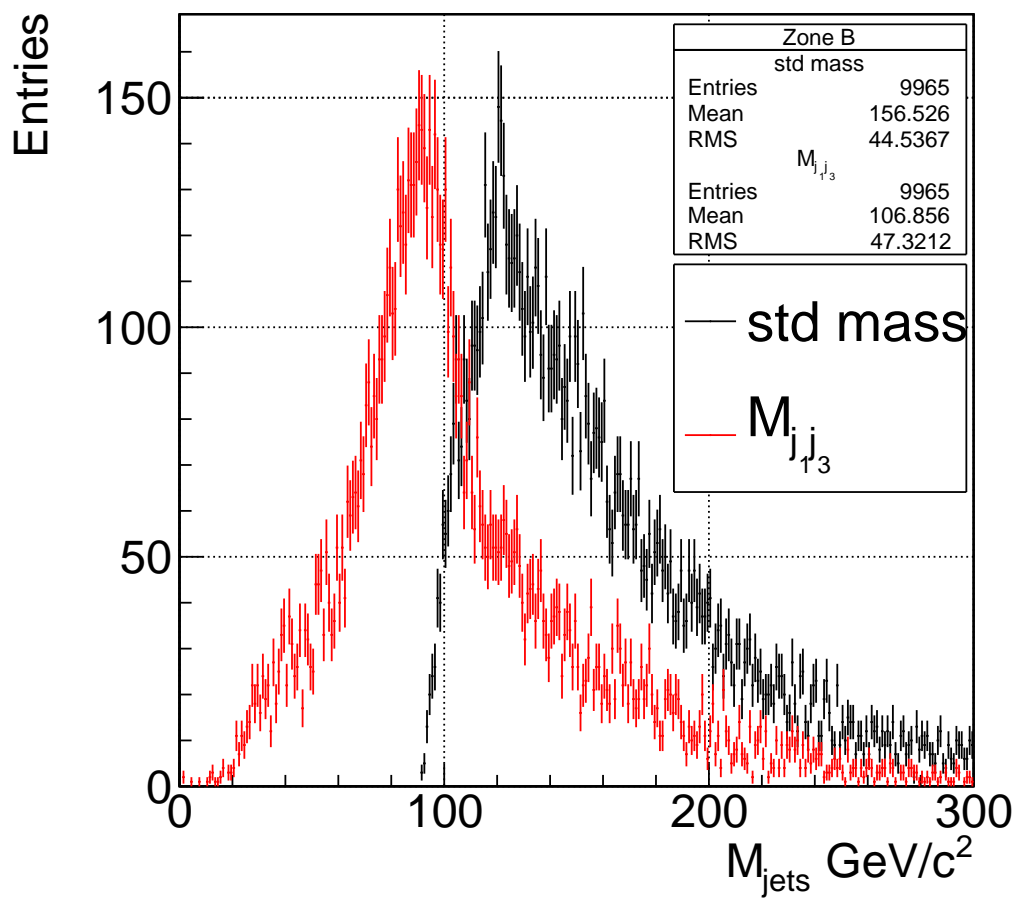


Figure 6.6: Effect of using the third leading jet instead of the second one for Zone B events in the three tight jets sample.

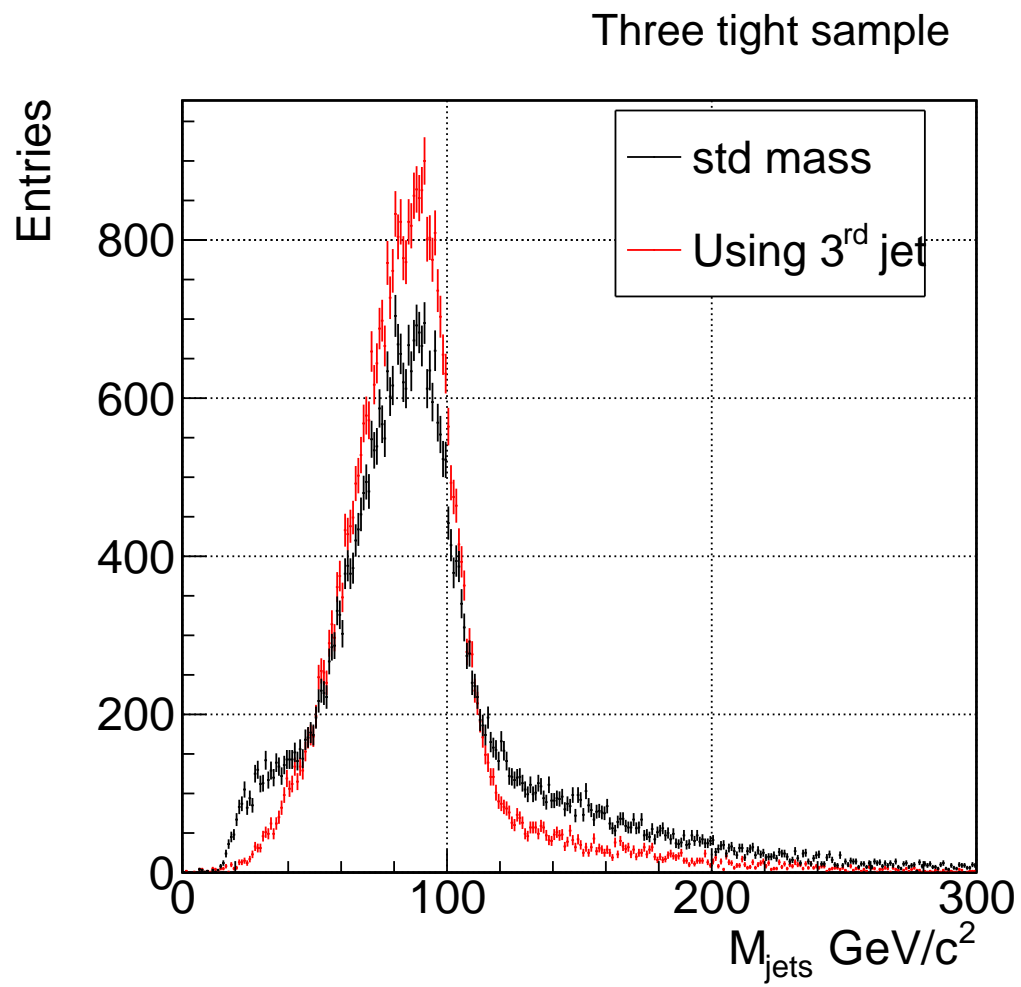


Figure 6.7: *Three tight jets subsample. Comparison between std-mass (Black) and mass when the modified criteria are applied in zone A and zone B (Red)*

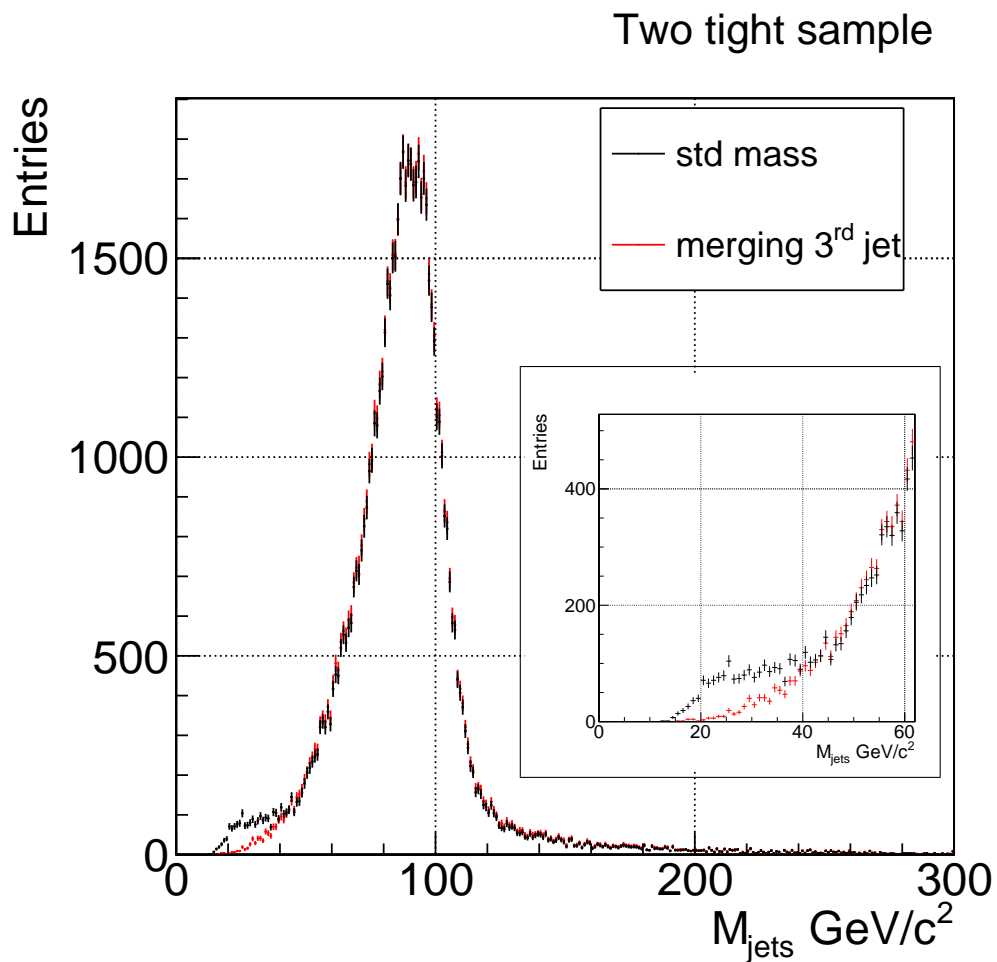


Figure 6.8: Comparison between *std-mass* and mass when the third jet is included in the *Z*-mass calculation for all events of the two tight sample (see pag. 78 for subsample definition) .

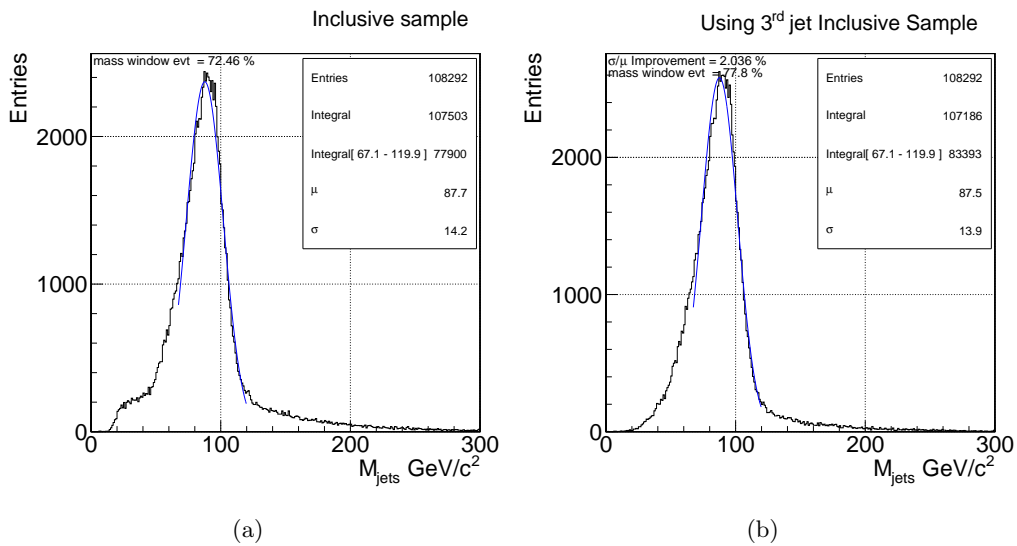
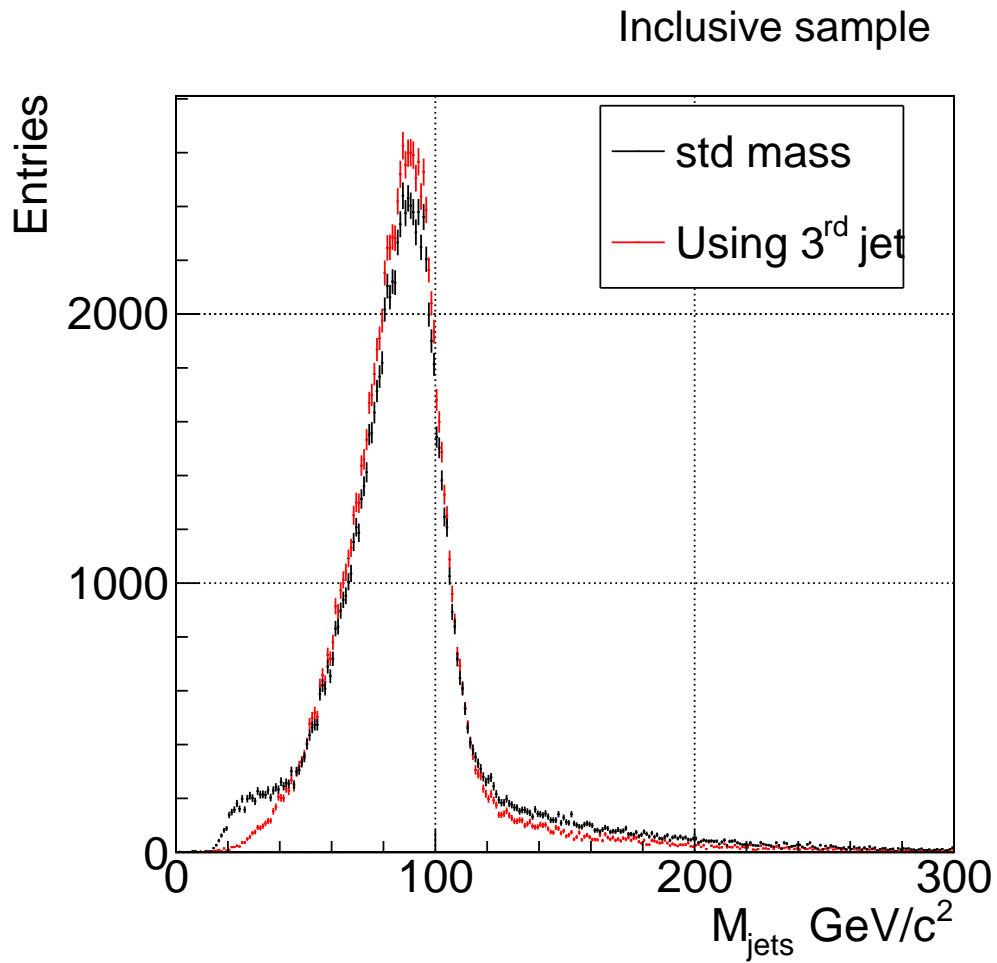


Figure 6.9: Comparison between *std-mass* and *mass* when criteria are applied in the inclusive sample. Figures 6.9(a)–6.9(b) show the fit respectively before and after the correction.

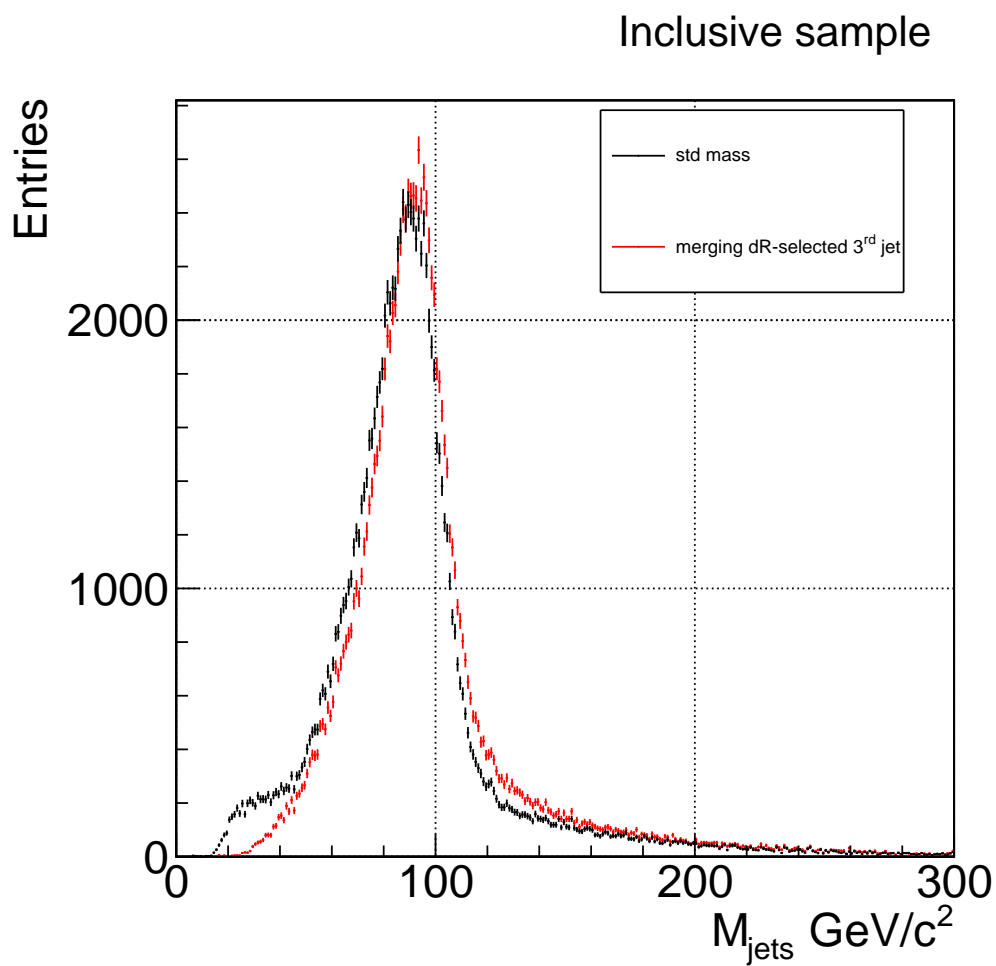


Figure 6.10: Comparison between *std-mass* and mass built using the third jet if two among the three leading jets are within  $dR < 1$

	std reference values	applying criteria
Z-mass	84.4	84.7
Width	19.0	16.5
$\frac{Width}{Z-mass}$	22.56%	19.46%
<b>G</b>		<b>13.74%</b>
<b>Evt/Wind.</b>		<b>12.62%</b>

Table 6.2: Effect of the modified criteria in zone A and B for computing the Z-mass in the *three tight jet sample* as described in the text. The first column gives reference values obtained with a fit to the standard mass definition, the second column gives the results of the fit to the mass corrected merging the third jet. The next to the last line “G” gives the relative decrease of the  $\sigma/\mu$  ratio, and the last line gives the difference in the percentage of events in the selected mass window.

	std reference values	applying criteria
Z-mass	87.7	87.53
Width	14.2	13.92
$\frac{Width}{Z-mass}$	16.24%	15.91%
<b>G</b>		<b>2.04%</b>
<b>Evt/Wind.</b>		<b>5.34%</b>

Table 6.3: Effect of the above criteria applied to the *inclusive sample*. The first column gives values of the *std-mass* fit, the second column gives the results of the fit to the mass corrected including the third jet (merging it in Zone A and substituting second leading jet by the third one in Zone B). The next to the last line “G” gives the relative decrease of the  $\sigma/\mu$  ratio, and the last line gives the difference in the percentage of events within the selected mass window.



## Chapter 7

# Concluding Summary and Future Prospects

In order to improve the invariant mass resolution in reconstructing the Z-mass in the hadron decay channels we studied on a MC sample two different methods:

1. using tracker information to obtain event-specific corrections to calorimeter jet axis and energy;
2. adopting a number of different jet combinations to reconstruct the Z-mass.

Studies based on method 1 predicted a maximum achievable improvement of about 5% (using parton directions as axes of calorimeter jets). However, no progress can be expected when tracker information as available in the real experiment is used. On the other hand jet energy can be sensed by the charge fraction of the jet. An improvement of about 4% can be expected by exploiting this information.

Method 2 is calorimeter-based and opens a new scenario in which one would be able to include in the data sample events not considered previously. According to our studies an improvement of about 14% in mass resolution and of about 13% in signal acceptance can be expected in the sample with three tight jets in the final state (tab. 6.2). In our studies we used  $WZ \rightarrow l\nu q\bar{q}$  MC events only and no background was taken in account so far. Therefore, while pointing at possible important progresses in Z-mass resolution and in signal rate, these studies are leaving important open questions. A check of the methods when applied to the backgrounds processes (mostly  $W + jets$ ) is on-going in order to provide an estimate of  $S/\sqrt{B}$  ratio. The specific jet energy corrections and the multijets analyses will also include studies of the dependence of the mass scale on event topology and on running

conditions<sup>1</sup>.

---

<sup>1</sup>Correcting for the dependence of the mass scale on these parameters is important in the real experiment when a mass peak will be searched in a set of runs performed under different experimental conditions.

# Appendices



## Appendix A

# Some Details on the SM and the Higgs Mechanism

The invariance of classic electrodynamics under the gauge transformation:

$$A_\mu \rightarrow A_\mu - \frac{1}{e} \partial_\mu \alpha(x) \quad (\text{A.1})$$

is recast into QED in terms of group theory. The Lagrangian of a free Dirac particle,

$$\mathcal{L} = \bar{\psi} (i\gamma^\mu \partial_\mu - m) \psi \quad (\text{A.2})$$

is invariant under global U(1) transformations  $\psi \rightarrow e^{-i\alpha} \psi$ . However, it is not invariant under local U(1) transformations  $\psi \rightarrow e^{-i\alpha(x)} \psi$ , where now  $\alpha(x)$  is a function of space-time. By replacing the derivative in eq. (A.1) with the covariant derivative

$$D_\mu = \partial_\mu - ieA_\mu \quad (\text{A.3})$$

where a real field  $A_\mu$  transform as in eq. (A.1), the Lagrangian becomes invariant under U(1) transformations. For completeness a kinetic term is introduced and the final QED Lagrangian is given by:

$$\mathcal{L} = \bar{\psi} (i\gamma^\mu \partial_\mu - m) \psi - \frac{1}{4} F_{\mu\nu}^2 + e\bar{\psi} \gamma^\mu A_\mu \psi \quad (\text{A.4})$$

where the field tensor  $F_{\mu\nu}$  is given by:

$$F_{\mu\nu} = \partial_\mu A_\nu - \partial_\nu A_\mu \quad (\text{A.5})$$

As it can be seen from eq. (A.4) there is a term  $e\bar{\psi}\gamma^\mu A_\mu\psi$  in the Lagrangian that describes the interaction between the charged particles, represented by the wave function  $\psi$  and the gauge field  $A_\mu$ . The existence and properties of the photon follow from the requirement of local gauge invariance under U(1) transformations. The Lagrangian does not contain a mass term for the field  $A_\mu$  (such as  $m^2 A_\mu A^\mu$  that would violate local gauge invariance), and the photon is massless.

The electroweak theory, which unifies the weak and electromagnetic interactions is constructed similarly to QED. The theory of weak interactions was initially developed to explain the properties of the  $\beta$ -decay by E.Fermi in 1934 [7]. In analogy with electromagnetic interactions in QED, such as electron proton scattering, whose amplitude is given by a product of electron and proton currents:

$$\mathcal{M} = (e\bar{u}_p\gamma^\mu u_p)\left(-\frac{1}{q^2}\right)(-e\bar{u}_e\gamma_\mu u_e) \quad (\text{A.6})$$

Fermi proposed a theory of  $\beta$ -decays with similar amplitudes:

$$\mathcal{M} = G_F(\bar{u}_n\gamma^\mu u_p)(\bar{u}_\nu\gamma_\mu u_e) \quad (\text{A.7})$$

for the charged current of weak decays. This model provided a satisfactory description of phenomenology of  $\beta$ -decays, but it was soon evident that it was a low energy approximation, since it predicted an indefinite growth of the cross-sections as the energy increases. After the discovery of parity violation in weak interactions it was realized that the vector-vector interaction term in Fermi's theory had to be modified, by replacing  $\gamma^\mu$  in eq. (A.7), with  $\gamma^\mu(1 - \gamma^5)$  [8, 9]. Indeed, parity was violated maximally, and weak interactions affected only left-handed particles. All the experimental evidence until now suggests that neutrinos interact with lepton only through weak interaction, and therefore are left-handed. The weak interaction term is customarily referred to as the "V-A" structure of weak interactions. The first attempt to incorporate the V-A structure into a gauge theory was made by Bludman in 1958 [10]. His model, based on the SU(2) weak isospin group, required three vector bosons (number of generator of the group) and predicted a neutral massive boson. The detection of neutrino scattering in CERN experiments in 1973 [11] opened a new chapter in particle physics, with the observation of weak neutral currents. The next step of unifying the electromagnetic and weak interactions was

made by Glashow in 1961 [12], when he utilized the gauge group  $SU(2) \otimes U(1)$ .  $U(1)$  was associated to the weak hypercharge  $Y_W$ , related to the weak isospin ( $I$ ) and electric charge ( $Q$ ) through

$$Q = I_3 + \frac{Y_W}{2}.$$

This theory required four gauge bosons: a triplet ( $W_\mu^1, W_\mu^2, W_\mu^3$ ) corresponding to the  $SU(2)$  group, and a neutral field  $B_\mu$  corresponding to  $U(1)$ . Similar to QED, a covariant derivative was introduced:

$$D_\mu = \partial_\mu - ig \frac{\tau_a}{2} W_\mu^a + i \frac{g'}{2} Y_W B_\mu \quad (\text{A.8})$$

where  $g$  and  $g'$  are the coupling constants and  $\tau_a$  are the Pauli spin matrices. As a result, the charged weak current appeared as linear combination of  $W_\mu^1, W_\mu^2$  and the photon and the neutral vector boson  $Z$  as combinations of  $W_\mu^3, B_\mu$ .

$$W_\mu^\pm \equiv \sqrt{\frac{1}{2}} (W_\mu^1 \mp W_\mu^2) \quad (\text{A.9})$$

$$A_\mu \equiv B_\mu \cos \vartheta_W + W_\mu^3 \sin \vartheta_W \quad (\text{A.10})$$

$$Z_\mu \equiv -B_\mu \sin \vartheta_W + W_\mu^3 \cos \vartheta_W \quad (\text{A.11})$$

$$\frac{g'}{g} = \tan \vartheta_W \quad (\text{A.12})$$

the coupling of electromagnetic current to the photon field  $A_\mu$  was given by electrical charge:

$$Q = g \cdot \sin \vartheta_W = g' \cdot \cos \vartheta_W. \quad (\text{A.13})$$

All boson masses in this theory are null. The problem of generating masses without breaking the gauge invariance of the theory was solved by introducing a mechanism for “spontaneous symmetry breaking”, the *Higgs mechanism*.

## A.1 The Higgs Mechanism

Spontaneous breaking of symmetry is based on the possibility, in systems with infinite degrees of freedom, to have a Lagrangian invariant under a group  $G$  of transformation that produces non symmetric states. The Higgs mechanism was proposed by P. Higgs in 1964 [13] and implemented to give masses to  $W$  and  $Z$

bosons by Weinberg and Salam [16, 17] in the  $SU(2) \otimes U(1)$  theory. The simplest example can be given considering a boson interacting with a complex scalar gauge field. The interaction is described by a Lagrangian density of the following form:

$$\mathcal{L} = (D_\mu \Phi)(D^\mu \Phi)^* - \mu^2 \Phi^* \Phi - \lambda (\Phi^* \Phi)^2 - \frac{1}{4} F^{\mu\nu} F_{\mu\nu} \quad (\text{A.14})$$

where the term containing the covariant derivative  $D_\mu$ , eq. (A.8), expresses the interaction between the boson and the gauge field with a coupling  $g$  (similar to the electric charge in eq. (A.3)) and  $F^{\mu\nu}$  is defined in eq. (A.5). Equation (A.14) maintains invariance under the local gauge transformation. The parameter  $\mu^2$  and  $\lambda > 0$  in the potential part  $V(\Phi) = \mu^2 \Phi^* \Phi + \lambda (\Phi^* \Phi)^2$  lead to a potential bounded from below. Figure A.1 shows the potential  $V(\Phi)$  for  $\mu^2 > 0$ , where only one minimum is present, and  $\mu^2 < 0$ , where there are two minima. The case of one minimum is applicable to a particle with mass  $\mu$ . It is qualitatively different from the case of two minima. The two minima of the potential are

$$\Phi = \pm v = \pm \sqrt{-\frac{\mu^2}{\lambda}} \quad (\text{A.15})$$

The solution of the equation of motion corresponds to the minimal energy solution, i.e. to the *vacuum expectation values* of the fields in lowest order perturbation theory (eq. (A.15)).

We must choose a stable minimum, or ground state, for a perturbative expansion. Shifting the theory to a non-zero ground state changes the properties of the potential, namely, it has removed the symmetry about the  $V(\Phi)$  axis<sup>1</sup>. We say the ground state “*breaks the symmetry*” since it no longer shares the symmetry of the full theory. The choice of ground state is arbitrary, and we select the ground state  $+v$ . The original  $\Phi(x)$  field can be expressed by new real fields,  $\xi$  and  $h$ , with zero vacuum expectation values, as in:

$$\Phi(x) = \frac{\exp i\xi/v}{\sqrt{2}} (v + h(x)). \quad (\text{A.16})$$

By choosing a gauge with  $\xi = 0$  we get

$$\begin{aligned} \mathcal{L} &= \frac{1}{2} (\partial_\mu - igA_\mu)(v + h)(\partial^\mu + igA^\mu)(v + h) - \frac{\mu^2}{2} (v + h)^2 - \frac{\lambda}{4} (v + h)^4 - \frac{1}{4} F_{\mu\nu}^{\mu\nu} \\ &= \frac{1}{2} (\partial_\mu h)(\partial^\mu h) + \mu^2 h^2 + \frac{(gv)^2}{2} A^\mu A_\mu + g^2 v h A^\mu A_\mu + \dots \end{aligned} \quad (\text{A.17})$$

---

<sup>1</sup>The perturbative expansion does not change the physics of the full process. If we took our expansion to high enough order, it would still have the symmetries of the full theory. Only the lower-orders description of the ground state has changed.

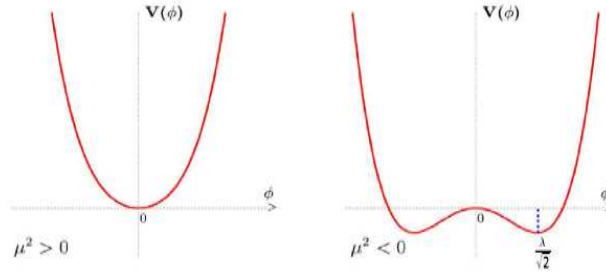


Figure A.1: *Symmetry breaking depending on the  $\mu^2$  parameter:  $\mu^2 > 0$  on the left,  $\mu^2 < 0$  on the right.*

Interpreting the individual terms in the Lagrangian density  $\mathcal{L}$  one finds that the theory contains:

- a mass term for the gauge boson  $M = gv$ ,
- a neutral scalar boson  $h$  (a real field) with a mass  $M_H = \sqrt{-2\mu^2}$ ,
- the interaction terms  $gM h A^\mu A_\mu$  with the coupling proportional to the mass of the gauge boson,
- the self interaction terms  $hhh, hhhh$  etc.

When spontaneous symmetry breaking takes place in eq. (A.17), the initial complex scalar field (two degrees of freedom) and the massless vector field (other two degrees of freedom for the helicity states) turns into a scalar real (neutral) particle (one degree of freedom) and a massive charged vector boson (three degrees of freedom).

By measuring the gauge boson mass one can determine the parameter  $v$ , provided there is independent constraint on the coupling  $g$ :

$$M = gv \tag{A.18}$$

The second term in eq. (A.17) predicts a scalar particle, with mass  $M_H = \sqrt{-2\mu^2}$ , which is called Higgs boson. However, for knowing the mass of the Higgs boson we should know the self interaction, i.e. parameter  $\lambda$ , since

$$M_H = \sqrt{2\lambda}v. \quad (\text{A.19})$$

### A.1.1 Spontaneous Symmetry Breaking in SM

We have seen that a perturbative expansion of the Lagrangian about its symmetry-broken ground state reveals mass terms for our gauge bosons and scalars. Symmetry breaking in the SM is similar to the example given above for a single complex scalar field, with the difference that two complex scalar fields are introduced now to adapt the Higgs mechanism to the gauge groups  $SU(2) \otimes U(1)$ . The details can be found in [2]. The process results in three massive gauge bosons ( $W^\pm$ ,  $Z$ ), a massless photon, a new massive electrically neutral scalar Higgs boson ( $H$ ), and a set of massive fermions<sup>2</sup>. The mass terms for the particles are

$$M_W = \frac{1}{2}vg \quad (\text{A.20})$$

$$M_Z = \frac{1}{2}v\sqrt{g^2 + g'^2} \quad (\text{A.21})$$

$$\frac{M_W}{M_Z} = \cos \vartheta_W \quad (\text{A.22})$$

$$M_f = \frac{y_f v}{2} \quad (\text{A.23})$$

$$M_h = \sqrt{2\lambda}v \quad (\text{A.24})$$

where  $v = 246$  GeV is the vacuum expectation value of the Higgs field,  $g(g')$  is the known strength of the charged (neutral) current interaction,  $\lambda$  is a free term in the scalar potential, and  $y_f$  is the Yukawa coupling of each fermion to the Higgs field. The couplings  $y_f$  and  $\lambda$  are free parameters in the theory that must be fixed by experimental inputs. As mentioned above, in 1973 the Gargamelle collaboration at CERN performed the first measurement of neutrino-induced weak neutral current interactions. From the measurement of the ratio of Neutral Currents (NC) to Charged Currents (CC) [11] it was found that at 90% C.L.

$$0.1 < \sin^2 \vartheta_W < 0.6 \quad (\text{A.25})$$

---

<sup>2</sup>Neutrinos are assumed to be massless. Recent neutrino experiments have shown that neutrinos do have mass [5], but its origin is not clear.

From low-energy phenomenology one can obtain a relation [2]

$$\frac{g}{2\sqrt{2}} = \sqrt{\frac{M_W^2 G_F}{\sqrt{2}}} \quad (\text{A.26})$$

which together with A.13 provided an estimate of the mass of the W and Z bosons:

$$M_W^2 = \frac{Q^2}{4 \sin^2 \vartheta_W} v^2 \approx \left( \frac{37.2}{\sin \vartheta_W} \text{GeV} \right)^2 \sim (48 - 118 \text{GeV})^2 \quad (\text{A.27})$$

and a similar relation may be obtained for  $M_Z$  :

$$M_Z^2 \approx \left( \frac{37.2}{\sin \vartheta_W \cos \vartheta_W} \text{GeV} \right)^2 \sim (76 - 124 \text{GeV})^2 \quad (\text{A.28})$$

In 1983, at the CERN SPS  $p\bar{p}$  collider, both Z and W [18] bosons were discovered. Their masses were determined with a precision of a few GeV as shown in tab. A.1.1, in a good agreement with SM predictions. Currently (year 2009) the most precise measurements are  $\sin^2 \vartheta_W = 0.23119 \pm 0.00014$ ,  $M_W = 80.40 \pm 0.03$  and  $M_Z = 91.188 \pm 0.002$  [5].

	UA1	UA2	Current Value
$M_W$	$83.5 \pm 1.1 \pm 2.7$	$80.2 \pm 0.6 \pm 0.5$	$80.40 \pm 0.03$
$M_Z$	$93.0 \pm 1.4 \pm 3.0$	$91.5 \pm 1.2 \pm 1.7$	$91.188 \pm 0.002$

Table A.1: *Masses of the W and Z bosons as measured by UA1 and UA2 experiments, and their more precise current values [5].*

## A.2 Quantum Chromodynamics

The theory describing the interactions of quarks and gluons is called Quantum Chromodynamics. After the discovery of the neutron, around 1932, it was realized that the forces keeping nucleons in nuclei together must be attractive at short distance and much stronger than the electromagnetic forces. The first theoretical model of strong interactions was constructed by Yukawa around 1935 [19]. Yukawa assumed that the interactions of nucleons is mediated by a new force, whose quanta, the mesons, would be new type of particles. Since the strong interaction is felt only over a short-range, the force carriers, "mesons", would be massive with a mass  $\sim 200$  MeV . Another important characteristic was the large meson-nucleon coupling. The muon discovered in cosmic rays with a mass close to that predicted

for the Yukawa meson was considered as a confirmation of the Yukawa theory. The misinterpretation was later removed when the pion was discovered, who was a better candidate are carrier of the strong force. However, many other mesons and baryons were discovered after the pion discovery, proving that the picture was much more complex. It was found that all known hadrons can be grouped into groups of octets and decuplets that can be represented as multiplets of  $SU(3)$ . The theory was confirmed with the observations of the  $\Omega^-$ -hyperon, which was predicted by the theory. The theory introduced quarks, belonging to the fundamental representation of  $SU(3)$ . This was the foundation of the quark model of hadrons. In this theory, mesons were formed as a bound state of a quark and anti-quark, while the baryons consist of three quarks. Fermions were assigned fractional electric charge:  $Q_u = 2/3$  and  $Q_d = -1/3$ . The quark model was very successful in describing the known properties of particles and in making predictions. However, the dynamics of the strong force was not clear. It was not understood why the quarks are only in bound states, and many attempts to detect free fractional charges were unsuccessful. Another difficulty arose from the observations of  $\Delta^{++}$ , which according to the quark model should contain 3 u-quarks in the same quantum state. Since two fermions cannot occupy the same quantum state, according to the Pauli's principle, a new quantum number called *color* was introduced. It was postulated that only colorless states are allowed, hence quarks are "confined" within hadrons. The color states are conventionally referred to as Red ( $R$ ), Green ( $G$ ) and Blue ( $B$ ). The relativistic quantum field theory of strong interactions was constructed using the  $SU(3)$  group, in a similar fashion to that of weak interactions. The force carriers in QCD are massless gluons. Due to non-Abelian nature of the transformation group, the gluons are self-interacting, which means that gluons can also carry color charge. A breakthrough occurred when the charge renormalization was calculated by Gross, Wilczek and Politzer and the phenomenon of *asymptotic freedom* was discovered [20, 21]. This allowed to make QCD a self-consistent theory. It also allowed to explain why the strong interactions are strong: if the coupling falls off at small distances it must grow at large distances reaching  $\sim 1$  at scales about 1 fm. The quark mass eigenstates are not the same as the weak eigenstates. The transformation from one eigenstate to another is performed using the Cabibbo-Kobayashi-Maskawa (CKM) matrix. The matrix is not diagonal, allowing mixing of quark flavors. The current most precise values of the CKM matrix are presented

in eq. (A.29) [5]

$$\begin{pmatrix} d' \\ s' \\ b' \end{pmatrix} = \begin{pmatrix} |V_{ud}| \approx 0.974 & |V_{us}| \approx 0.23 & |V_{ub}| \approx 0.004 \\ |V_{cd}| \approx 0.230 & |V_{cs}| \approx 1.04 & |V_{cb}| \approx 0.04 \\ |V_{td}| \approx 0.008 & |V_{ts}| \approx 0.04 & |V_{tb}| > 0.74 \end{pmatrix} \times \begin{pmatrix} d \\ s \\ b \end{pmatrix} \quad (\text{A.29})$$

The 9 elements of the CKM matrix can be written in terms of 4 parameters, which need to be determined from experiments:  $V_{CKM} = R_1(\vartheta_{23})R_2(\vartheta_{13}, \delta_{13})R_3(\vartheta_{12})$ . The  $R_i(\vartheta_{jk})$  are rotational matrices around the axis  $i$ , the angle  $\vartheta_{jk}$  describes the mixing of the generations  $j$  and  $k$  and  $\delta_{13}$  is a phase. For three generations the CKM matrix does not have to be real, i.e. the phase  $\delta_{13}$  does not have to be zero. This non-zero phase explains the  $CP$  violation in weak interactions. Overall, the Standard Model of particle physics contains close to 20 free parameters, which need to be determined from experiments. These are the lepton and quark masses, 4 independent parameters of the CKM matrix, the gauge couplings of  $U(1)$ ,  $SU(2)$  and  $SU(3)$ , and the Higgs quadratic coupling  $\mu$  and the Higgs couplings.



## Appendix B

# Collision Energy and Luminosity

The collision energy determines the accessible phase-space for the particle production in the final state. The luminosity is the coefficient of proportionality between the rate of a given process and its cross-section  $\sigma$ :

$$\frac{dN}{dt} [\text{events s}^{-1}] = \mathcal{L} [\text{cm}^{-2}\text{s}^{-1}] \times \sigma [\text{cm}^2].$$

The time-integral of the luminosity (integrated luminosity) allows to compute the expected number of events,  $N$ , produced in a finite time  $T$ :

$$N(T) = \int_0^T \mathcal{L} \sigma dt.$$

Assuming an head-on collision with zero crossing angle between the beams, the instantaneous luminosity is defined as:

$$\mathcal{L} = 10^{-5} \frac{N_p N_{\bar{p}} B f \beta \gamma}{2\pi \beta^* \sqrt{(\varepsilon_p + \varepsilon_{\bar{p}})_x (\varepsilon_p + \varepsilon_{\bar{p}})_y}} F(\sigma_z / \beta^*) \quad [10^{30} \text{cm}^{-2} \text{s}^{-1}]$$

The luminosity depends on the average numbers of protons (antiprotons) in each bunch (typically  $N_p \approx 2.8 \cdot 10^{12}$  and  $N_{\bar{p}} \approx 8.3 \cdot 10^{11}$  at Tevatron), the number of circulating *bunches* in the ring ( $B = 36$ ), the revolution frequency  $f$  (47.713 kHz), the Lorentz relativistic factor  $\beta\gamma$  (*boost*,  $\beta\gamma = 1045.8$  at 980 GeV), an empiric factor  $F$  which is a function of the ratio between the longitudinal r.m.s. width of the bunch ( $\sigma_z$ ) and the “beta function”  $\beta^*$  calculated at the interaction point ( $\beta^* \approx 31$  cm), and the 95% normalized emittances of the beams  $\varepsilon_p$  ( $\varepsilon_{\bar{p}}$ ) ( $\varepsilon_p \approx 18\pi$  mm mrad e

$$\varepsilon_{\bar{p}} \approx 13\pi \text{ mm mrad) [37].}^1$$

---

<sup>1</sup>The  $F$  factor is a parameterization of the longitudinal profile of the beams in the collision region, which assumes the shape of an horizontal hourglass centered in the interaction region. The beta function is a parameter used to describe approximately the trajectory of a particle through an arbitrary beam transport system. The emittance  $\varepsilon$  measures the phase-space occupied by the particles of the bunches. The quantity  $\sqrt{\beta\varepsilon}$  is proportional to the r.m.s. width of the beam in the phase plane.

## Appendix C

# Tevatron Collider Operation

### C.1 Proton Production

Protons are produced from gaseous hydrogen  $H_2$ , which is negatively ionized to allow an essentially loss-free acceleration to 750 kV Cockcroft-Walton DC accelerator. Negative  $H^-$  ions are produced in two steps: first the  $H_2$  molecule is broken and the electrons are stripped away from the hydrogen atom by an electric field. These protons are then collected on a negatively charged Cs-doped metal surface, where they are linked to two free electrons.  $H^-$  ions are kicked away by other incoming protons and moved away from the metal surface because of their like-sign charge.

750 keV  $H^-$  ions are then accelerated up to 400 MeV by a 130 m long Alvarez type linear accelerator (*Linac*, fig. 2.1). The  $H^-$  beam pulse lasts typically 20 ms and is injected into a booster synchrotron. When entering the booster,  $H^-$  ions pass through a carbon foil where the two electrons are removed. The booster has a circumference of 475 m and accelerates protons from 400 MeV to 8 GeV.

Injecting  $H^-$  ions rather than protons into the booster allows the injection to proceed over multiple revolutions of the beam around the booster ring (usually 10–12). If protons were instead injected, the magnetic field used to inject new protons onto orbit in the booster would also deflect out the already revolving protons out of orbit.

### C.2 Antiproton Production and Accumulation

Protons exiting the booster with a momentum of 8 GeV are transferred to the Main Injector. This synchrotron was built as an upgrade of the Fermilab accelerator

chain that took place between 1998 and 2002 to achieve better Tevatron performances in Run II. The Main Injector replaced the Main Ring, an older synchrotron of similar energy which was housed in the Tevatron tunnel. The Main Injector carries more current with faster cycling rate than the Main Ring, leading to a higher luminosity of the Tevatron Collider. The radiofrequency bunched proton beam is extracted from the Main Injector at 120 GeV and brought to collide against a 7 cm thick nickel target, where many secondary particles, including antiprotons, are produced. The produced particles are focussed by a lithium lens and analyzed in a magnetic spectrometer selecting negatively charged particles. Antiprotons are produced over a wide momentum range, with a broad maximum around 8 GeV and an efficiency of about  $2 \cdot 10^{-5}$  per interacting proton<sup>1</sup>. The bunched antiproton beam is accepted with a momentum spread of about 2.5% by a “debuncher” synchrotron (see fig. 2.1) where, by radiofrequency manipulation, it is turned into a continuous nearly monochromatic 8 GeV beam. The  $\bar{p}$  debunched beam is transferred to the Accumulator Ring, housed in the same tunnel of the debuncher, which collects pulses from the debuncher over a long period of time, usually many hours. In the accumulator a higher intensity antiproton beam is stored, as much as allowed by its larger acceptance. In both the debuncher and the accumulator the longitudinal and transverse momentum spread of the beam is reduced (“cooled”) by stochastic cooling<sup>2</sup>. Since 2004, optimized antiproton accumulation is achieved using the Recycler Ring (see fig. 2.1). This is a constant 8 GeV-energy storage-ring placed in the Main Injector enclosure, that uses permanent magnets (magnetized strontium ferrite). It is used to gather antiprotons that are periodically transferred from the Accumulator (with  $\sim 95\%$  transfer efficiency) thus maintaining it at its optimum intensity regime. Recently, relativistic electron cooling was successfully implemented in the Recycler, further enhancing the Tevatron performance [35].<sup>3</sup>

---

<sup>1</sup>Typically, 21 antiprotons are collected for each 106 protons on target, resulting in a stacking rate of approximately 10–20 mA/h

<sup>2</sup>Stochastic cooling is a technique used to reduce the transverse momentum and energy spread of a beam without beam loss. This is achieved by applying iteratively a feedback mechanism that senses the beam deviation from the ideal orbit with electrostatic plates, processes and amplifies it, and transmits an adequately-sized synchronized correction pulse to another set of plates downstream [34]. Bunch rotation is an RF manipulation technique that, using adequate phasing, transforms a beam with a large time spread and a small energy spread in a beam with a large energy spread and a small time spread, or viceversa.

<sup>3</sup>Electron cooling is a method of damping the transverse motion of the antiproton beam through the interaction with an electron beam propagating together at the same average velocity.

## C.3 Injection and Collisions

Every some 10–20 h, antiproton accumulation is stopped in preparation for injection. A set of seven proton bunches is extracted from the booster, injected into the Main Injector, accelerated to 150 GeV, coalesced with  $\approx 90\%$  efficiency into a single bunch of  $\approx 3 \times 10^{12}$  p, and then injected into the Tevatron.<sup>4</sup> This process is repeated every 12.5 seconds, until 36 proton bunches, separated by 396 ns, are loaded into the Tevatron central orbit<sup>5</sup>. Typically, 65% of the protons in the Main Injector are successfully transferred to the Tevatron. The electrostatics separators (about 30 pairs of metal plates) are then activated in the Tevatron, in preparation for antiproton injection.

Four sets of 7–11  $\bar{p}$  bunches are extracted from the Accumulator (or from the Recycler) to the Main Injector, accelerated to 150 GeV, coalesced with  $\approx 80\%$  efficiency into four  $8 \times 10^{11}$   $\bar{p}$  bunches separated by 396 ns, and then injected into the Tevatron, where protons are counter-rotating. Protons and antiprotons circulate in the same enclosure, sharing magnet and vacuum systems. The injection process is repeated nine times until 36 antiproton bunches circulate in the Tevatron.

The beam is then accelerated in about a minute from 150 to 980 GeV, at which energy one particle completes the full revolution of the Tevatron circumference in 21  $\mu\text{s}$  at  $0.9999996c$ . The beams are finally brought into collision at the two instrumented interaction-points located along two straight sections of the Tevatron: D $\emptyset$  and B $\emptyset$ , where the D $\emptyset$  and CDF II detectors, respectively, are located. Special high-power quadrupole magnets (“low- $\beta$  squeezers”), installed on the beam pipe at either side of the detectors, reduce the transverse spatial spread of the beams to maximize the collision rate in the interaction regions. The resulting transverse spatial distribution of the luminous region is approximately a two-dimensional Gaussian, with  $\sigma_T \approx 30 \mu\text{m}$ . The typical longitudinal dimension of a bunch is 60–70 cm. The interaction regions have a roughly Gaussian distribution along the beam direction, with r.m.s. width  $\sigma_z \approx 28 \text{ cm}$ .<sup>6</sup>

<sup>4</sup>Coalescing is the process of compacting into one dense bunch many smaller bunches.

<sup>5</sup>Currently (as of 2002), the Tevatron is running at a center-of-mass energy of 1.96 TeV with an inter bunch-crossing time of 396 ns. The original plan of shortening the inter bunch-crossing to 132 ns, to reduce pile-up events, has been abandoned. Antiprotons are accumulated at  $\approx 10^{11} \bar{p}/\text{h}$  rates and transferred through the accelerator chain with average 75% overall efficiency for the next store.

<sup>6</sup>Whereas one may expect a bunch length  $\sigma_z \approx 60 \text{ cm}$  to distribute  $p\bar{p}$  interactions over a length of  $60/\sqrt{2} \text{ cm}$ , this length is in fact less than 30 cm owing to the variation of the transverse beam profile along the beam ( $z$ ) axis.

The number of overlapping inelastic interactions  $N$  for each bunch crossing is a Poisson-distributed variable that depends on the instantaneous luminosity. The observed distribution of the multiplicity of interaction vertices yields  $\bar{N} \approx 0.2, 1.0, 2.0,$  and  $6.0$  for respectively,  $\mathcal{L} \approx 1 \times 10^{31}, 5 \times 10^{31}, 10 \times 10^{31},$  and  $30 \times 10^{31}$  luminosities. The luminosity decreases as a function of time because of the interactions of the beam with residual molecules of gas in the beam pipe, beam-halo interactions, and to a lesser extent of  $\bar{p}$  depletion due to the collisions. During the 10–20 h of a store, the luminosity decreases by a factor of 2.5–5, the majority of data being collected at  $\mathcal{L} \approx \mathcal{L}_0/2$ . After injection, a new antiproton accumulation cycle is started. When the antiproton stack is sufficiently large and the colliding beams are degraded, the detector supply-voltages are switched-off and the store is dumped. The beam is extracted via a switch-yard and sent to an absorption zone.

Beam abortion can occur also accidentally when a superconducting magnet rises its temperature above the critical value (i. e., the magnet “quenches”), destroying the orbit of the beams.<sup>7</sup> The time between the end of a store and the beginning of collisions of the next one is typically 2 h, during which time calibrations of the subdetectors and cosmic rays tests are usually performed.

## C.4 Tevatron Performance

Since the beginning of Run II the Tevatron performance has been steadily improving. The Tevatron set the world record of highest peak luminosity for a hadron collider of  $3.47 \times 10^{32} \text{ cm}^{-2}\text{s}^{-1}$  (April 2009). As of September 2009, physics quality data corresponding to  $\sim 6\text{fb}^{-1}$  are stored on permanent memories (see fig. C.1) and  $8-9\text{fb}^{-1}$  are expected by the end of 2010. The main features of Tevatron in history are listed in tab. C.1. Further details can be found in [32].

---

<sup>7</sup>During a quench, one cubic liter of liquid helium expands to 700 cubic liters of gaseous helium within a quarter of a second. More than 1500 custom-made relief valves allow the Tevatron cryogenic system to manage the rapid expansion.

Run	RunIb	RunII	RunIIa	RunIIb
p bunches $\times$ $\bar{p}$ bunches	6 $\times$ 6	36 $\times$ 36	140 $\times$ 103	140 $\times$ 103
p/bunch	$2.3 \cdot 10^{11}$	$2.78 \cdot 10^{12}$	$2.7 \cdot 10^{11}$	$2.7 \cdot 10^{11}$
$\bar{p}$ /bunch	$5.5 \cdot 10^{10}$	$8.33 \cdot 10^{11}$	$4.0 \cdot 10^{10}$	$1.0 \cdot 10^{11}$
Total antiprotons	$3.3 \cdot 10^{11}$	$3.3 \cdot 10^{12}$	$4.2 \cdot 10^{12}$	$1.1 \cdot 10^{13}$
$\bar{p}$ production rate ( $hr^{-1}$ )	$6.0 \cdot 10^{10}$	$2.2 \cdot 10^{11}$	$2.1 \cdot 10^{11}$	$5.2 \cdot 10^{11}$
p emittance (mm $\cdot$ mrad)	23 $\pi$	18 $\pi$	20 $\pi$	20 $\pi$
$\bar{p}$ emittance (mm $\cdot$ mrad)	13 $\pi$	13 $\pi$	15 $\pi$	15 $\pi$
$\beta^*$ (cm)	35	31	35	35
$\sqrt{s}$ (GeV)	1.8	1.96	1.96	1.96
Bunch length RMS (m)	0.60	0.37	0.37	0.37
Crossing angle ( $\mu$ rad)	0	0	136	136
Design $\mathcal{L}$ ( $cm^{-2}s^{-1}$ )	$0.16 \cdot 10^{31}$	$0.86 \cdot 10^{32}$	$2.1 \cdot 10^{32}$	$5.2 \cdot 10^{32}$
$\int \mathcal{L}dt$ ( $pb^{-1}/week$ )	3.2	50.3	42	105
Bunch spacing (ns)	$\sim 3500$	396	132	132
Interaction/crossing	2.5	2.3	1.9	4.8

Table C.1: Main Tevatron performance parameter since 1993. In the current Run II the number of bunches has been reset to 36 $\times$ 36 and the increase of luminosity has been obtained by improving the antiproton storage.

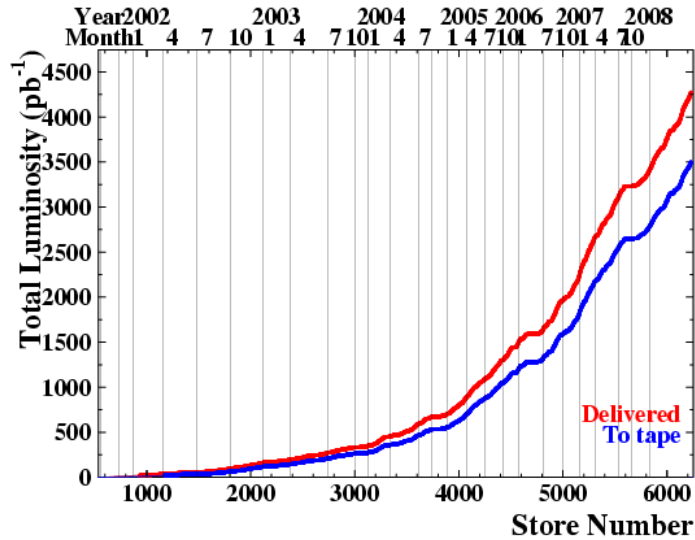


Figure C.1: Total integrated luminosity in Run II up to spring 2009. Red line is the total luminosity produced, blue line the registered one on hard disks.



# Appendix D

## Other CDF II Sub-Detectors

### D.1 Time-of-Flight Detector

Between the COT and the solenoid a layer of 1.4 m inner radius scintillator bars measures the track time of flight (TOF) from the collision point [39],[44]. TOF information can be combined with  $\left(\frac{dE}{dx}\right)$  to separate pions from kaons up to a momentum of about 1.5 GeV. This information is particularly important in high precision B-physics<sup>1</sup>

The TOF detector is composed by 216 scintillator bars, with a slightly trapezoidal cross-section of 4 cm maximum basis, 4 cm thickness and 2.79 m length. Light is collected by photomultipliers at the ends of the bars. Single hit position along the scintillator bars is determined by the comparing the timing of the photomultiplier signals. The TOF time resolution is  $\approx 120$  ps. Figure D.1 shows the CDF pion/kaon/proton separation power by the combined  $\left(\frac{dE}{dx}\right)$  and TOF measurements. For the TOF measurement the collision time  $t_0$  must be known. This is found with a  $\sim 50$  ps uncertainty by a best-fit process over all tracks in the event.

### D.2 Muon Detectors

The tracker, the magnet return yoke, the calorimeter, and additional steel shielding act as muon filters: they absorb electromagnetic and hadronically interacting particles thus allowing detecting the more penetrating muons in multiple layers of drift

---

<sup>1</sup>The particle mass can be derived as  $m = \frac{p}{c} \sqrt{\frac{c^2 t^2}{L^2} - 1}$ , where the momentum  $p$  and the path length  $L$  are precisely measured by the tracking system.

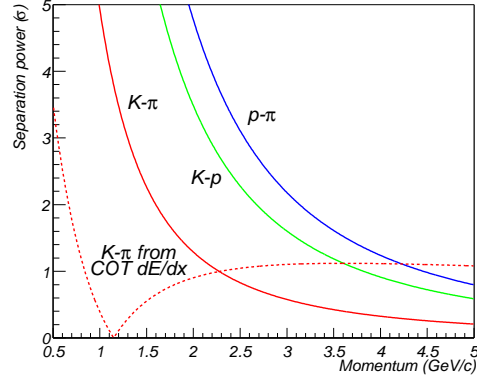


Figure D.1: Particle separation power of the TOF detector (comparison with COT  $dE/dx$  is shown too).

chambers placed on the outermost shell of the detector. Four independent systems detect penetrating charged particles at the  $|\eta_{\text{det}}| \lesssim 1.5$ , employing combinations of drift tubes, scintillation counters, and absorbers with different azimuthal coverages [50]. Table D.1 shows the most relevant design parameters of these detectors. Single wire, rectangular drift chambers are arranged in arrays with various azimuthal segmentations and coupled with scintillator counters. The chambers, filled with a 50:50 admixture of argon and ethane, have sense wires parallel to the beam axis and operate in proportional regime. In each azimuthal sector, stacks of up to eight layers of chambers are overlaid along the radial direction to allow coincidences among layer hits. The chambers are staggered in various patterns of alternating cells, for azimuthal ambiguity resolution. The difference of the drift electrons arrival-times between neighboring staggered cells provides up to  $250 \mu\text{m}$  hit-position resolution in the  $(r, \varphi)$  view. Division of the charge collected at the opposite ends of sense wires allows a measurement of the  $z$  coordinate of the hit with up to  $1.2 \text{ mm}$  resolution, as measured with energetic cosmic muons traversing the detector. Scintillators provide timing information to suppress backgrounds due to secondary interactions in the beam pipe material and to cosmic rays. Timing also allows association of cell hits to the appropriate bunch-crossing, since the maximum drift time in the chambers (see tab. D.1) exceeds the inter bunch-crossing time. When a short track-segment (*stub*), resulting from three matching radial layers, corresponds to the outward extrapolation of a COT track, a muon candidate is identified and associated to the corresponding momentum measured in the tracker.

The Central MUon detector (CMU) is located around the outside of the central

hadron calorimeter at a radius of 347 cm from the beam axis and covers the region  $0.03 \lesssim |\eta_{\text{det}}| \lesssim 0.63$ . Each array covers  $12.6^\circ$  in  $\varphi$ , while a  $2.4^\circ$  gap between arrays limits the azimuthal coverage to 84% of the full angle. Each array is further segmented azimuthally into three  $4.2^\circ$  modules.

The Central Muon uPgrade (CMP) is a second set of drift chambers located behind an additional 60 cm of steel and arranged to enclose the central detector within an approximately rectangular box. Its function is to cover the  $\varphi$  gaps of the CMU, and to enhance rejection of penetrating high energy hadrons, which are limited to a measured fraction of 1% of the total pions and 2–4% of the total kaons. Owing to the common CMU and CMP coverage, only one set of scintillators is used for both. The  $z$  coordinate is measured only in the CMU.

At a radial distance of 400–600 cm from the beam axis, an arrangement of drift-cells and scintillation counters shaped as a conical surface around the beam, the Central Muon eXtension (CMX), extends the muon coverage to the  $0.6 \lesssim |\eta_{\text{det}}| \lesssim 1$  region.

Coverage in the region  $1 \lesssim |\eta_{\text{det}}| \lesssim 1.5$  is completed by the Intermediate MUon system (IMU). Each cell-stack spans  $1.25^\circ$  in  $\varphi$  although its azimuthal coverage is limited by the presence of support structures (see tab. D.1).

Parameter	CMU	CMP	CMX	IMU	Units
Polar coverage	$ \eta_{\text{det}}  \lesssim 0.6$	$ \eta_{\text{det}}  \lesssim 0.6$	$0.6 \lesssim  \eta_{\text{det}}  \lesssim 1.0$	$1 \lesssim  \eta_{\text{det}}  \lesssim 1.5$	–
Azimuthal coverage	$302^\circ$	$360^\circ$	$360^\circ$	$270^\circ$	Degrees
Maximum drift time	800	1,400	1,400	800	ns
Number of channels	2,304	1,076	2,208	1,728	–
Pion interaction-length	5.5	7.8	6.2	6.2–20.0	$\lambda_{\text{int}}$
Minimum $p_T(\mu)$	1.4	2.2	1.4	1.4–2.0	GeV/ $c$

Table D.1: *Design parameters of the muon detectors. The traversed material in units of pion interaction lengths is quoted at  $\vartheta = 90^\circ$  in CMU and CMP, and  $\vartheta = 55^\circ$  in CMX.*

### D.3 Cherenkov Luminosity Counters

The luminosity ( $\mathcal{L}$ ) is inferred from the average number of inelastic interactions per bunch crossing ( $\bar{N}$ ) according to  $\bar{N} \times f_{\text{b.c.}} = \sigma_{\text{p}\bar{\text{p}}-\text{in.}} \times \varepsilon \times \mathcal{L}$ , where the bunch-crossing frequency ( $f_{\text{b.c.}}$ ) is precisely known from the frequency of the Tevatron acceleration

cavities,  $\sigma_{p\bar{p}\text{-in.}} = 59.3 \pm 2.3$  mb is the inelastic  $p\bar{p}$  cross-section resulting from the averaged CDF and E811 luminosity-independent measurements at  $\sqrt{s} = 1.8$  TeV [51], and extrapolated to  $\sqrt{s} = 1.96$  TeV, and  $\varepsilon$  is the efficiency for detecting an inelastic scattering within the forward region covered by the luminosity monitors.

The Cherenkov Luminosity Counters (CLC) are two separate modules, covering the  $3.7 \lesssim |\eta_{\text{det}}| \lesssim 4.7$  range symmetrically in the forward and backward regions [52]. Each module consists of 48 thin, 110–180 cm long, conical, isobutane-filled multicell Cherenkov counters. They are arranged around the beam-pipe in three concentric layers split into azimuthal cell pointing to the nominal interaction region. The base of each cone, 6–8 cm in diameter and located at the furthest extremity from the interaction region, contains a conical mirror that collects the light into a PMT. Isobutane guarantees high refraction index and good transparency for ultraviolet photons. With a Cherenkov angle  $\vartheta_C = 3.4^\circ$ , the momentum thresholds for light emission are 9.3 MeV/ $c$  for electrons and 2.6 GeV/ $c$  for charged pions. Prompt charged particles from the  $p\bar{p}$  interaction are likely to traverse the full counter length, thus generating large signals and allowing discrimination from the smaller signals of angled particles due to the beam halo or to secondary interactions. In addition, the signal amplitude distribution shows distinct peaks for different particle multiplicities entering the counters. This allows a measurement of  $\bar{N}$  with 4.4% relative uncertainty in the luminosity range  $10^{31} \lesssim \mathcal{L} \lesssim 10^{32}$  cm<sup>-2</sup>s<sup>-1</sup>. This accuracy, combined with the 4% relative uncertainty on the inelastic  $p\bar{p}$  cross-section, results in an instantaneous luminosity measured with 5.9% relative uncertainty. This uncertainty only affects the results of analysis where absolute cross sections are measured.

## D.4 Forward Detectors and Beam Monitoring

A set of forward detectors, not shown in previous figures, are used for the measurement of diffractive processes at small angle and for monitoring beam losses. Their location is outside the CDF calorimeters, at different distances up to 57 m from the origin of the interaction region.

Two small, cylindrical calorimeters occupy the radial range  $6 \lesssim r \lesssim 33$  cm in the region  $580 \lesssim |z| \lesssim 640$  cm. They employ lead plates immersed in radiation-resistant liquid scintillator with a tower-less, homogeneous geometry suited for diffractive physics measurements [53].

The furthestmost ( $z \approx -57$  m) components from the interaction point are scintillating fibers placed in the Tevatron vacuum inside retractable “Roman Pots”, which are used as spectrometer for leading antiprotons in measurements of diffractive physics.

Finally, arrays of scintillation counters and ionization chambers are placed along the beam line at varying distances from the interaction point to monitor the beam halo and losses [54].



# Appendix E

## Trigger Levels

### E.1 Level-1

At Level-1, a synchronous system of custom-designed hardware processes a simplified subset of data in three parallel streams to reconstruct coarse information from the calorimeters (total transverse energy and single towers over threshold), from the COT (two-dimensional tracks in the transverse plane), and from the muon system (muon stubs in the CMU, CMX, and CMP chambers). The COT generates also a specially important signal, the eXtreme Fast Tracker (XFT), from a powerful parallel pattern recognition algorithm feedings raw tracking information to L2 trigger. A decision stage combines the informations from these low-resolution physics objects, called “primitives”, into more sophisticated objects, e. g., track primitives are matched with muon stubs, or tower primitives, to form muon, electron, or jet objects, on which simple acceptance cuts are applied.

### E.2 Level-2

At Level-2, an asynchronous system of custom-designed integrated circuits processes the time-ordered events accepted by the Level-1. Additional information from the shower-maximum strip chambers in the central calorimeter and the axial hits in the SVXII are combined with Level-1 primitives to produce Level-2 primitives. A crude energy-clustering is done in the calorimeters by merging the energies in adjacent towers to the energy of a seed tower above a preset threshold. Level-1 track primitives matching shower-maximum clusters provide refined electron candidates whose azimuthal position is known with  $2^\circ$  accuracy. Information from the  $(r, \varphi)$  sides

of the SVXII is combined with Level-1 tracks primitives to form two-dimensional tracks with resolution similar to the off-line one. Finally, an array of programmable processors makes the trigger decision, while Level-2 later accepted objects at Level-1 are being reconstructed.

### E.3 Level-3

The digitized output relative to the Level-2-accepted event arrives fragmented from all subdetectors via optical fibers. It is collected by a custom hardware switch that arranges it in the proper order and transfers it to 292 (as of this writing) commercial computers, running LINUX and organized in a modular and parallelized structure of 16 subsystems [55]. The ordered fragments are assembled in the *event record*, a block of data that univocally corresponds to a bunch crossing and is ready for the analysis of the Level-3 software. The event reconstruction makes use of the full detector information and has an improved resolution with respect to the preceding trigger levels, including three-dimensional track reconstruction, tight matching between tracks and calorimeter or muon information, and calibration information. If an event satisfies the Level-3 requirements, it is transferred to mass storage at a maximum rate of 20 Mbyte/s. The Level-3 decision is made after the full reconstruction of the event is completed and the integrity of its data is checked, a process that takes a few milliseconds. A fraction of the output events is monitored in real time to search for detector malfunctions, to derive calibrations constants and to graphically display events for inspection.

# Appendix F

## Track Parameters

The arc of the helix is parameterized using three transverse, and two longitudinal parameters:

$C$  – signed helix (half)-curvature, defined as  $C \equiv \frac{q}{2R}$ , where  $R$  is the radius of the helix and  $q$  is the charge of the particle. This is directly related to the transverse momentum:  $p_T = \frac{cB}{2|C|}$ ;

$\varphi_0$  –  $\varphi$  direction of the particle at the point of closest approach to the  $z$ -axis;

$d_0$  – signed impact parameter, i. e., the distance of closest approach to the  $z$ -axis, defined as  $d_0 \equiv q(\sqrt{x_c^2 + y_c^2} - R)$ , where  $(x_c, y_c)$  are the coordinates of the center-guide;

$\lambda$  – the helix pitch, i. e.,  $\cot(\vartheta)$ , where  $\vartheta$  is the polar direction of the particle at the point of its closest approach to the  $z$ -axis. This is directly related to the longitudinal component of the momentum:  $p_z = p_T \cot(\vartheta)$ ;

$z_0$  – the  $z$  coordinate of the point of closest approach to the  $z$ -axis.

Every point along the trajectory satisfies the following equations[62]:

$$x = r \sin \varphi - (r - d_0) \sin \varphi_0, \quad (\text{F.1})$$

$$y = -r \cos \varphi + (r - d_0) \cos \varphi_0, \quad (\text{F.2})$$

$$z = z_0 + s\lambda, \quad (\text{F.3})$$

where  $s$  is the length projected along the track, and  $\varphi = 2Cs + \varphi_0$ .



## Appendix G

# Signal and Background Cross Sections

The following is the list of signal and background cross sections of interest in this work.

- *Signal processes:*

$$p\bar{p} \rightarrow WW$$

$$p\bar{p} \rightarrow WZ$$

$$p\bar{p} \rightarrow ZZ$$

- *Signal cross section:*

$$\sigma(WW \rightarrow l\nu jj + WZ \rightarrow l\nu jj + ZZ \rightarrow ll jj) = 2.66 \text{ pb}$$

- *Background processes:*

$$p\bar{p} \rightarrow W(\rightarrow l\nu) + jets$$

$$p\bar{p} \rightarrow W(\rightarrow \tau\nu) + jets$$

$$p\bar{p} \rightarrow Z(\rightarrow ll) + jets$$

$$p\bar{p} \rightarrow t\bar{t} + \dots; t \rightarrow Wb$$

fake  $e/\mu$  from QCD processes

$$p\bar{p} \rightarrow W(\rightarrow l\nu) + c$$

$$p\bar{p} \rightarrow tb$$

- *Background cross sections:*

$$\sigma_{W(e\nu)+jets} = 2066 \text{ pb}$$

$$\sigma_{Z(e^+e^-)+jets} = 187 \text{ pb}$$

$$\sigma_{W\rightarrow l\nu+c} = 7.3 \text{ pb}$$

$$\sigma_{SingleTop} = 2.3 \text{ pb}$$

## Appendix H

# Nominal Interaction Vertex

All the significant variables of jets (particles) in an event are reconstructed starting from the event vertex (*evt*). This point can be displaced from the detector center. Because of the projective nature of calorimeter towers it is useful to have detector center as reference in such a way to better identify sensitive or not-sensitive calorimeter regions. A function is built to find the partons  $\eta$  in the detector frame.

The function starts with the  $\eta_{evt}$  and then considering the distances between the detector center and the first layer of the calorimeter (central and forward one) calculates the  $\eta_{det}$ . The used distance are  $R = 172.7$  cm, the radial distance of the first calorimeter layer from the center of the detector, and  $Z_{max} = 174.0$  cm, the z-distance between plags and detector center.

The function is tested using calorimeter-jets info; for caljet the bank provides  $\eta_{detector}$  info too. Results are in figure H.1.

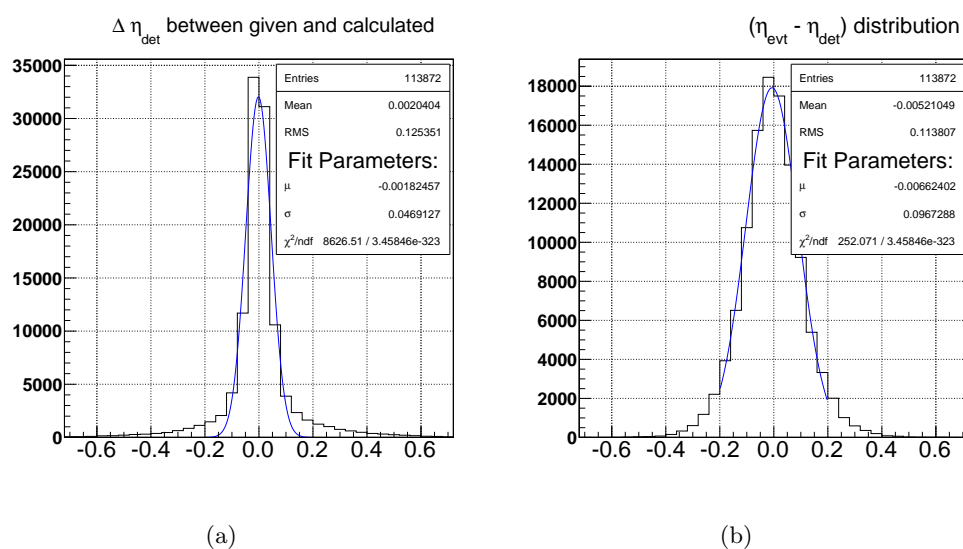


Figure H.1: Difference between  $\eta_{\text{detector}}$  as given by CaljetBlock in the StnNtuple and  $\eta_{\text{detector}}$  calculated by function (a) or difference between  $\eta_{\text{event}}$  and  $\eta_{\text{detector}}$  as given by caljets bank (b)

# Bibliography

## Chapter 1

- [1] M. Breidenbach *et al.*, “Observed Behavior Of Highly Inelastic Electron-Proton Scattering”, *Phys. Rev. Lett.* **23**, 935 (1969).
- [2] F. Halzen, A. Martin, *Quarks and Leptons: An Introductory Course in Modern Particle Physics*, John Wiley & Sons, 1984.
- [3] D.H. Perkins, *Introduction to High Energy Physics*, Cambridge University Press, 2000.
- [4] L.H. Ryder, *Quantum Field Theory*, Cambridge University Press, 1996.
- [5] C. Amsler *et al.*, *Particle data group*, *Phys. Lett.* **B 667**, 1 (2008)
- [6] A.I. Veinstein, *Sov. Phys. Usp.*, **23**, 429 (1980).
- [7] E. Fermi, *Nuovo Cim.*, **11**, 1 (1934).
- [8] R. P. Feynman and M. Gell-Mann, *Phys. Rev.* **109**, 193 (1958).
- [9] R. E. Marshak and E. C. G. Sudarshan, *Phys. Rev.* **109**, 1860 (1958).
- [10] S. A. Bludman, *Nuovo Cim.*, **9**, 433 (1958).
- [11] F. J. Hasert *et al.*, *Phys. Lett.* **B 46**, 121 (1973).
- [12] S. L. Glashow, *Nucl. Phys.*, **22**, 579, (1961).
- [13] P. W. Higgs, *Broken Symmetries, Massless Particles and Gauge Fields*, *Phys. Lett.* **12**, 132 (1964)
- [14] N. Cabibbo *et al.*, *Nucl. Phys.* **B 158**, 295 (1979); See, e.g., G. Altarelli and G. Isidori, *Phys. Lett.* **B 337**, 141 (1994); J.A. Casas, J.R. Espinosa, and M.

- Quiros, Phys. Lett. **B 342**, 171 (1995) idem., Phys. Lett. **B 382**, 374 (1996);  
T. Hambye and K. Riesselmann, Phys. Rev. **D 55**, 7255 (1997).
- [15] LEP Electroweak Working Group: <http://lepewwg.web.cern.ch/LEPEWWG/>.
- [16] S. Weinberg, Phys. Rev. Lett. **19**, 1264 (1967).
- [17] A. Salam, *Elementary particle theory*, In N. Svartholm, editor, Proc. 8th Nobel Symp. Almqvist and Forlag A. B., Stockholm, 1968.
- [18] UA1 Collaboration, G. Arnison *et al.*, Phys. Lett. **B126**, 398 (1983). UA2 Collaboration, P. Bagnaia *et al.*, Phys. Lett. **B129**, 130 (1983). UA1 Collaboration, G. Arnison *et al.*, Phys. Lett. **B122**, 103 (1983). UA2 Collaboration, P. Banner *et al.*, Phys. Lett. **B129**, 476 (1983).
- [19] Hideki Yukawa, *On the interaction of elementary particles*, Proc. Phys. Math. Soc. Jap. **17**, 48–57 (1935).
- [20] D. J. Gross and Frank Wilczek, *Ultraviolet behaviour of non-abelian gauge theories*, Phys. Rev. Lett. **30**, 1343–1346 (1973).
- [21] H. David Politzer, *Setting the scale for predictions of asymptotic freedom*, Phys. Rev. **D 9**, 2174–2175 (1974).
- [22] J. M. Campbell and R. K. Ellis, “*Update on vector boson pair production at hadron colliders*”, Phys. Rev. **D 60**, 113006 (1999).
- [23] F. Abe *et al.* (CDF Collaboration), “*Evidence for  $W^+W^-$  Production in  $p\bar{p}$  Collisions at  $\sqrt{s} = 1.8$  TeV*”, Phys. Rev. Lett. **78**, 4536 (1997).
- [24] B. Abbott *et al.* (D0 Collaboration), “*Studies of  $WW$  and  $WZ$  production and limits on anomalous  $WW\gamma$  and  $WWZ$  couplings*”, Phys. Rev. **D 60**, 072002 (1999).
- [25] M. Neubauer, for the CDF and DØ Collaborations, arXiv:hep-ex/0605066v2, 2006.
- [26] A. Annovi *et al.* (CDF Collaboration), “*Search for Diboson production in  $WW/WZ \rightarrow l\nu jj$  using  $3.9 fb^{-1}$* ”,  
<http://www-cdf.fnal.gov/physics/ewk/2009/jjlnu/index.html>. The results have been approved as of June 25th, 2009.

- [27] G. Flanagan *et al.* (CDF Collaboration), “*Observation of Diboson Production in  $E_T + jets$  channel*”, May 28th 2009, to be published on arXiv:0905.4714.
- [28] K. Hagiwara, J. Woodside, and D. Zeppenfeld, “*Measuring the WWZ coupling at the Fermilab Tevatron*”, Phys. Rev. **D 41**, 2113 (1990).
- [29] ALEPH and DELPHI and L3 and OPAL Collaboration and the LEP Working Group for Higgs Boson Searches, Phys. Rev. Lett. **565**, 61 (2003);  
ALEPH Collaboration, J. Alcaraz *et al.*, *A combination of preliminary electroweak measurements and constraints on the Standard Model*, arXiv:hep-ex/0612034, December (2006).
- [30] CDF II Collaboration, Top Quark Group Physics Results: <http://www-cdf.fnal.gov/physics/new/top/top.html>.

## Chapter 2

- [31] D. P. McGinnis, *Fermilab Tevatron operational status*, in C. Horak (ed.), proceedings of the Particle Accelerator Conference (PAC 05), (2005).
- [32] Fermilab Beam Division, *Run II Handbook*, and *Operations Rookie Books*.
- [33] R. Blair *et al.* [CDF Collaboration], *The CDFII Detector: Technical Design Report*, FERMILAB-Pub-96/390-E (1996).
- [34] D. Mohl *et al.*, *Physics and Technique of Stochastic Cooling*, Phys. Rept. **58**, **73**, 1980,
- [35] S. Nagaitsev *et al.*, *Experimental Demonstration of Relativistic Electron Cooling*, Phys. Rev. Lett. **96**, **044801**, 2006,
- [36] C. Avila *et al.* [E811 Collaboration], *A Measurement Of The  $p\bar{p}$  Total Cross-Section at  $\sqrt{s} = 1.8$  TeV*, Phys. Lett. B **445** (1999) 419 [doi:10.1016/S0370-2693(98)01421-X]; F. Abe *et al.* [CDF Collaboration], *Measurement Of The  $p\bar{p}$  Total Cross-Section at  $\sqrt{s} = 546$  GeV and 1800 GeV*, Phys. Rev. D **50** (1994) 5550-5561 [doi:10.1103/PhysRevD.50.5550].
- [37] Fermilab Accelerator Division web-page: <http://www-bd.fnal.gov/pplot/index.html>
- [38] The CDF Collaboration: *The CDF II Detector Technical Design Report* FERMILAB-PUB-96/390-E, October, 1996 The CDF Collaboration: *Summary of the CDF RunII Detector Parameters*

- [39] The CDF Collaboration: *Proposal for Enhancement of the CDF II Detector: an Inner Silicon Layer and a Time of Flight Detector* FERMILAB-PROPOSAL-909 (and updates), October 23, 1998
- [40] A. Sill: *CDF Run II silicon tracking projects* Nucl. Instrum. Methods **A447, 1, 2000**, . C. Kruse: *Silicon Detector Upgrades for the Tevatron Run 2* FERMILAB-CONF-02/253-E. Published Proceedings 31st International Conference on High Energy Physics (ICHEP 2002), Amsterdam, The Netherlands, July 24-31, 2002
- [41] A. Affolder *et al.*, *Status report of the intermediate silicon layers detector at CDF II*, Nucl. Instrum. Methods **A485,6,2002**,
- [42] C. S. Hill, *Initial experience with the CDF layer  $\emptyset\emptyset$  silicon detector* , Nucl. Instrum. Methods **A511,118,2003**,
- [43] A. Affolder *et al.*, *CDF Central Outer Tracker*, Nucl. Instrum. Methods **A526, 249, 2004**,
- [44] Ch. Paus *et al.*, *Design and performance tests of the CDF time-of-flight system*, Nucl. Instrum. Methods **A461,579,2001**, . Acosta *et al.*, *A Time-of-Flight detector in CDF-II*, Nucl. Instrum. Methods **A518,605,2004**,
- [45] R. D. Erbacher, *Calorimetry in CDF Run 2*, FERMILAB-CONF-02/251-E. Published Proceedings 31st International Conference on High Energy Physics (ICHEP 2002), Amsterdam, The Netherlands, July 24-31, 2002; S. Kuhlmann *et al.*, *The CDF calorimeter upgrade for Run Iib*, Nucl. Instrum. Methods **A518,39,2004**, L. Breccia *et al.*, *Test of 2000 phototubes for the CDF endplug calorimeter upgrade*, Nucl. Instrum. Methods **A532,575,2004**,
- [46] L. Balka *et al.*, *The CDF central electromagnetic calorimeter*, Nucl. Instrum. Methods **A267,272,1988**,  
S. R. Hahn *et al.*, *Calibration systems for the CDF central electromagnetic calorimeter*, Nucl. Instrum. Methods **A267, 351,1988**,
- [47] M. Gallinaro, *A New Scintillator Tile/Fiber Preshower Detector for the CDF Central Calorimeter*, IEEE Trans. Nucl. Sci. **52,879,2005**, , ([()physics/0411056]).
- [48] S. Bertolucci *et al.*, *The CDF central and endwall hadron calorimeter*, Nucl. Instrum. Methods **A267, 301, 1988**,

- [49] M. Albrow *et al.*, *The CDF plug upgrade electromagnetic calorimeter: test beam results*, Nucl. Instrum. Methods **A480**, 524, 2002, M. Albrow *et al.*, *A preshower detector for the CDF Plug Upgrade: test beam results*, Nucl. Instrum. Methods **A431**, 104, 1999, G. Apollinari *et al.*, *Shower maximum detector for the CDF plug upgrade calorimeter*, Nucl. Instrum. Methods **A412**, 515, 1998, M. Albrow *et al.*, *Intercalibration of the longitudinal segments of a calorimeter system*, Nucl. Instrum. Methods **A487**, 381, 2002,
- [50] G. Ascoli *et al.*, *CDF central muon detector*, Nucl. Instrum. Methods **A268**, 33, 1988, C. M. Ginsburg, *CDF Run 2 Muon System*, Eur. Phys. J. **33**, S1002, 2004,
- [51] C. Avila *et al.* (E811 Collaboration), *A measurement of the proton-antiproton total cross-section at  $\sqrt{s} = 1.8$  TeV*, Phys. Lett. **B445**, 419, 1999, F. Abe *et al.* (CDF Collaboration), *Measurement of the anti-proton proton total cross-section at  $\sqrt{s} = 546$  GeV and 1800 GeV*, Phys. Rev. D **50**, 5550, 1994,
- [52] D. Acosta *et al.*, *The performance of the CDF luminosity monitor*, Nucl. Instrum. Methods **A494**, 57, 2002,
- [53] K. Goulios *et al.*, *The CDF miniplug calorimeters at the Tevatron*, Nucl. Instrum. Methods **A518**, 42, 2004, [physics/0310156].
- [54] M. Karagoz Unel and R. J. Tesarek, *Beam Halo monitoring at CDF*, Nucl. Instrum. Methods **A506**, 7, 2003, [hep-ex/0211055].
- [55] G. Gomez-Ceballos *et al.*, *Event Builder and Level 3 at the CDF experiment*, Nucl. Instrum. Methods **A518**, 522, 2004,
- [56] E. Gerchtein and M. Paulini, *CDF detector simulation framework and performance*, eConf. **C0303241**, TUMT005, 2003 physics/0306031] (2003).
- [57] ROOT: *An Object Oriented Analysis Framework* : <http://root.cern.ch>
- [58] M.L. Mangano *et al.*, *ALPGEN, a generator for hard multiparton processes in hadronic collisions* JHEP 0307:001, (2003).
- [59] T. Sjostrand *et al.*, *High-Energy-Physics Event Generation with PYTHIA 6.1*, Comp. Phys. Commun. 135, 238 (2001); Pythia home page: <http://www.thep.lu.se/~torbjorn/Pythia.html>.

- [60] G. Corcella *et al.*, *HERWIG 6.5 release note*, arXiv:hep-ph/0210213, Oct 15, 2002.
- [61] R. Brun *et al.*, *GEANT: Simulation Program For Particle Physics Experiments. User Guide And Reference Manual*, CERN-DD-78-2-REV (1978).

### Chapter 3

- [62] J. Marriner, *Secondary vertex fit with mass and pointing constrains (CTVMFT)*, CDF Internal Note 1996 (1993), unpublished.
- [63] F. D. Snider *et al.*, *Tracking at CDF: Algorithms and Experience from Run I and Run II*, Nucl. Instrum. Methods **566**, 133 (2006).
- [64] P. Azzi *et al.*, *Histogram tracking in the COT*, CDF note 5562, February 21, 2001.
- [65] K. Bloom, W. M. Yao, “*Outside-In*” *Silicon Tracking at CDF*, CDF note 5991, June 5, 2002.
- [66] Byeong Rok Ko *et al.*, *SVXII Stand-alone Tracking*, CDF note 6440, May 15 (2003).
- [67] C. Hays *et al.*, *Inside-out tracking at CDF*, Nucl. Instrum. Methods **538**,249 (2005)
- [68] J. Goldstein *et al.*, *Silicon Tracking for Plug Electrons*, CDF note 5970, May 16, 2002.
- [69] S. Harper *et al.*, *Reconstructing the Plug Electron Energy in 5.3.3*, CDF note 7687, July 17, 2005.
- [70] CDF Collaboration, *Measurement of the inclusive W and Z cross sections in p $\bar{p}$  collisions at  $\sqrt{s} = 1.96$  TeV*, Jour. of Phys. G 34, 2457 (2007)
- [71] U. Grunder *et al.*, *High-PT muons recommended cuts and efficiency for Summer 2006*, May 31, 2006.
- [72] The CDF Collaboration, *Topology of three-jet events in p $\bar{p}$  collisions at  $\sqrt{s} = 1.8$  TeV*, Phys. Rev. D **45**, 1448,1992,  
(G). C. Blazey *et al.*, *Run II Jet Physics*, CDF note 5293, April 18, 2000

- [73] G. Latino, *Calorimetric Measurements in CDF: a New Algorithm to Improve the Energy Resolution of Hadronic Jets*, Ph. D. Thesis, Università di Cassino, 2001
- [74] A. Bhatti *et al.*, *Determination of the jet energy scale at the Collider Detector at Fermilab*, Nucl. Instrum. Methods **A566**, 375,2006,
- [75] J. Adelman *et al.*, *Generic Jet Scale Correction for Run II*, CDF note 7358, December 12, 2005.

#### Chapter 4

- [76] U.-K. Yang and B. Knuteson, “*Muons from  $\pi/K$  Decay in Flight and their impact on Top/ElectroWeak/Exotic Physics*”, <http://hep.uchicago.edu/ukyang/talk/cdf/kaonmuon.pdf>

#### Chapter 5

- [77] Anna Sfyrla, “*Search for WW and WZ production in electron-neutrino plus dijet final state using 1.29 fb<sup>-1</sup> of data*”, CDF note 8740.
- [78] N. Pozzobon, *Pisa graduation thesis “Experimental study of the WZ intermediate bosons associated production with the CDF experiment”*, CDF note 9005.
- [79] G. Bellettini, G. Latino, N. Pozzobon, G. Velez, “*Specific jet energy corrections in the search for WZ to lvbb*”, CDF note 9005.
- [80] Rick Field, “*The Underlying Event in Run 2*”, CDF note 6403.



# Acknowledgements

During the time I spent to make this work many people supported me both in professional and personal life, so I would like to thank anyone of them for their generosity and for their real friendship.

I start to thank Dr Vadim Rusu who gave me help in understanding and using the codes useful in this analyses, for his patience and his generous behaviour when asked for fast producing some MC samples. I am grateful to Marco Trovato who suggested me right things and helped me in resolving codes and conceptual troubles pushing me ahead when everything seemed stopped, who always had time to listen my innocent questions and whose friendship was something over just working matter. I need to say thanks to Giuseppe Latino whose ideas and suggestions was everytime illuminating: without his support and experience I could never finish my work. Thanks to Gueorgui Velez who spent time in discussing the correctness of my ideas. I feel very grateful to my main advisor Giorgio Bellettini who put me in the condition of doing unusual experiences, followed my steps, carefully revised this thesis and listened to me showing deep interest even when he was not supposed to. Also thanks to Caterina Vernieri whose summer student work was useful to me for finding and fixing bugs in the codes.

I want to thank Fermilab friends Paolo, Michael, Diego, Michele, Pierluigi, Guido, Benedetto, Matteo, Lorenzo, Roger, Federico, the mexican and brasilian friends and anyone who helped me in understanding stuff and improving my knowledge.

Special thanks to Patrizia, Januscia, Viviana and Angelo who took care of me in the hardest Fermilab days when no time to sleep was available.

Last but not least among Fermilab friends Mirco Dorigo (“the terrorist”) with whom I shared the sad and long nights in front of a monitor in the trailers office trying to understand and fix the bugs!

I cannot forget Pisa friends, the “Fascetti” ones, the “Zia Veronica Caprino fun

Club”, the “Brigate CMT” (c muvimm CON MOLTA TRANQUILLITA) group and all the other guys I met in these years.

Finally, and this means the most important, I need to thank my family and my girlfriend Giuseppina, the former since supported me all the times and because their pride in me (also if I think they are prouder than needed) make me sure to be able in doing everything, the latter since accepted the challenge to stay with me!